# VYSOKÉ UČENÍ TECHNICKÉ V BRNĚ

BRNO UNIVERSITY OF TECHNOLOGY

FAKULTA ELEKTROTECHNIKY A KOMUNIKAČNÍCH TECHNOLOGIÍ
ÚSTAV TEORETICKÉ A EXPERIMENTÁLNÍ ELEKTROTECHNIKY

FACULTY OF ELECTRICAL ENGINEERING AND COMMUNICATION
DEPARTMENT OF THEORETICAL AND EXPERIMENTAL ELECTRICAL ENGINEERING


# IMPLEMENTATION OF DIXON METHODS FOR PRECLINICAL MR IMAGING AT HIGH FIELDS

DIZERTAČNÍ PRÁCE
DOCTORAL THESIS


AUTOR PRÁCE — Ing. RADIM KOŘÍNEK
AUTHOR



BRNO 2015


VYSOKÉ UČENÍ TECHNICKÉ V BRNĚ

BRNO UNIVERSITY OF TECHNOLOGY


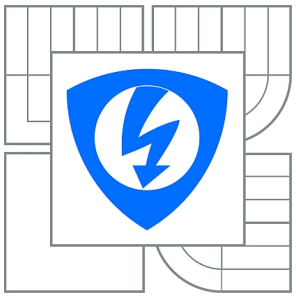


FAKULTA ELEKTROTECHNIKY A KOMUNIKAČNÍCH TECHNOLOGIÍ

ÚSTAV TEORETICKÉ A EXPERIMENTÁLNÍ ELEKTROTECHNIKY

FACULTY OF ELECTRICAL ENGINEERING AND COMMUNICATION

DEPARTMENT OF THEORETICAL AND EXPERIMENTAL ELECTRICAL ENGINEERING


# IMPLEMENTATION OF DIXON METHODS FOR PRECLINICAL MR IMAGING AT HIGH FIELDS

IMPLEMENTACE DIXONOVÝCH TECHNIK PRO PREKLINICKÉ MR ZOBRAZOVÁNÍ NA VYSOKÝCH POLÍCH

DIZERTAČNÍ PRÁCE

DOCTORAL THESIS


AUTOR PRÁCE — Ing. RADIM KOŘÍNEK

AUTHOR

VEDOUCÍ PRÁCE — prof. Ing. KAREL BARTUŠEK, DrSc.

SUPERVISOR



BRNO 2015

# ABSTRACT

Preclinical magnetic resonance (MR) imaging in small animals is a very popular procedure that requires a higher sensitivity, given the small size of the subjects. A higher sensitivity can be reached when an MR imaging system with a high magnetic field is used (e.g., 4.7 T or higher). The benefits of such sensitivity include, for example, a higher resolution, an improved signal-to-noise ratio (SNR), an increased chemical shift, and a longer $T_1$ longitudinal relaxation time. On the other hand, a high field causes stronger static magnetic field deformation along the borders between tissues with different susceptibilities, and it also results in the shortening of the $T_2$ transversal relaxation.

Adipose tissue is significantly contained in the human (or mammal) body and is primarily used to store energy in the form of fat. This tissue can be classified into white and brown subsets. Brown adipose tissue is found mainly in new-born children, and a certain (yet very small) amount of such tissue can be traced also in adults. White adipose tissue then ensures the storage of fat as a source of energy. Furthermore, white adipose tissue produces adipokines, hormones, and many other substances important for metabolism. Generally, fat can be regarded as a biomarker in the case of specific diseases (obesity, steatosis – fatty liver disease, and others). Thus, the quantification of fat is a precondition for correct diagnosis. MR imaging comprises a special group of methods for water-fat separation; these methods are referred to as Dixon methods and utilize the principle of chemical shift.

In this thesis, a new $T_2$ – weighted sequence for Dixon acquisition is introduced (Chapter 5.3). The proposed sequence is a very time-effective three-point (3PD) method. The newly proposed sequence of fast triple spin echo Dixon (FTSED) is derived from the original fast spin echo sequence (FSE). Such modification of the original FSE sequence leads to a novel FTSED sequence, where three images are acquired simultaneously without any increase of the total acquisition time. The discussed sequence was successfully implemented on a 9.4 T MR imaging system at the Institute of Scientific Instruments, ASCR Brno. The acquired data were calculated through the use of the IDEAL (iterative decomposition of water and fat with echo asymmetry and least-squares estimation) algorithm. The results of the computation are water and fat images, and the fat fraction (FF) can be calculated from these. The sequence was successfully tested in a rat. The successful FTSED implementation on a 9.4 T MR imaging system enables this method to be used in low-field MR imaging systems.

# KEYWORDS

Magnetic resonance imaging; the Dixon method; fast triple spin echo Dixon; FTSED; high field; preclinical research; iterative decomposition.

# ABSTRAKT

Preklinické magneticko-rezonanční (MR) zobrazování na malých zvířatech je velmi aktuální a vyžaduje, vzhledem k rozměrům těchto zvířat, vyšší citlivost. Vyšší citlivosti lze dosáhnout použitím MR systému s vysokým základním magnetickým polem (např. 4,7 T a výše). Vyšší citlivost přináší výhody v podobě možnosti vyššího rozlišení, lepší poměr signál-šum, větší chemický posuv, prodloužení longitudinální relaxace ($T_1$), atd. Na druhou stranu vyšší magnetické pole znamená větší deformace základního magnetického pole na rozhraních tkání s rozdílnou susceptibilitou a zkrácení transverzální relaxace ($T_2$).

Tuková tkáň je významně zastoupena v lidském těle a primárně sloužící pro uchovávání energie ve formě tuků. Tukovou tkáň lze rozdělit na hnědou a bílou tukovou tkáň. Hnědá tuková tkáň se vyskytuje hlavně u novorozenců, ale může být ve velmi malém množství také u dospělých jedinců. Bílá tuková tkáň je určena pro ukládání tuků, které slouží jako zdroj energie. Kromě toho bílá tuková tkáň produkuje adipokiny, hormony a mnoho dalších látek důležitých pro náš metabolizmus. Tuk lze obecně považovat jako biomarker při určitých nemocech (obezita, steatóza jater, a další). Z tohoto důvodu je kvantifikace tuku velmi důležitá pro správnou diagnózu. V MR zobrazování je speciální skupina metod pro separaci vody a tuku. Tyto metody se nazývají Dixonovy metody a jejich princip je založen na chemickém posuvu.

V této práci je popsána nová $T_2$-váhovaná sekvence pro Dixonovu akvizici (Kapitola 5.3). Navržená sekvence je z hlediska akviziční doby velmi efektivní a řadí se mezi tříbodové Dixonovy (3PD) techniky. Nově navržená sekvence fast triple spin echo Dixon (FTSED) vychází z původní sekvence rychlého spinového echa (FSE). Modifikací původní sekvence FSE vedla ke vzniku nové sekvence FTSED, která umožňuje získat tři obrazy během jediné akvizice, bez toho aniž bychom prodloužili celkovou dobu měření. Sekvence byla úspěšně implementována na 9,4 T MRI systém na Ústavu přístrojové techniky v Brně. Získaná data byla pak zpracována iterativně pomocí algoritmu IDEAL (iterative decomposition of water and fat with echo asymmetry and least-squares estimation). Výsledkem jsou separátní obrazy vody a tuků, z kterých lze vypočítat mapy frakce tuku (FF-mapy). Sekvence byla ověřena na fantomech a poté byla odzkoušena potkanovi. Úspěšná implementace této metody na 9,4 T MRI systému znamená, že může být použita také na MR zobrazovacích systémech s nižšími magnetickými poli.

# KLÍČOVÁ SLOVA

Zobrazování magnetickou rezonancí; Dixonova metoda; fast triple spin echo Dixon; FTSED; vysoké pole; preklinický výzkum; iterativní dekompozice.

KOŘÍNEK, R. Implementace Dixonových technik pro preklinické MR zobrazování na vysokých polích. Brno: Vysoké učení technické v Brně, Fakulta elektrotechniky a komunikačních technologií, 2015. 87 s. Vedoucí dizertační práce prof. Ing. Karel Bartušek, DrSc..

# PROHLÁŠENÍ

Prohlašuji, že svou dizertační práci na téma implementace Dixonových metod pro preklinické MR zobrazování na vysokých polích jsem vypracoval samostatně pod vedením vedoucího dizertační práce a s použitím odborné literatury a dalších informačních zdrojů, které jsou všechny citovány v práci a uvedeny v seznamu literatury na konci práce.

Jako autor uvedené dizertační práce dále prohlašuji, že v souvislosti s vytvořením této dizertační práce jsem neporušil autorská práva třetích osob, zejména jsem nezasáhl nedovoleným způsobem do cizích autorských práv osobnostních a/nebo majetkových a jsem si plně vědom následků porušení ustanovení § 11 a následujících zákona č. 121/2000 Sb., o právu autorském, o právech souvisejících s právem autorským a o změně některých zákonů (autorský zákon), ve znění pozdějších předpisů, včetně možných trestněprávních důsledků vyplývajících z ustanovení části druhé, hlavy VI. díl 4 Trestního zákoníku č. 40/2009 Sb.

V Brně dne ..... .....

(podpis autora)

# PODĚKOVÁNÍ

Tato práce vznikla za finanční podpory Národního programu udržitelnosti I (NPU-I), projekt LOL1212.

Děkuji vedoucímu diplomové práce prof. ing. Karlu Bartuškovi, DrSc. za účinnou metodickou, pedagogickou a odbornou pomoc a další cenné rady při zpracování mé dizertační práce. Dále bych chtěl poděkovat Ústavu přístrojové techniky AV ČR, v. v. i. v Brně a vedoucímu NMR oddělení Ing. Zenonovi Starčukovi (jr), CSc. za možnost přístupu na 9,4 T MRI systém, na který byla implementována a odzkoušena navržená metoda.

V Brně dne ..... .....

(podpis autora)

# Table of content

# Introduction

Magnetic resonance imaging (MRI) or nuclear magnetic resonance (NMR) constitutes one of the most significant tomographic technologies applicable in medicine and biology. By extension, nuclear magnetic resonance spectroscopy (MRS) is a very important instrument for chemistry and research of materials. In 1946, Felix Bloch defined Bloch equations, which describe the time evolution of the magnetization vectors of spins. The first one-dimensional (1D) MRI image was presented by Herman Yaggi Carr in his Ph.D thesis in 1953 [1]. Seven years later, in the USSR, Vladislav Ivanov introduced a document (about an MR imaging device) which was forwarded for review to scientific institutes in St. Petersburg (Leningrad), [2]. In 1971, Raymond Damadian presented his findings related to in vivo detection of a tumour via NMR [3], and in 1972 he created and patented the first MRI scanner in the world (U.S. patent #3,789,832). Paul Lauterbur later showed how gradients can be applied to generate MRI images in 2D and 3D. The first 1.5 T MRI scanner was released in 1980. At present, the standard magnetic field in human body imaging is 1.5 T, 3 T and 7 T; the last of these variants is becoming increasingly popular thanks to the higher sensitivity. Moreover, advanced 9.4 T MR imaging systems are currently used for human imaging. In the case of studies centered on animals, measurements of up to 21.1 T [4], [5] have been performed. Otherwise, a high field comprises certain advantages/disadvantages [6], including higher sensitivity to susceptibility artefacts (disadvantage), extension of the relaxation times $T_1$ and $T_2$ (advantage – narrower spectral lines; disadvantage – longer measurement time [7]), and higher chemical shift (advantage – the spectral lines are far from each other).

All isotopes which contain an odd number of protons exhibit an intrinsic magnetic moment and an angular moment, which means that these isotopes have a nonzero spin (e. g., $^{1}$H, $^{13}$C, $^{15}$N, $^{17}$O, $^{19}$F $^{29}$Si, $^{31}$P, $^{43}$Ca, $^{57}$Fe, $^{129}$Xe). Importantly, one of these is $^{1}$H. The human body contains mainly $^{1}$H protons (90 % of nuclei in the body); hence, the protons are measured using MRI. Another frequently measured nucleus is sodium $^{23}$Na (lower sensitivity than $^{1}$H). A major procedure for increasing MRI sensitivity is hyperpolarization (e. g., hyperpolarized $^{13}$C, $^{129}$Xe). A significant feature of NMR lies in the resonance frequency (Larmor frequency) $\omega$; this feature depends on the strength of the applied magnetic field, on the gyromagnetic ratio $\gamma$ (e. g. $\gamma/2\pi(^{1}\text{H}) \sim 42.576$ MHz/T, $\gamma/2\pi(^{23}\text{Na}) \sim 11.262$ MHz/T), and it is sensitive to the chemical environment of the nucleus [8], [9].

During the $^{1}$H measurement of human tissues, the measured signal comprises the signal of fat and other substances (e.g., metabolites); metabolites can be measured with MRS (magnetic resonance spectroscopy). In many cases, fat plays an important role as a significant biomarker of the patient's health. The quantification of water and fat is possible because the chemical shift effect [10], [11] causes differences in Larmor frequencies between fat and water. "*Although the chemical shift information can be either frequency encoded* [12], [13], [14] *or phase encoded* [15] *to obtain chemical shift images using Fourier transform, this approach is limited by the very long data acquisition time, due to the additional chemical shift dimension. To achieve water-fat imaging with resolution, signal-to-noise ratio (SNR), and data acquisition time that are comparable to conventional MRI, more efficient methods must*

*be found*" [16]. The chemical shift in a two-peak water-fat model is ≈ 3.5 ppm between fat and water; in fact, however, the spectrum of fat is more complex (Fig. 2), and it is also important to consider the fact that the body of a human being or an animal accommodates many types of fat. Yet another factor for water-fat differentiation is longitudinal relaxation $T_1$ [17].

## 1.1. Adipose Tissue

Adipose tissue is a specialized connective tissue consisting mostly of fat cells (adipocytes) and found in mammals. "*In adults, the major bulk of adipose tissue is a loose association of lipid-filled cells called adipocytes, which are held in a framework of collagen fibers. In addition to adipocytes, adipose tissue contains stromal-vascular cells including fibroblastic connective tissue cells, leukocytes, macrophages, and pre-adipocytes (not yet filled with lipid), which contribute to structural integrity*" [18].

Adipose tissue in mammals can be classified into two main forms: white adipose tissue (WAT) and brown adipose tissue (BAT), Fig. 1. In the case of animals, the presence, amount, and distribution of each of these classes varies between the species [18]. The main purposes of WAT are heat insulation, mechanical cushioning, and provision of energy. Adipose tissue produces a number of biologically active substances, such as prostaglandins, insulin-like growth factor 1, binding proteins, adipsin, cytokines (e.g., the tumor necrosis factor α), estrogens (primarily estrone), and leptin [19]. The colour of the BAT is derived from the colour of vascularization and the densely packed mitochondria, and it can be found at various locations within the body. The primary function of BAT consists in thermogenesis (heat production). Adipose tissue is further divided according to its location in the body: subcutaneous fat can be found directly below the skin; epicardial fat is stored around the heart and supports cardiac functions [20], [21]; and abdominal fat is located in the abdominal cavity.

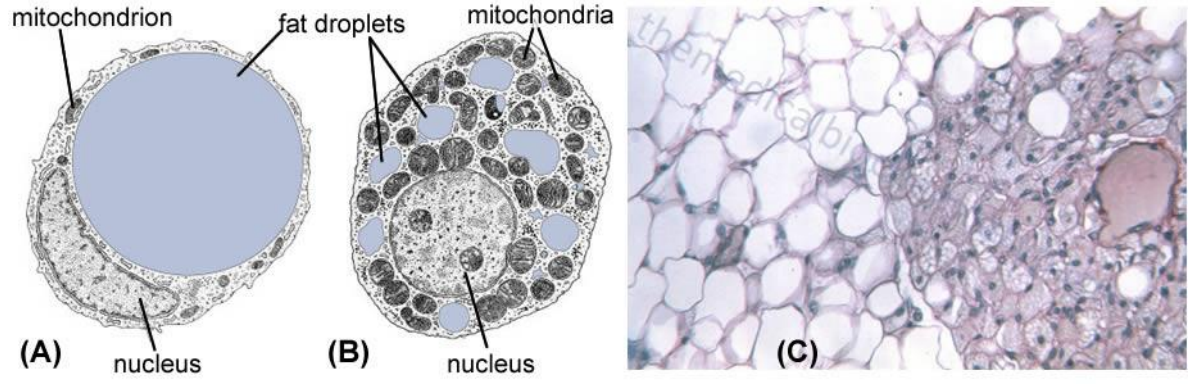


**Fig. 1** (A), (B) Schematic images of WAT and BAT cells [22]; (C) Morphology of the WAT and the BAT [23].

The WAT is a very variable component of the body, and its content indicator ranges between only a few percent of bodily weight to 50 % or more in the case of obese mammals. In mammals, this adipose tissue can be found under the skin, in the abdominal cavity, in musculature (between the muscles: intermuscular occurrence), and in muscles (intramuscular

occurrence, such as in the marbling of meat); furthermore, the tissue is located at several highly specialized points, including the eye socket [19]. As already mentioned above, the WAT secures the storage of energy in the form of triacylglycerol (fat, lipids). The size of a WAT cell oscillates from 25 to 200 μm. A WAT cell contains between 60 to 85 % (with 90 - 99 % triacylglycerol) of lipids, with the remaining portion occupied by free fatty acids, diglyceride, cholesterol, phospholipid, minute quantities of cholesterol ester, and monoglyceride. "*In this lipid mixture, six fatty acids make up approximately 90 % of the total, and these are myristic, palmitic, palmitoleic, stearic, oleic, and linoleic. Varying the composition of your diet can vary the fatty acid profile in adipose tissue. The remaining weight of white adipose tissue is composed of water (5 to 30 %) and protein (2 to 3 %)* [18]. One gram of adipose tissue contains 800 mg of triacylglycerol and approximately 100 mg of water [19].

The amount of brown fat in an organism (primarily in children) is small; although the main function of brown fat consists in thermogenesis, it also exerts influence on metabolism [24]. The size of adipocytes in the BAT is about 60 μm, and the lipids inside the cell exhibit about 25 μm in diameter [18]. This fat plays a significant role in the thermoregulation of new-born children [25]. Brown fat is frequently discussed in specialized articles from a variety of perspectives. For example, it was claimed in the past that the BAT is present only in infants, not in adult humans. Many studies centered on animals [26], [27], [28] indicated that brown fat in rodents has a profound effect on the body weight, energy balance, and glucose metabolism. The presence of brown fat was also observed in articles [29], [30] analysing processes in a human organism exposed to cold. In humans, Cypess et al. [31] showed that a relationship exists between the BAT and outdoor temperature and that the prevalence of BAT differs between men and women. Lee at al., however, contended in their review that the BAT is present in most adult humans and is likely to play a regulatory role in energy metabolism [24]. The presence of BAT can be successfully observed using positron emission tomography (PET) [30], [31] and MRI [32], [33].

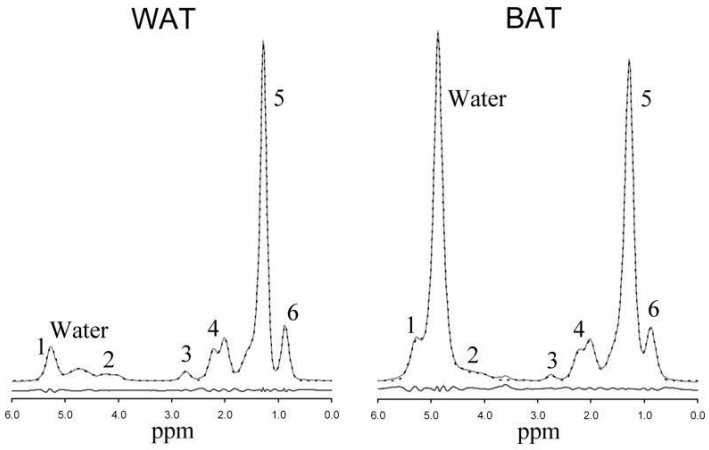


**Fig. 2** The MR spectra (mice) of white adipose tissue and brown adipose tissue measured with a 3T scanner ($T_R$ = 5000 ms, $T_E$ = 13 ms) [17].

In NMR, Hamilton et al. [17] demonstrated several key physical properties that are different for the BAT and the WAT, namely fat fraction, $T_1$ relaxation rate of the water

component, and the degree of lipid saturation. Thus, the BAT and the WAT can be differentiated in magnetic resonance; the spectra (Fig. 2) of both indicate that the water component of the WAT is much smaller than the main component of fat and comparable with the remaining fat components. In the case of the BAT, the water component is comparable with the main fat component. The adipose tissue structure (Fig. 1(C)) significantly influences the $T_1$ relaxation of bounded water (Tab. 1). The water bounded in the WAT exhibits a much longer $T_1$ compared to the water bounded in the BAT.

| Peak | In vivo ppm | Assignment | T1 (ms) | T2 (ms) | Measured signal | Calculated signal |
|---|---|---|---|---|---|---|
| 1 | 5.3 ppm | -**CH**=**CH**-<br>-**CH**-O-CO- | 421 (406–436) | 44.1 (42.6–45.6) | 0.127 (0.109–0.145) | 0.122 [7.6 %] |
| Water | 4.7 ppm | $\mathbf{H_2O}$ | 1053 (1005–1101) | 21.7 (17.3–26) | 0.124 (0.119–0.148) | – |
| 2 | 4.2 ppm | -$\mathbf{CH_2}$-O-CO- | 154 (145–163) | – | – | 0.064 [4.0 %] |
| 3 | 2.75 ppm | -CH=CH-$\mathbf{CH_2}$-CH=CH- | 284 (274–294) | 46.2 (44.5–47.9) | 0.027 (0.023–0.033) | 0.033 [2.0 %] |
| 4 | 2.1 ppm | -CO-$\mathbf{CH_2}$-$CH_2$-<br>-$\mathbf{CH_2}$-CH=CH-$\mathbf{CH_2}$- | 202 (194–210)<br>249 (238–259) | 51.9 (51.8–52.1) | 0.238 (0.237–0.238) | 0.241 [15.0 %] |
| 5 | 1.3 ppm | -CO-$CH_2$-$\mathbf{CH_2}$-<br>-$(\mathbf{CH_2})_n$- | 240 (214–264)<br>280 (268–292) | 54.7 (42.8–61.4) | 1.000 | 1.000 [62.4 %] |
| **6** | 0.9 ppm | -$(CH_2)_n$-$\mathbf{CH_3}$ | 543 (434–616) | 80.1 (50.7–110.2) | 0.147 (0.140–0.158) | 0.144 [9.0 %] |

| Peak | In vivo ppm | Assignment | T1 (ms) | T2 (ms) | Measured signal | Calculated signal |
|---|---|---|---|---|---|---|
| 1 | 5.3 ppm | -**CH**=**CH**-<br>-**CH**-O-CO- | – | – | – | 0.098 [6.4 %] |
| Water | 4.7 ppm | $\mathbf{H_2O}$ | 618 (588–669) | 21.1 (18.1–22.9) | 1.605 (0.901–1.865) | – |
| 2 | 4.2 ppm | -$\mathbf{CH_2}$-O-CO- | – | – | – | 0.060 [3.9 %] |
| 3 | 2.75 ppm | -CH=CH-$\mathbf{CH_2}$-CH=CH- | 219 (154–294) | 41.4 (32.3–48.7) | 0.016 (0.012–0.020) | 0.019 [1.2 %] |
| 4 | 2.1 ppm | -CO-$\mathbf{CH_2}$-$CH_2$-<br>-$\mathbf{CH_2}$-CH=CH-$\mathbf{CH_2}$- | 189 (156–216)<br>247 (235–265) | 55.3 (47.8–59.6) | 0.216 (0.213–0.219) | 0.218 [14.2 %] |
| 5 | 1.3 ppm | -CO-$CH_2$-$\mathbf{CH_2}$-<br>-$(\mathbf{CH_2})_n$- | 239 (227–265)<br>278 (271–292) | 51.8 (46.7–55.1) | 1.000 | 1.000 [65.3 %] |
| 6 | 0.9 ppm | -$(CH_2)_n$-$\mathbf{CH_3}$ | 567 (544–591) | 61.5 (50.9–71.3) | 0.149 (0.138–0.164) | 0.136 [8.9 %] |

**Tab. 1** The first table shows the mean (and range) of $T_1$, $T_2$ and $T_2$-corrected peak areas for white adipose tissue. The final column gives the predicted areas for ndb = 3.3 and nmidb = 1.0 [% total fat]. The second table summarizes the mean (and range) of $T_1$, $T_2$ and $T_2$-corrected peak areas for brown adipose tissue. The final column presents the predicted areas for ndb = 2.7 and nmidb = 0.6 [% total fat]. [17]

Fat is a significant element in magnetic resonance, and in many clinical studies it is necessary to differentiate between water and fat signals. For this purpose, methods facilitating fat/water suppression are being developed within MR.

# 2. State of the Art in Water-Fat MR Imaging

One of the most interesting domains in MRI consists in water and fat separation/suppression. The first articles describing various approaches for the separation/suppression of water and fat appeared almost 30 years ago. Methods for water and fat separation are based on two physical principles: longitudinal relaxation $T_1$ and chemical shift (CS). Each of the techniques exploits one of the above-mentioned principles, and all procedures developed for water and fat separation/suppression are utilized in clinical MR imaging (depending on the application and capabilities of the MRI system). The suppression/separation of water and fat is very useful in the treatment of fatty liver disease, and it also finds application in cardiology, magnetic resonance angiography (MRA), contrast-enhanced imaging, and other clinical processes or branches of medicine.

The discussed methods can be classified into four main categories: (1) Inversion recovery (IR); (2) Fat-Sat; (3) spectral-spatial excitation; and (4) Dixon methods. Although this is not the only classification approach usable, it appears to be more than sufficient in our case. Excepting application in humans, these techniques can be employed for preclinical purposes on small mammals, including mice, rats, rabbits, and others. As mentioned earlier, the amount of fat in the tissue can be applied as a biomarker in specific cases; on the other hand, however, the fat can contaminate the MR signal and sometimes can impede proper diagnostics.

More concretely, we can point to IR methods (Chapter 4.4) in the first place. In this context, the original method consists in the Short-Time Inversion Recovery (STIR); other related techniques, such as the SPIR (characterized by the use of spectral selective pulses) and SPAIR (with spectral selective adiabatic pulses), are directly derived from this primary procedure. Inversion recovery methods exploit the fact that the $T_1$ relaxation of fat is much shorter compared to that of tissues (brain, muscles, organs, etc.). If a suitable inversion time is adjusted, the fat can be suppressed. The methods can be used in conjunction with other MR techniques, for instance the gradient echo (GRE), the fast spin echo (FSE), and the single-shot FSE (SSFSE) approaches. The research of IR methods is focused on the optimalization of parameters to facilitate particular clinical applications and the achievement of best fat or water suppression possible; as already indicated above, the target fields include, among others, abdominal MR imaging [34], magnetic resonance angiography [35], cardiology [36], [37], and the research of liver diseases [38]. At this point, it is necessary to accentuate the fact that the approach with adiabatic pulses is very popular because an adiabatic RF pulse ensures homogeneous excitation of the $\mathbf{B}_1$ field over the sample. This field is very important for successful fat suppression. The principle of IR-based methods excludes the use of specific contrast agents; however, this problem can be solved via chemical shift selective (CHESS) imaging or, in other words, the Fat-Sat (fat saturation, Chapter 4.5). Fat saturation methods exploit a chemical shift between fat and water. In the case of the Fat-Sat method, the fat (or water) component is flipped into the transversal plane and crushed by the gradient, whereas the water (or fat) remains unaffected. Thanks to this principle, the Fat-Sat method can be used along with contrast-enhanced imaging and is much faster compared to IR techniques. The Fat-

Sat method is suitable for combination with fast imaging methods, e.g., the FLASH method. At present, the Fat-Sat and IR techniques are built into many clinical protocols in the form of "modules". Another interesting approach lies in the use of spectral-spatial (SPSP) selective RF pulses for water or fat suppression in which the water/fat can be excited while other spectral components are unaffected (Chapter 4.6). SPSP pulses are frequently combined with fast imaging methods, for example echo planar imaging (EPI) or spoiled gradient echo (SPGR). Importantly, a large number of publications were focused on binominal pulses [39] (a special group of composite pulses). Currently, SPSP pulses are very frequently employed in conjunction with steady state free precession (SSFP) methods, which provide short measurement times and a high signal-to-noise ratio (SNR). The most interesting group of water/fat separation techniques can be identified in Dixon methods; their principle is described in detail within Chapter 4.7. Dixon methods are very flexible and can be built into many imaging sequences; the range of clinical applications is practically unlimited. The magnetic field inhomogeneity owing to instability of the MR system or susceptibility influences is a major challenge for Dixon methods. Since the inception of these methods, research has been continually focused on finding the field inhomogeneity and reducing the measurement time.

# 3. Aim of the Thesis

In preclinical research, small animals are frequently used for the testing of drugs or animal models of diseases. Therefore, the use of a high field (4.7 T or more) is one of the techniques to increase the sensitivity. A high field nevertheless brings about specific problems, such as a stronger magnetic field inhomogeneity due to the differing susceptibility at the boundary between environments with diverse magnetic susceptibilities; on the other hand, it is also true that a high magnetic field leads to the high sensitivity, and the water-fat chemical shift is increased. The magnetic field inhomogeneity ($\mathbf{B}_0$) in Dixon-based methods causes problems during the reconstruction process, and the measurement must be as short as possible because the animal is anesthetized.

The aim of the thesis is to extend and implement modern MRI methods for water/fat separation and, consequently, to verify these techniques on phantoms and animal subjects at high fields (9.4 T) at the Institute of Scientific Instruments (ISI), Brno. The thesis assumes the modification or creation of a new fast Dixon sequence for water and fat separation; the implementation of the method on a 9.4 T MRI system; the verification on a phantom; and, finally, the eventual application in animals.

# 4. Survey of Current Water-Fat Imaging Methods

MRI is a significant diagnostic method for clinical medicine, and it chiefly provides excellent contrast between soft tissues in dependence on the molecular bonding between water/fat and the examined tissue. As mentioned in the introduction, fat often forms a substantial part of the human body and can be a significant biomarker [40] of the patient's health. Hence, fat suppression is widely used in MR imaging for the elimination or detection/imaging of adipose tissue. In practice, three principal fat suppression techniques are available: fat saturation, inversion recovery, and opposed-phase imaging [41]. According to Bley et al. [42], fat suppression and water-fat imaging methods can be categorized as follows: chemically selective fat suppression pulses "Fat-Sat"; spatial-spectral pulses (water excitation); short time inversion recovery (STIR) imaging; chemical shift-based water-fat separation methods; and fat suppression and balanced steady-state free precession (SSFP) sequences. The selection of a method for fat suppression or water-fat imaging depends on the clinical application, and each such approach has its advantages and disadvantages resulting from its physical background. A brief overview of the advantages/disadvantages and applications of each method is presented in Tab. 2 (adopted from Bley et al.). Generally, fat is bright in clinical images, and it may hamper the discernment of major pathologies such as tumour, edema, or inflammation; this problem is caused by a relatively short $T_1$ relaxation (240 to 280 ms [17]). Fat suppression methods, embedded into many clinical protocols, constitute an effective solution to the above-discussed issue, and the visualization of abnormalities in a normal tissue can thus be significantly improved [42]. One of the benefits of fat suppression consists in the elimination of chemical shift artefacts in clinical images. Together with direct visualization of fat, this can improve the detection of pathologies (such as fatty tumours and other fat-containing tumours), and it is possible to quantify and evaluate the amount of various kinds of adipose tissue [43], [44], [45], infiltrated fat in the tissue/organs in the case of fatty infiltrated liver diseases [46], [47], [48], [49], [50], or the amount of myocardial fat [51], [52], [53]. Many other clinical applications are also available (breast, knee, bone marrow [40], or optical nerves [54], [55]). If we understand the physical background of water-fat imaging methods, we can correctly estimate which method best suits our clinical application.

| Method | Advantages | Disadvantages | Suggested applications |
|---|---|---|---|
| Chemically selective fat suppression | • Versatile<br>• Relatively fast<br>• Applicable to most pulse sequences | • Sensitive to $B_0$ and $B_1$ inhomogeneities<br>• Low sequence efficiency | • Most applications except:<br>• Head and neck<br>• Mediastinum<br>• Extremities with metal implants |
| Spatial-spectral pulses, water excitation | • Insensitive to $B_1$ inhomogeneities<br>• Versatile<br>• Relatively fast<br>• Practical to most pulse sequences except FSE | • Sensitive to $B_0$ inhomogeneities<br>• Low sequence efficiency<br>• Longer excitation pulses | • 3D imaging of cartilage in knee<br>• Most applications except:<br>• Head and neck<br>• Mediastinum<br>• Extremities |
| STIR | • Robust to $B_0$ and $B_1$ inhomogeneities<br>• Reliable fat suppression | • Mixed contrast<br>• Inherent $T_1$weighting<br>• Only works with PD and $T_2$W<br>• Low SNR efficiency<br>• Suppresses short $T_1$ species and enhancing tissue after contrast | • Head and neck<br>• Chest<br>• Abdomen<br>• Extremities<br>• Large field of view<br>• Inhomogeneous $B_0$<br>• T2/PD applications |
| Chemical shift based water-fat separation | • Robust fat saturation<br>• Provides fat/water images<br>• Allows recombined images<br>• Corrects for chemical shift<br>• Universal compatibility<br>• Quantitative applications<br>• High SNR efficiency | • Long scan times<br>• More complex reconstruction | • Anywhere fat saturation and water excitation fail<br>• Anywhere fat information/ quantification is needed<br>• Hepatic steatosis<br>• Adnexal masses |
| SSFP methods | • Rapid<br>• High SNR<br>• Bright fluid | • $T_2/T_1$ mixed contrast<br>• Banding and flow artifacts from $B_0$ inhomogeneities<br>• "India Ink" artifact<br>• Currently under development<br>• Limited clinical experience | • NCE vascular imaging<br>• Bowel imaging<br>• New applications being explored |

**Tab. 2** The most commonly used methods for fat and water imaging [36].

## 4.3. Brief Physical Background

The chemical shift between water and fat is the key physical feature facilitating the separation of water and fat signals. The resonant frequency of nuclear spins is defined by the Larmor equation:

$$\omega_0 = \gamma \mathbf{B}_0 => f_0 = \frac{\gamma \mathbf{B}_0}{2\pi}. \quad (1)$$

For example, a nucleus with the spin of I = ½ has two energy states in the presence of a homogeneous external static magnetic field. These energy states are degenerated if the condition of an external homogeneous static magnetic field is not satisfied. In the molecules, the nuclei are not isolated from the other electrons, which are in motion and charged. Hence, the field of a nucleus is slightly different from the applied external static magnetic field $\mathbf{B}_0$; this slight difference is referred to as electron shielding, and such shielding then causes chemical shift. The electrons reduce the magnetic field of the nucleus, and this effect can be expressed by the equation of an effective magnetic field $\mathbf{B}_{\text{eff}}$ at the nucleus:

$$\mathbf{B}_{\text{eff}} = \mathbf{B}_0(1 - \sigma), \quad (2)$$

where $\sigma$ represents the electron shielding constant (the shielding or screening constant). The size of $\sigma$ (size in units of ppm) depends on the chemical environment of the nucleus [56], which means that equation (1) can be modified to

$$f_0 = \frac{\gamma}{2\pi}\mathbf{B}_0(1-\sigma). \quad (3)$$

The different electron shielding of protons in water molecules and triacylglycerol molecules of fat is caused by a different microscopic magnetic field, which means diverse resonance frequencies of protons in water and fat. Unlike water, fat exhibits a complex spectrum with several peaks (Fig. 2), where one of these elements is dominant. The fat signal is shifted to a lower frequency onto the water peak. A significant preponderance of signal energy is contained in the main peak, but for precise quantification we also need to consider the other peaks of fat. In the frequency domain, the chemical shift between fat and water is their difference:

$$\Delta f_{\mathrm{CS}} = f_{\mathrm{W}} - f_{\mathrm{F}} = \gamma \boldsymbol{B}_0 \cdot \Delta\delta[\mathrm{ppm}] \cdot 10^{-6}, \quad (4)$$

where $\Delta\delta$ is the chemical shift between water and fat. The chemical shift between the main fat and water peaks is approximately 3.5 ppm, as mentioned in the introductory chapter. For example, the chemical shift between water and fat is ≈ 1400 Hz at 9.4 T. However, let us also stress the fact that chemical shift is sensitive to the local temperature. This fact was first observed by Hindman in 1966 [57] during the study of intermolecular forces and hydrogen bond formation between water molecules [58]; furthermore, for example, Baxter and Williamson [59] measured and discussed in their study the temperature dependence of $^1$H chemical shifts in proteins. Generally, temperature dependence must be considered within fat suppression and water-fat imaging in a phantom or tissue because the phantom temperature can be different from that of the tissue. In a 1.5 T system, "*the chemical shift between water and the main fat peak is -210 Hz at body temperature (≈ 37°C), and -224 Hz at 22°C*" [42].

Each method for fat suppression or water-fat separation is sensitive in a certain manner to the static magnetic field $\mathbf{B}_0$ or $\mathbf{B}_1$ (the RF excitation field) inhomogeneity. Hence, we have to ensure good homogeneity of $\mathbf{B}_0$ and $\mathbf{B}_1$. In general terms, there are several factors which can cause inhomogeneity in the image of the static magnetic field $\mathbf{B}_0$.

The homogeneity $\mathbf{B}_0$ depends on the homogeneity of the self-magnet in the MR scanner. An imperfect magnetic field in the magnet can be shimmed, and in modern scanners the inhomogeneity of $\mathbf{B}_0$ is smaller than 1 ppm through the field of view (FOV). Another (and a very significant) source of the $\mathbf{B}_0$ inhomogeneity is the different susceptibility at the boundaries between the tissue/air/bone/fat; this effect can be observed in lungs, ears, oral and nasal cavities, entrails, knees, and many other points in the human or animal body. The contrast agent injected into the bloodstream and blood (with or without oxygen) exhibits a slightly different susceptibility too. Additionally, metal implants cause distortion in the static magnetic field; such distortion leads to a change of the resonance frequency. Also, several methods assume the same resonant frequencies for fat and water, which can cause errors in reconstructed water and fat images. The magnetic susceptibility $\chi_m$ is a physical quantity characterized by the following relationship between the magnetic moment (magnetization) of the material and the applied magnetic field:

$$\chi_{\mathrm{m}} = \frac{\mathbf{M}}{\mathbf{H}}, \tag{5}$$

where **M** (sometimes denoted as J) is the magnetization, and **H** is the magnetic field intensity. The magnetic flux density **B** can be derived from equation (5):

$$\chi_{\mathrm{m}} = \frac{\frac{\mathbf{M}}{\mathbf{B}}}{\mu} = \frac{\mathbf{M}}{\frac{\mathbf{B}}{\mu_0(1+\chi_{\mathrm{m}})}} \Rightarrow \mathbf{B} = \mu_0(\mathbf{M}+\mathbf{H}) = \mu\mathbf{H} = \mu_0(1+\chi_{\mathrm{m}})\mathbf{H}, \tag{6}$$

where $\mu_0$ is the magnetic permeability in vacuum, and $(1+\chi_{\mathrm{m}})$ is the permeability $\mu_{\mathrm{r}}$ of the material. It is obvious from the equation of magnetic susceptibility that susceptibility depends on the magnetic field strength. In high fields, this fact leads to stronger sensitivity to inhomogeneities, and the condition is caused by susceptibility. The inhomogeneity of the static magnetic field leads to: image distortion in the frequency encoding (readout) direction (the spins can be spatially encoded at the wrong position [60] during frequency encoding); faster $T_2^*$ decay for imaging methods based on the gradient echo, resulting in a lower intensity; and finally imperfect fat or water suppression owing to the frequency shift. As all these effects can cause significant problems in fat suppression and water-fat imaging, they must be seriously considered. The effect of the $\mathbf{B}_0$ inhomogeneity is shown in Fig. 3.

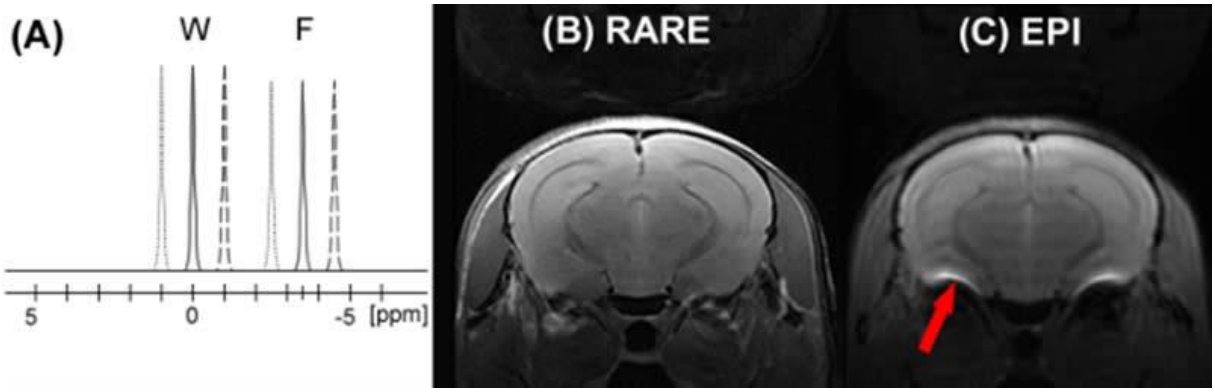


**Fig. 3** (A) The simplified water-fat spectrum (full line) for $\mathbf{B}_0$ without an inhomogeneity. The inhomogeneity of $\mathbf{B}_0$ can shift the water-fat spectrum to left or right (dashed and dotted lines). (B), (C) Images of a mouse brain at the 9.4 T field. The Rapid Acquisition with Relaxation Enhancement (RARE) sequence is insensitive to the $\mathbf{B}_0$ inhomogeneity compared to the Echo Planar Imaging – Diffusion Weighted (EPI-DW) sequence, which is sensitive to this inhomogeneity. The $\mathbf{B}_0$ inhomogeneity is caused by different susceptibilities on the boundary between air and the brain tissue. The $\mathbf{B}_0$ inhomogeneity appears in the image as a deformation (red arrow). The tissue (e.g., muscle) and the adipose tissue exhibit slightly different susceptibilities, which means a small deformation of the $\mathbf{B}_0$ field.

The $\mathbf{B}_1$ field inhomogeneity perpendicular to the $\mathbf{B}_0$ field is important for homogeneous excitation over the sample. The $\mathbf{B}_1$ inhomogeneity resulted in different flip angles at various locations of the excited sample and led to different intensities over the image, creating problems for some fat suppression methods. In the case of surface coils, the $\mathbf{B}_1$ field inhomogeneity of a coil in the receive mode does not constitute an obstacle and can be compensated through the use of sensitivity correction algorithms, which can be built into MR scanners. Ensuring homogeneous excitation is a problematic task in surface coils; therefore, the combination of a volume coil (as the transceiver, low sensitivity) with a surface coil (as the receiver, high sensitivity) is frequently used. The volume-surface coil combination

provides homogeneous excitation over the sample together with a high sensitivity. Hence, this coil combination is common in clinical MR imaging. A coil transmit $\mathbf{B}_1$ inhomogeneity can be reduced through a better RF coil design [5], [61], [62]; compensation of the RF pulse designs (e.g., adiabatic, small-tip-angle tailored RF (TRF)) [63], [64], [65], [66], [67], [68]; and via post-processing image correction [69], [70]. A transmit $\mathbf{B}_1$ inhomogeneity is more important than a receive $\mathbf{B}_1$ inhomogeneity (Fig. 4).

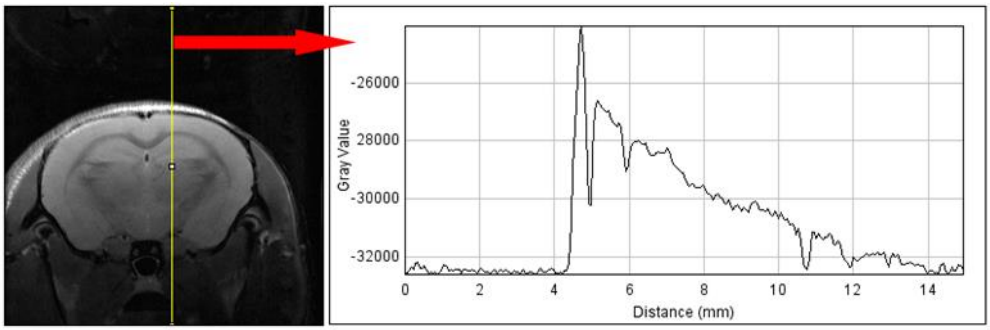


**Fig. 4** If a surface coil is used, the profile of the image (yellow line) shows the effect of a receive $\mathbf{B}_1$ inhomogeneity on the image of a mouse head.

## 4.4. Short Inversion -Time Inversion Recovery

It is a well-known fact that the Inversion Recovery (IR) method provides heavily $T_1$-weighted images. In 1985, Bydder and Young published an important modification of the inversion recovery (IR) method and showed very practical clinical applications [71], [72], [73]. This technique was denoted as STIR. The Short inversion-Time Inversion Recovery (STIR) method enables us to suppress fat signal because the longitudinal relaxation times $T_1$ of fat and water in a tissue are different. The STIR sequence (and related modifications) is based on the difference in $T_1$ relaxation times between water and lipids (fat). The $T_1$ relaxation of fat is much shorter in comparison with the $T_1$ relaxation time of water [17]. In the STIR sequence, the inversion time ($T_I$) is timed such that the fat signal is nulled ($M_{Z(F)} = 0$) and the water signal in the tissue ($M_{Z(W)} \neq 0$) is flipped (180°) into the transversal plane (Fig. 5; left diagram). The STIR sequence is frequently used with $T_2$-weighted (T2W) and proton density-weighted (PDW) sequences, for example the spin echo (SE) or fast-spin echo (FSE) ones. The STIR sequence produces a high soft-tissue contrast owing to the nulling of the adipose tissue signal and improves the contrast between the metastases and the normal surrounding tissue, e.g., in liver [73]. The use of contrast agents with similar $T_1$ relaxation times is a problematic step because these agents will be suppressed together with the fatty tissue. Hence, the method is unsuitable for application in contrast-enhanced MR imaging. Certain problems can occur with contrast agents exhibiting the same or a similar $T_1$, for example in a fatty tissue. In this case, the signal of the contrast agents will be suppressed together with the fatty tissue signal. The $T_1$ relaxation time increases, and the $T_2$ relaxation time decreases with the main magnetic field strength. In the STIR sequence, the inversion time $T_I$ must be chosen precisely for the maximum possible fat suppression. Kaldoudi et al. [74] presented a hybrid fat suppression method (CSS-IR (chemical shift selective-inversion recovery)) which combines the principles of the STIR and chemical shift selective imaging (CHEES, Fat-Sat). The conclusions

proposed within the above-mentioned study [74] were further developed by Tanabe et al., who extended Kaldoudi's sequence to introduce Dual-FS-STIR-CHESS [75]. Hybrid methods secure robustness in clinical MR imaging, especially when compared to conventional fat suppression methods. The principle of STIR is also used in the fluid-attenuated inversion recovery (FLAIR) sequence (Fig. 5, middle diagram), except that the fluid has a long $T_1$. In this case, the fluid is suppressed, as can be seen in Fig. 5 (C), (D).

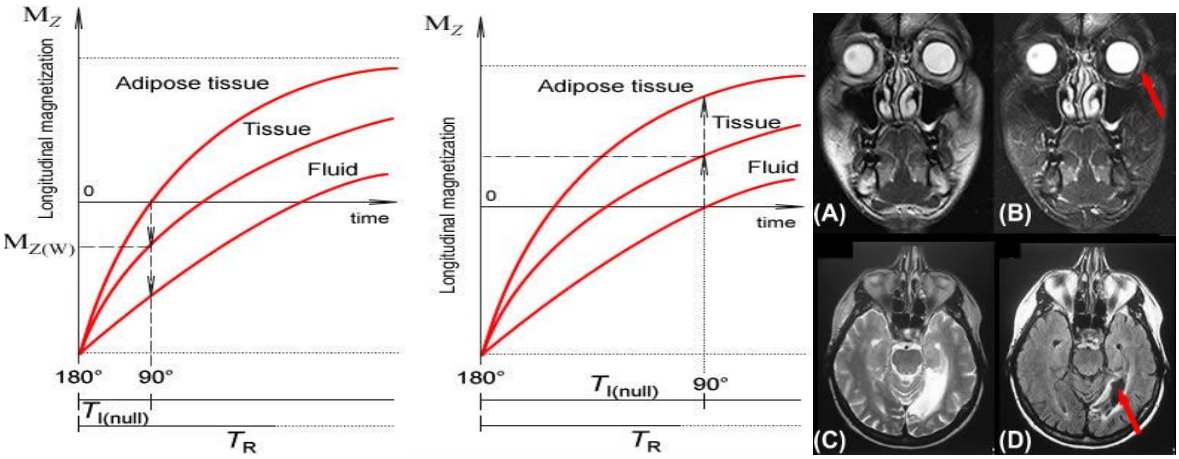


**Fig. 5** The left diagram shows the progress of longitudinal magnetization in time for an adipose tissue during the STIR sequence, and the middle diagram presents the longitudinal magnetization behaviour of fluid (free water) during the FLAIR sequence. The clinical images (A) and (B) show oblique-coronal images of head obtained with the STIR-FSE ($T_I$ = 50, 170 ms) sequence (the fat around the eye is suppressed for $T_I$ = 170 ms) [75]. The clinical images (C) and (D) represent a transversal image of a head measured by the FSE, where (C) is the FSE without FLAIR preparation, and (D) shows the FLAIR preparation part [76].

The main advantage of the STIR method lies in its insensitivity to $\mathbf{B}_0$ inhomogeneity and uniform fat suppression over the sample. The STIR method can be used in low-field-strength magnets. The differences in the relaxation times $T_1$ and $T_2$ contribute to the contrast in the STIR image; thus, the contrast is very good, and a tissue with long relaxations appears very bright [41], [71].

The STIR technique is based on the relaxation principle. The fat in the body is more complex, and several fats (peaks in the spectrum) have different relaxation times $T_1$; this means that such instances of "other fat" cannot be suppressed for a specific $T_{I(null)}$. Therefore, it is necessary to employ optimized inversion time for specific clinical applications or to combine it with other fat suppression principles (hybrid sequence [74], [75].). The measured signal is appropriate for longitudinal magnetization, and the water signal is partially saturated; thus, a lower signal-to-noise ratio (SNR) is achieved. The SPIR method requires homogenous excitation over the selected FOV. The non-fulfillment of this condition leads to non-uniform fat suppression over the image. The sensitivity of the sequence to $\mathbf{B}_1$ inhomogeneity can be solved using an inversion adiabatic pulse, which provides homogeneous excitation over the sample. Another source of $\mathbf{B}_1$ inhomogeneity is the dielectric effect [77]. Despite these drawbacks, the STIR is a practical method facilitating a wide range of clinical applications.

To improve the effectivity of the STIR approach, modifications (hybrid methods) of this method were introduced. In the STIR technique, the water signal is partially saturated

(Fig. 6(A) – dashed line), and the adipose tissue, whose relaxation is identical with that of the fat, will be suppressed (Fig. 6(A) – dotted line). The SPECtral Inversion At Lipid (SPECIAL) method provides an unsaturated water signal because, in this technique (Fig. 6(B)), a spectrally-selective RF inversion pulse is used that inverts fat magnetization only. Another benefit consists in an unsuppressed signal from a non-adipose tissue with the same $T_1$ relaxation as the adipose tissue.

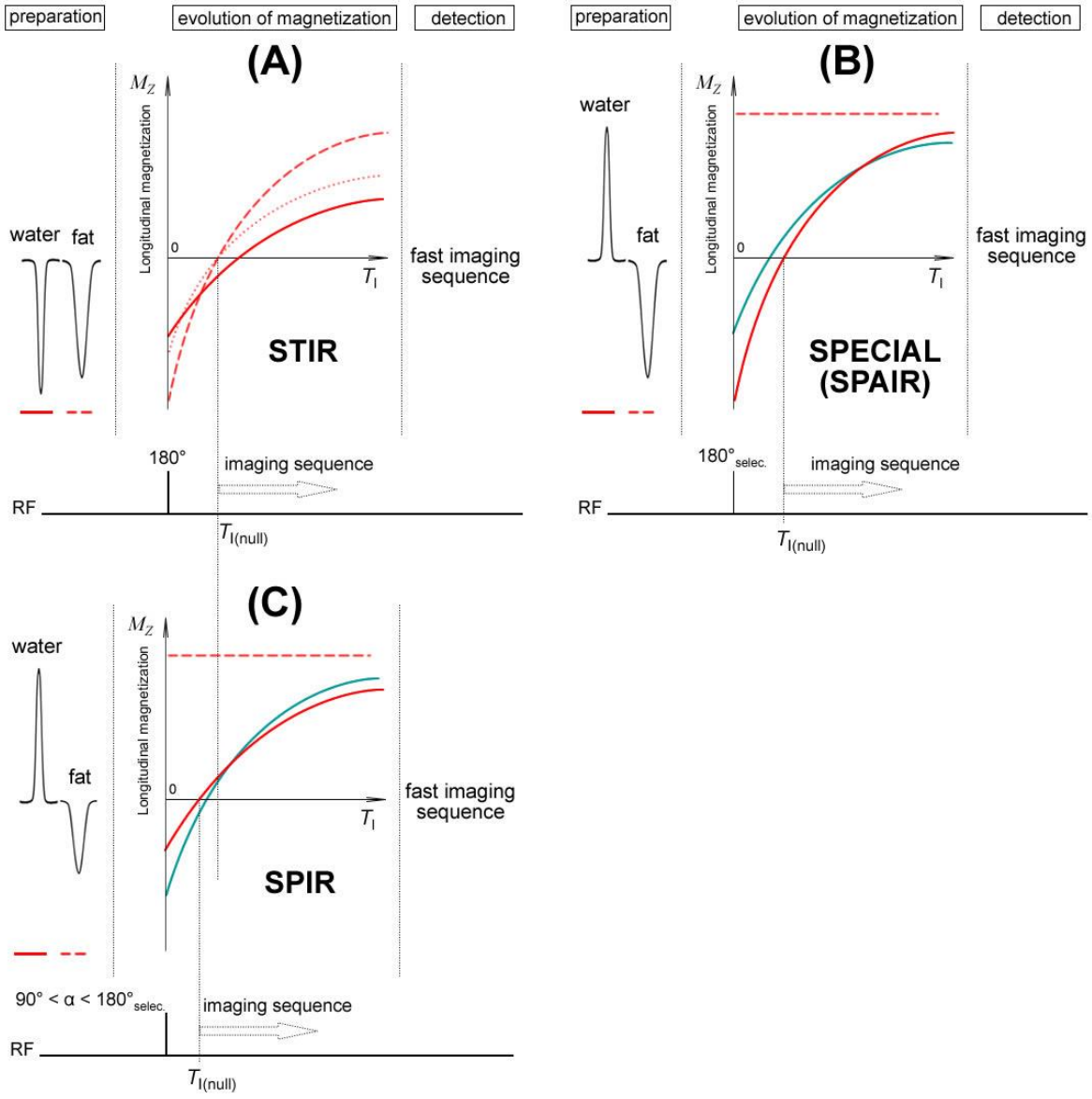


**Fig. 6** Each diagram shows three time periods: (A) The STIR method comprises only a non-selective inversion 180° RF pulse. The water and fat components are inversed. In the time $T_{I(null)}$, the longitudinal magnetization of fat is nulled, and a standard imaging sequence can be applied. The water component is partially saturated. (B) If we applied a spectrally-selective 180° inversion RF pulse, only the fat component would be inversed (SPECIAL). The water component is unaffected. This method is still time-consuming. (C) The SPIR method uses an inversion pulse close to 90°, which leads to a shorter $T_{I(null)}$. The $\mathbf{B}_1$ inhomogeneity causes different flip angles in different locations of the selected slice, and this practically means a shift of $T_{1(null)}$ – green lines in (B) and (C). The SPAIR method uses an adiabatic pulse, which results in insensitivity to $\mathbf{B}_1$ inhomogeneity.

The STIR and SPECIAL methods are time-consuming; this problem is suitably solved by means of the Spectral Pre-saturation with Inversion Recovery (SPIR) sequence (Fig. 6(B)). The inversion spectrally-selective RF pulse is close to 90°, which means that the inversion time $T_{I(null)}$ can be shorter compared to the $T_{I(null)}$ in the STIR method. Hence, the acquisition time of the preparation part will be shorter. The principle of the SPIR is clearly shown in Fig. **6**(C). The shift of the $T_{I(null)}$ point due to $\mathbf{B}_1$ inhomogeneity leads to incorrect fat suppression in the image.

The actual extension of the SPIR (or SPECIAL) technique is called the SPectral Attenuated Inversion Recovery (SPAIR) or the SPectral Adiabatic Inversion Recovery method (Fig. 6(C) – the adiabatic inversion RF pulse). The $\mathbf{B}_1$ inhomogeneity causes significant problems; therefore, the use of an adiabatic inversion pulse solves the issue of $\mathbf{B}_1$ sensitivity. The adiabatic pulses exhibit special properties and, as such, they are fundamentally different from other RF pulses. In the case of adiabatic pulses, when RF power exceeds a certain value, the flip angle will be constant. Adiabatic pulses are amplitude- and frequency-modulated pulses insensitive to the $\mathbf{B}_1$ inhomogeneity and frequency offset [78], [79]. The design of adiabatic pulses is complicated, and for more than a decade, considerable effort has been focused on the design of modulation functions which maximize the inequality of the adiabatic condition [80]. For our purpose, it is sufficient suffices to know that an adiabatic pulse is insensitive to $\mathbf{B}_1$ inhomogeneity. The homogeneous $\mathbf{B}_1$ field excitation leads to better fat suppression based on adiabatic pulse. The adiabatic pulse in the SPAIR technique is frequency-selective, and the use of a frequency-selective RF pulse yields another positive effect. The IR based methods including a frequency-selective pulse can be used in contrast-enhanced MR imaging; the frequency-selective pulse is placed on the centre of the main fat peak, and therefore a small fraction of fat will be contained in the image.

## 4.5. Fat Saturation (Fat-Sat)

The fat saturation method (Fat-Sat) is a frequency-selective excitation method for fat suppression. This procedure selectively saturates fat protons, and water protons will be unaffected if we ensure certain specific conditions (good $\mathbf{B}_0$ and $\mathbf{B}_1$ homogeneity). The Fat-Sat, or CHEmically Shift Selective (CHESS) imaging to be used for selective suppression fat, was presented by Haase et al. [81] in 1985. Generally, CHESS can be utilized for the suppression of a specific spectral component.

The principle of CHESS is shown in Fig. 7(A). In this technique, a selective 90° RF pulse (e.g., fat) is applied, and longitudinal magnetization is flipped into the transversal plane; subsequently, the crusher (dephasing) gradient is applied. The RF selective pulse is centered at the main fat peak, and the shape of the RF pulse is often *sinc* or a related function (in the time domain). Therefore, the shape of the pulse in the frequency domain (the Fourier transform (FT) of the time domain) will be a rectangle, which means that the main part of the RF energy is located at the main fat peak and the water protons will be unaffected. The dephasing of the spins flipped into the transversal plane due to the crusher gradient leads to fat saturation. After the chemically selective RF pulse and the crusher gradient (CHESS period), the imaging sequence follows. The time of the crusher gradient is very short, but

small longitudinal magnetization occurs during this period. The fat saturation method works perfectly in regions where the $\mathbf{B}_1$ and $\mathbf{B}_0$ homogeneity is relatively good. Similarly to the STIR method, the use of an adiabatic RF saturation pulse eliminates the sensitivity to $\mathbf{B}_1$ inhomogeneity.

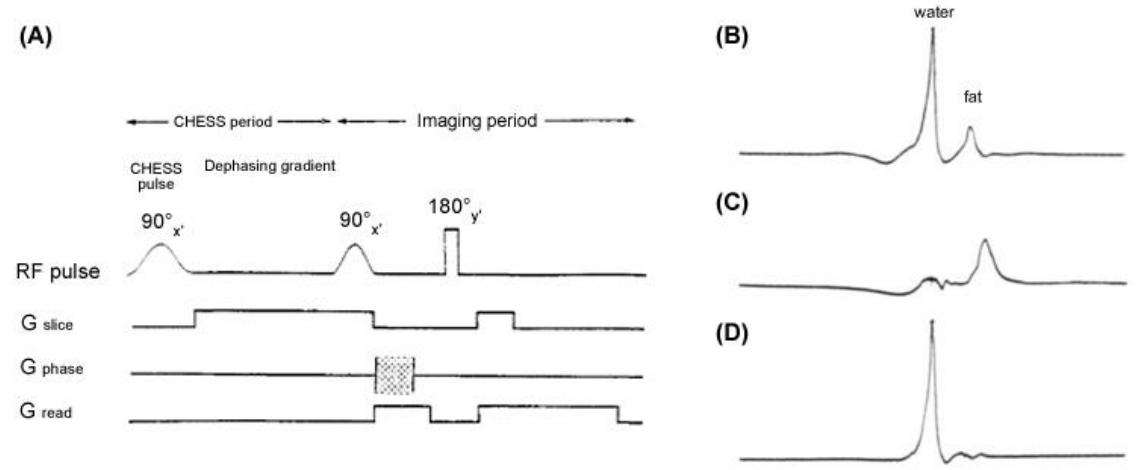


**Fig. 7** (A) The original time diagram of CHESS imaging; (B) the normal spectrum of a human hand (without the CHESS period); (C) the fat spectrum after application of CHESS (selective elimination of water resonance); (D) the water spectrum after CHESS had been applied to fat resonance. [74].

Fat saturation is a chemical shift selective method; therefore, the combination with contrast-enhancement ($T_1$-weighted) MR imaging is possible, and addition is suitable for areas with a large amount of fat. The use of fat saturation can eliminate the problem of chemical shift artefacts. The signal of the non-adipose tissue is unaffected if good homogeneity of the $\mathbf{B}_1$ and $\mathbf{B}_0$ fields is assumed. The SNR of the adipose tissue will be logically lower. Only a single imaging experiment is necessary to obtain water or fat image. The Fat-Sat can be used for other nuclei and is easily combinable with various imaging sequences. The high field leads to the widening of the spectrum, and the frequency shift between water and fat is increased ($f$ for 3.5 ppm (calculated from equation (4)) at 9.4 T: $\Delta f_{\mathrm{CS}} \approx 1400$ Hz; 3 T: $\Delta f_{\mathrm{CS}} \approx 447$ Hz).

Field inhomogeneity is a significant problem of Fat-Sat imaging. The static field inhomogeneity $\mathbf{B}_0$ leads to a shift of the spectrum, which produces errors in Fat-Sat imaging. Examples of incorrect fat suppression owing to the $\mathbf{B}_0$ inhomogeneity are shown in Fig. 8(B), (C). An inhomogeneous excitation field $\mathbf{B}_1$ of the spins leads to different flip angles in different parts of the image. In this case, the flip angle will be lower than 90°, and this results in incomplete (partial) fat saturation (Fig. 8(D)). Referring to Mao et al. [82], Delfaut et al. [41] affirmed in their review that about 5 % of fats have the same frequency as water, but this affirmation is not correct. In the case of a low magnetic field, the fats close around the water peak can merge with this peak; therefore, the suppression of these fats can be a problematic task, and a higher magnetic field is preferred. A homogeneous $\mathbf{B}_1$ over a large FOV still remains a challenge and is necessary for correct fat suppression. The high field yields an increased chemical shift between fat and water, but the sensitivity to the $\mathbf{B}_0$ inhomogeneity is higher.

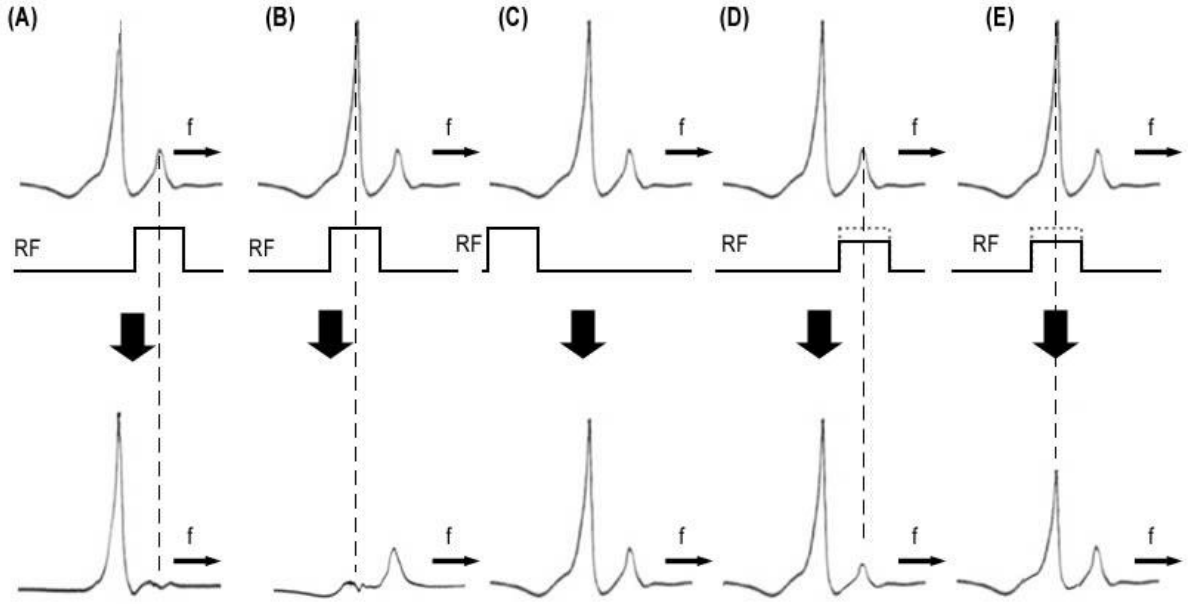


**Fig. 8** The images show influences of the $\mathbf{B}_0$ and $\mathbf{B}_1$ inhomogeneities on the fat saturation. In the case of good $\mathbf{B}_0$ and $\mathbf{B}_1$ homogeneity, the fat suppression will be correct, (A). A strong $\mathbf{B}_0$ inhomogeneity can lead to a shift of the spectrum and incorrect fat suppression, (B) and (C). The inhomogeneity of the $\mathbf{B}_1$ field results in incomplete fat saturation, (D). The worst case is a combination of the $\mathbf{B}_0$ and $\mathbf{B}_1$ inhomogeneities, (E). In clinical MRI, the combination of both inhomogeneities is common.

## 4.6. Spectral-Spatial Excitation

Another fat suppression approach consists in directly excited water [83], [84], [85]. In 1988, Pauly et al. [86] introduced a k-Space analysis of the small-tip angle and presented two new pulse types. The first was a slice-selective excitation pulse that is inherently refocused at the end of the excitation (gradient refocusing lobes are not needed), and the second one consisted in a pulse spatially selective in two dimensions. Immediately after this article (1990), Mayer and Pauly et al. [83] introduced spectral-spatial (SPSP) RF pulses for water/fat excitation. They showed the ability of SPSP RF pulses to be simultaneously selective in both the space and the resonant frequency in the context of water/fat excitation. Examples of these SPSP RF pulses are shown in Fig. 9. Generally, the SPSP pulses are used for replacing the combination of a spectral-selective presaturation pulse and an excitation pulse [82], but Zur [87] introduced another application, namely saturation.

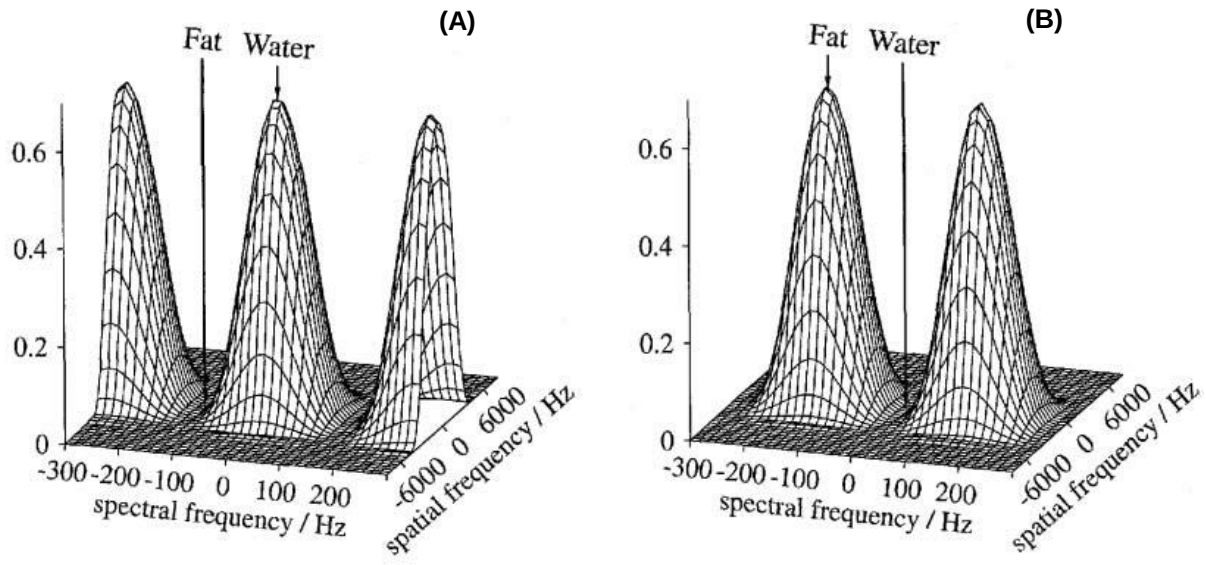


**Fig. 9** The examples of spectral-spatial RF excitation pulses [85]. The maximum excitation occurs at water frequency, and the fat is unaffected (A). The reverse case consists in excited fat and unaffected water (B).

*There are many variants of SPSP pulses, but all consist in multiple RF subpulses that are played under a broad RF envelope. The subpulses, together with a concurrent oscillating bipolar slice-selection gradient waveform, determine the spatial selectivity, whereas the RF envelope governs the spectral content. The spatial RF subpulses can be played under some, or all, of the gradient lobes. Time-varying gradients are required because a constant slice-selection gradient produces identical (but spatially offset) replicas of the slice profiles for chemical species such as lipids and water. The oscillating gradient can be sinusoidal in shape, but more commonly it is implemented with trapezoidal lobes* (Fig. 10(C)) *of alternating polarity. The trapezoid maximizes the area under the gradient lobes which allows for thinner slices.* [88]

The methods proposed by Mayer et al. [83] and Spielman et al. [84] use sine-shaped gradients combined with suitable RF pulses (Fig. 10(A)). The calculation of an RF pulse shape is relatively complicated for the off-centre slice position. In these cases, the moderate gradient slew rates are sufficient even for thin slices. The research group of Schick [89] introduced a different approach to spectral-spatial excitation of water or fat where *off-center slice positions can be achieved by using the conventional RF pulse processing of the image since all RF pulses are applied at the same slice-selection gradient amplitude. Only constant and linearly ramped gradients* (Fig. 10(B)) *(with relatively fast slew gradient) are required* [85]. In 1998, Schick et al. [85] proposed the first method allowing simultaneous water- and fat-selective imaging with spatial-spectral excitation in multi-slice acquisition.

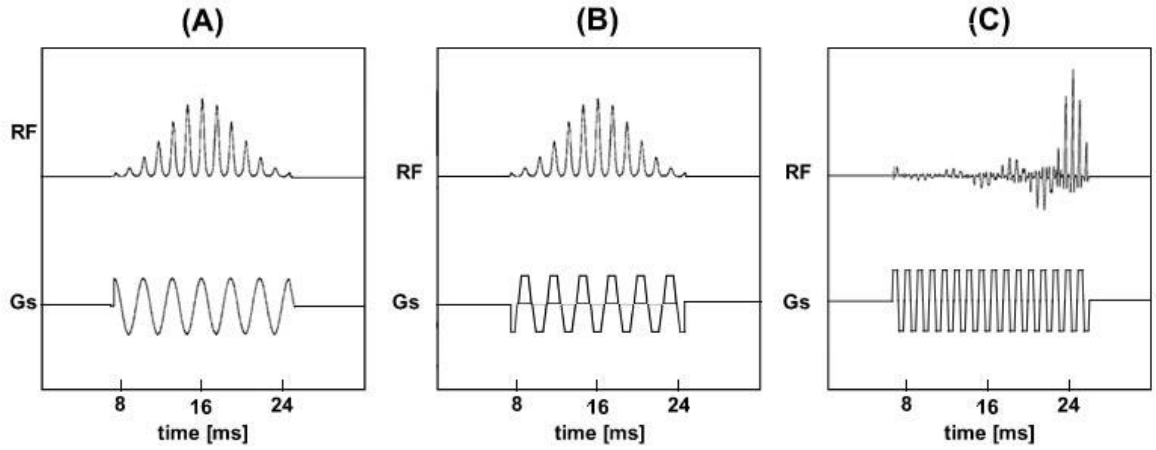


**Fig. 10** The examples of RF and gradients waveforms for SPSP pulses with Gaussian profiles, (A) and (B). The first case is for a sine-shaped gradient, (A), and the second one exhibits ramped gradients, (B). (C) shows the trapezoid profile of SPSP pulses.

The principle of a typical sequence with SPSP pulses for water/fat excitation can be explained easily, as follows. Consider the train of only spatially-selective RF pulses, each with a small flip angle $\alpha$. The time interval between the RF pulses corresponds to the fat precession over $\pi$ rad relative to water, which practically means 354 μs at 9.4 T field because the period can be calculated as $T_{\alpha-\alpha} = 1/2\pi\Delta f_{wf}$. The behaviour of water and fat magnetization is shown in Fig. 11. After the first RF pulse, the water and fat magnetization are commonly flipped (e.g., 5°) from the *z*-axis. The fat is an off-resonance component, and during the $T_{\alpha-\alpha}$ period the fat precesses relative to water in the transverse plane. Therefore, only the water component is successively flipped to the transversal plane, and the fat is practically unaffected.

The use of the SPSP RF pulses yields a number of advantages. One of the most significant ones is better tolerance to $\mathbf{B}_1$ inhomogeneity in comparison with Fat-Saturation pulses, which require a good $\mathbf{B}_1$ inhomogeneity over the selected FOV. A sequence with SPSP RF pulses enables us to eliminate chemical shift artefacts in the image because only one spectral component is excited. The train of RF pulses is played under the time varying gradients (positive and negative lobes); therefore, the system is more prone to $\mathbf{B_0}$ inhomogeneity due to eddy currents. Eddy currents inauspiciously affect the $\mathbf{B}_0$ homogeneity and the gradient fields. An uncompensated eddy current leads to the k-space trajectory deviation of the theoretical k-space trajectory. When symmetric gradient switching is ensured, the eddy currents can be reduced. [90]. In addition to the perfect eddy current correction, the RF pulses and gradients waveforms must be exactly synchronized because the RF train playing during the gradient waveform causes the sensitivity of the offset SPSP pulses to small time mismatches (units of micro seconds) between the RF and gradients waveform. Zur [87] and Block et al. showed compensation and calibration methods applicable in errors due to mismatches between RF and gradient waveforms. *The short duration RF sub-pulses (individual pulses in the RF train) are not very spatially-selective.; therefore, the minimum-slice thickness is limited.* [88]

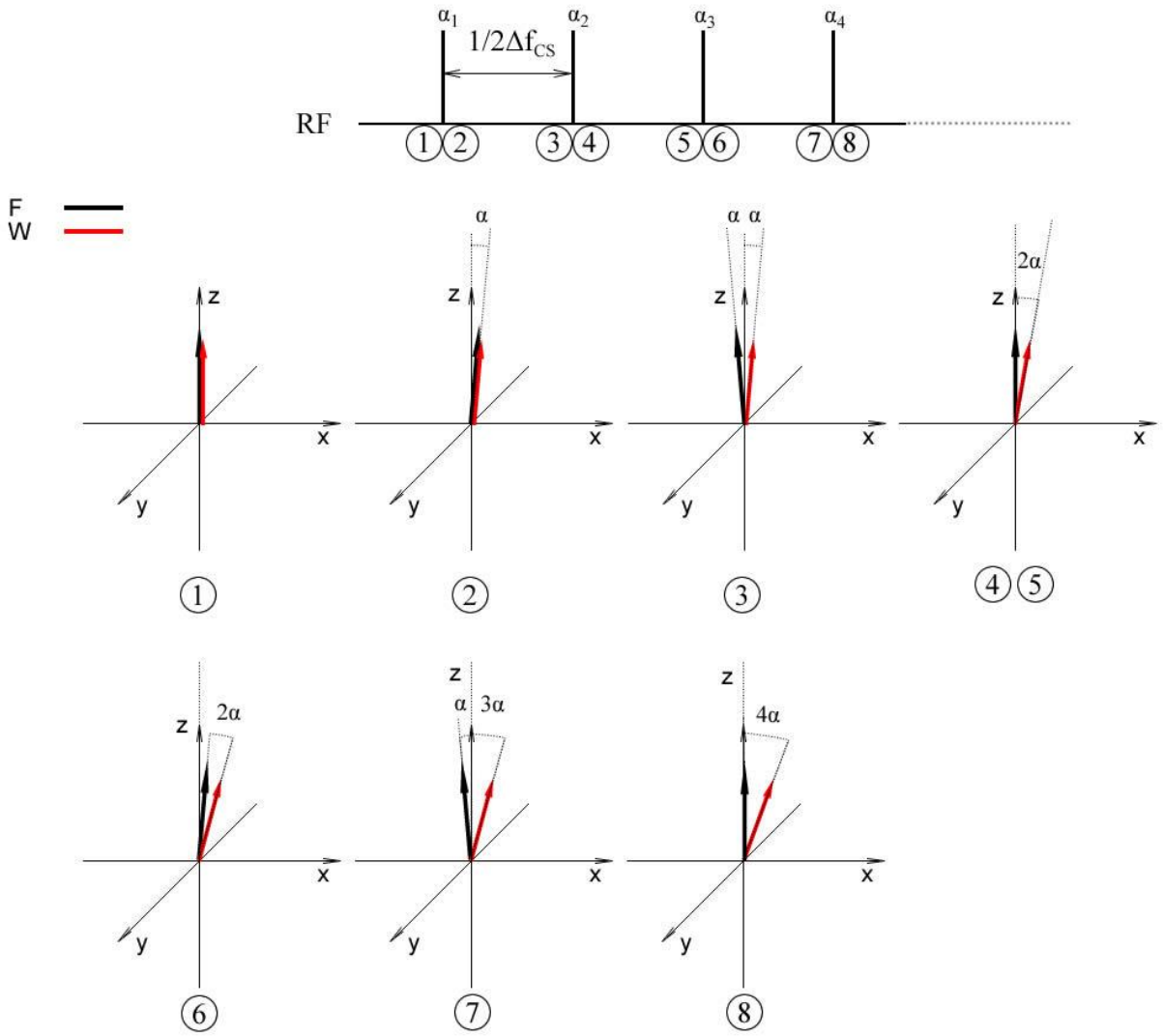


**Fig. 11** A schematic illustration of the spatial-selective pulses train shows the behaviour of water and fat magnetization. The time period between the RF pulses is $T = 1/(2\Delta f_{CS})$. The time corresponds to the 180° phase shift between water and fat. At the 9.4 T field, the time period between the RF pulses is 354 μs. The water and fat are flipped together (2), but after the time period *T*, when the phase shift between water and fat is 180° (3), the following RF pulse with same flip angle is applied. The fat is returned to the longitudinal plane, and the water component is flipped to the transversal plane (4). This process is repeated until the water is not fully flipped into the transversal plane.

The SPSP pulses are frequently combined with spiral and echo planar imaging [91], [92] or with other sequences such as the SPGR (spoiled gradient echo) [93] and the FSE (fast spin-echo) [94]. The conjunction of the SPSP pulses and the bSSFP (balanced steady state precession) sequence [95] is very attractive (appropriate) because the bSSFP is a fast imaging sequence with a high signal-to-noise ratio efficiency. The special group of composite pulses are binomial pulses [39] that are denoted according to binomial coefficients: (121), (1331) and many others. The mathematical description can be found in [88]. Binomial pulses appears suitable for many clinical applications such as cartilage imaging [96], [97], and musculoskeletal imaging [98], [99], [42]

The SPSP pulses at high fields yield some advantages. In the case of a high field, the frequency shift between water and fat is determined by equation (4); therefore, the RF pulses

can be shorter (the spectral bandwidth BW of the RF pulse is increased). Another advantage is the lower sensitivity of the pulses to the $\mathbf{B}_0$ inhomogeneity. It is also important to note that the time intervals between the subpulses will be shorter at a high field.

## 4.7. Dixon-Based Water-Fat Separation Methods

Dixon water-fat separation methods are chemical shift-based water-fat separation methods. Water protons precess faster between 3 and 4 ppm (the main fat peak) than fat protons, which results in different resonance water-fat frequencies equation (4). This difference is ≈ 1400 Hz at 9.4 T. The water-fat chemical shift, owing to different resonance frequencies between water and fat, leads to the water-fat phase shift. The discussed Dixon-based methods encode the water-fat chemical shift difference into the phase of the image, but water-fat separated images are obtained after the post-processing procedure.

In 1984, Thomas Dixon [100] introduced a new method for water-fat separation. This method already exploited differences in water and fat precession (Fig. 12(A)). If a 90° RF pulse is applied, the water and fat protons are flipped into the transversal plane. The total magnetization vector is the sum of water and fat magnetizations (Fig. 12(B)). The time behaviour of the transversal magnetization is shown in Fig. 12(C).

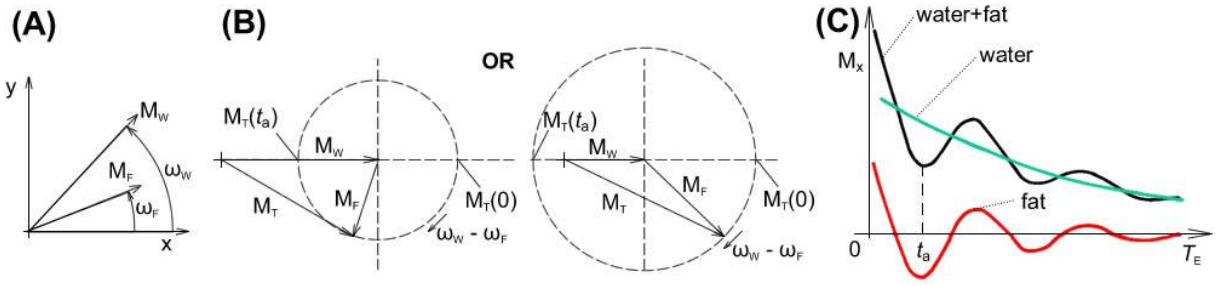


**Fig. 12** (A) The laboratory frame. (B) The magnetization vectors of fat in a rotating frame, left $|M_W| > |M_F|$, right $|M_W| < |M_F|$. (C) The free induction decay (FID) signal. [100]

The total magnetization $M_T$ is the sum of water and fat magnetizations. The rotating frame has the resonance frequency of water. The small differences in the resonance frequencies of water ($f_W$) and fat ($f_F$) lead to the rotation of fat in the rotating frame. At the beginning, $M_T(0)$, the water and fat are in phase. The magnetization goes through the first local minimum when fat and water are in opposite directions. The first local minimum occurs at [100]:

$$t = \frac{1}{2 \cdot (f_W - f_F)} = \frac{1}{2 \cdot (\Delta f_{CS})} \equiv t_a. \tag{7}$$

Another local maximum occurs at $2t_a$: water and fat then exhibit the same direction (in-phase). This time variation is periodical and depends on the different frequencies between water and fat. Simple summation or subtraction of the opposite-phase and the in-phase images is used to calculate a water-only or a fat-only image. Generally, this is a simple spectroscopic imaging concept.

The main problem of Dixon-based methods is the presence of a $\mathbf{B}_0$ inhomogeneity leading to phase errors in the acquired images. The phase errors in the in-phase and opposite-phase images result in incorrect water and fat separation; thus, phase correction is necessary for successful water-fat separation. Furthermore, Dixon methods require precise timing of the pulse sequence because the water/fat phase changes are relatively fast. At high fields (e.g., 9.4 T), the time between the in-phase (IF) and the opposite-phase (OP) images is much shorter compared to low fields (e.g., 1.5 T, 3 T). This fact follows from the above equation (7). The motion and incorrect pulse sequence timing cause the degradation of the obtained images [101].

In the past two decades, many Dixon-based water-fat decomposition methods have been proposed [102], [103], [104], [105], [106], [107], [108], [109], [110], [111], [112], [113], [114] to increase the robustness with respect to field inhomogeneity ($\mathbf{B}_0$ and $\mathbf{B}_1$). The problems affecting Dixon-based methods constitute a major topic, and multiple studies are focused on the correction of these drawbacks. Several procedures have been proposed to facilitate phase correction (post-processing algorithms, data acquisition, or a combination of both). Thus, the knowledge of the $\mathbf{B}_0$ inhomogeneity is crucial for correct water-fat separation. The phase correction and the data acquisition strategy are very significant for successful application of Dixon methods [101]. Significant development of Dixon-based methods has allowed their successful application in clinical MRI.

Dixon methods can be classified as single-point [115], two-point [106], [116], [117], [107], [110], [108], [118] and multipoint or triple ones [119], [103], [105], [111]; however, even higher variations are available [104], [120], [121], [122], [113]. The three or multipoint versions are preferred over the two-point variant when a short acquisition time is not required; in addition, they are more robust and enable more effective reconstruction of errors.

The signal model common for Dixon methods is represented by single delta function spectral peaks for water and fat. The signal model in the original 2PD method [100] was very simple and considered only two peaks (water and fat) without the presence of field inhomogeneity, system errors, and influences such as diffusion losses, intravoxel susceptibility losses, or losses due to spectral broadening. Thus, other improvements were proposed for field inhomogeneity estimation [102], [103], [104], [109], [123], [124]. Generally, the signal model often assumes only the two-peak form (water and fat); however, multi-peak models were developed to provide for higher accuracy. A more accurate signal model results in significant improvement of the fat fraction estimation, and therefore the quantification of fat [48], [125], [124], [123] in a tissue or phantom is more accurate.

### 4.7.1. General Analysis

We assume the spectrum $L(\omega)$ with two spectral components, namely $L_1(\omega)$ (water) and $L_2(\omega)$ (fat), (Fig. 13(A)). The integrated real-value intensities of these lines can be denoted as $\rho_1$ and $\rho_2$. The chemical shift between the water and fat components is $\omega_{CS} = 2\pi \cdot \Delta f_{CS}$.

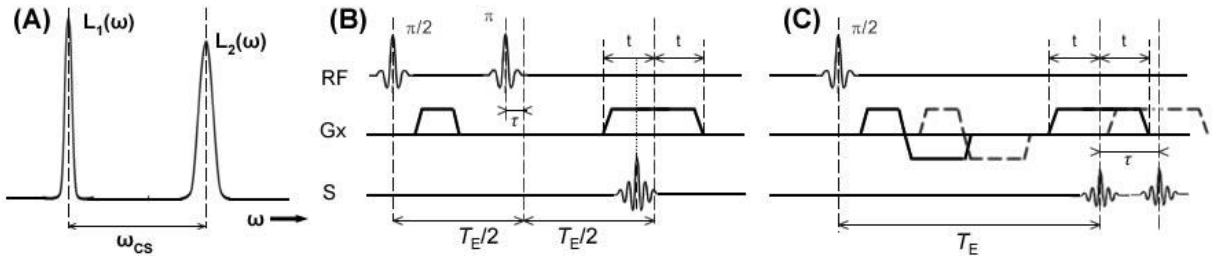


**Fig. 13** (A) The simplified spectrum of water and fat protons. (B) The spin-echo sequence and (C) the gradient echo sequence for N-point Dixon methods. The images show only two-phase encoding positions - 2PD.

The multipoint Dixon method can be performed using the gradient-echo sequence (GRE) or the spin-echo sequence (SE) (Fig. 13(B) and (C)). In the GRE, we consider the following aspects: when the $T_2$ is very short and comparable with the echo time ($T_E$), then the losses owing to the $T_2$ decay must be taken into account. For our purpose, it is important to assume the condition $T_2 \gg T_E$. In this case or in the spin echo, the signal ($S$) acquired from one voxel in the time $\tau$ is a mixture of the water and fat components [104], namely

$$\begin{gathered} \mathrm{M_T} = S_\mathrm{n}(\tau) = \left(\rho_1 \cdot \mathrm{A}_1(\tau) + \rho_2 \cdot \mathrm{A}_2(\tau)\mathrm{e}^{i\theta_n}\right) \cdot \mathrm{e}^{i(\varphi+\varphi_0)}, \\ \rho_1 \cdot \mathrm{A}_1(\tau) = \mathrm{M_W}, \\ \rho_2 \cdot \mathrm{A}_2(\tau) = \mathrm{M_F}, \end{gathered} \tag{8}$$

where $A_1$ and $A_2$ are the loss factors for water and fat, which depend on the $\tau$; $\theta$ is the phase difference between fat and water; $\varphi$ represents the $\mathbf{B}_0$ field inhomogeneity (e.g., an imperfect shim and the influence of susceptibility); and $\varphi_0$ is the phase error due to system imperfections such as the different signal time delay in the receive channels, spatial dependence of the RF penetration [101], and other systematic phase shifts. The amplitudes of the loss factors $A_1$ and $A_2$ are affected by diffusion, susceptibility dephasing, and spectral broadening [104]. The total losses for water or fat can be calculated as follows:

$$\mathrm{A}_m = \mathrm{A}_{m\mathrm{d}} \cdot \mathrm{A}_{ms} \cdot \mathrm{A}_{m\mathrm{w}}, \tag{9}$$

where $m$ = 1, 2; $A_d$ – the diffusion losses; $A_s$ – the intravoxel susceptibility losses; and $A_w$ – the losses due to spectral broadening. It follows from the above equation (7) that IP images are acquired in zero time or even multiples of $t_a$, and OP images are acquired in odd multiples of $t_a$. Generally, the phase difference $\theta$ is proportional to $\tau$, that is

$$\theta[\mathrm{rad}] = 2\pi \cdot \gamma \cdot \mathbf{B}_0 \cdot \Delta\delta[\mathrm{ppm}] \cdot 10^{-6} \cdot \tau = 2\pi \cdot \Delta f_{\mathrm{CS}} \cdot \tau. \tag{10}$$

The phase error is too proportional to $\tau$, and we have

$$\varphi = 2\pi \cdot \Delta\mathbf{B}_0 \cdot \tau, \tag{11}$$

where $\Delta\mathbf{B}_0$ is the magnitude of the field inhomogeneity.

### 4.7.2. Original Two-Point Dixon Method (2PD)

As mentioned in the introduction to Dixon water-fat separation methods, Dixon had introduced and explained the method based on the acquisition of two source images [100],

each with slightly different echo times ($T_E$). The 2PD method assumes $A_1 = A_2 = 1$. In the case of the two-point Dixon method, the images are obtained when the water and phase differences $\theta$ are 0 ($\tau = 0$) and $\pi$ ($\tau = t_a$). Thus, the acquired signals from one voxel can be expressed as

$$S_0 = S(0) = (\rho_1 + \rho_2) \cdot e^{i\varphi_0}, \tag{12}$$

$$S_1 = S(t_a) = (\rho_1 - \rho_2) \cdot e^{i(\varphi+\varphi_0)}. \tag{13}$$

The phase error $\varphi_0$ is independent of the chemical shift, and it can be determined from equation (12) as the argument of $S_0$ and consequently removed from equations (12), (13); we then have

$$S_0' \equiv S_0 \cdot e^{-i\varphi_0} = (\rho_1 + \rho_2), \tag{14}$$

$$S_1' \equiv S_1 \cdot e^{-i\varphi_0} = (\rho_1 - \rho_2) \cdot e^{i\varphi}. \tag{15}$$

The amount of fat and water in each pixel is important for calculating the "water" (*W*) and "fat" image (*F*). When the water-dominant voxel is assumed without the phase error, the water and fat images can be calculated such that

$$W = \frac{|S_0'| + |S_1'|}{2}, \tag{16}$$

$$F = \frac{|S_0'| - |S_1'|}{2}. \tag{17}$$

In the fat-dominant voxel without the phase error:

$$W = \frac{|S_0'| - |S_1'|}{2}, \tag{18}$$

$$F = \frac{|S_0'| + |S_1'|}{2}. \tag{19}$$

A disturbance of the phase error condition ($\varphi = 0$) results in misleading water and fat images calculated through the use of equations (16), (17) or (18), (19). Generally, the images calculated from $S_{IP}$ and $S_{OP}$ are images where each pixel contains a dominant signal of water or fat. In clinical MR images, the amounts of fat and water can be different for each pixel. Therefore, the practical problem of the two-point Dixon method lies in the decision of whether the calculated pixel of the image corresponds to a water or a fat signal. The success of the two-point Dixon method relates to the magnitude of the field inhomogeneity $\Delta\mathbf{B}_0$, which is proportional to the phase error (11). In the case of a strong magnetic field inhomogeneity, the calculated images are a mixture of fat and water signals. Another factor that can confound the water-fat decomposition is the $T_2$ decay of the signal at increasing echo times [126]. In the case of the gradient-echo method, the $T_2$ decay will be a major concern.

### 4.7.3. Multi-Point Dixon Methods

The presence of magnetic field inhomogeneity is a crucial problem of Dixon methods; therefore, Young and Kormos [102], Glover and Schneider [103], and Glover [104] showed the possibility of determining the field inhomogeneity (off-resonance, phase error) by acquiring an additional image. The original three-point Dixon (3PD) method [103] used the phase-encoding strategy (–π, 0, π). In the same year, Glover introduced the extended three-point Dixon (E3PD) method [104], where a new phase-encoding strategy was presented: (0, π, 2π). In the same article, the four-point Dixon (4PD) method was described.

#### *4.7.3.1. Three-point Dixon (3PD) method*

The method is based on the acquisition of three images under specific conditions, and it mainly constitutes an extension of the original two-point Dixon method. The 3PD method assumes $A_1 = A_2 = 1$, similarly as the 2PD. In the three-point Dixon method, three images ($S_1$, $S_0$, $S_1$) are acquired at an exactly defined time position, namely when the relative phase between water and fat is: (-π, 0, π). The $S_{-IP}$ image (-π phase) is acquired from the spin-echo sequence by shifting the refocusing RF pulse with respect to the conventional spin-echo that is centered between the RF excitation and acquisition. The pulse sequence is shown in Fig. **14**.

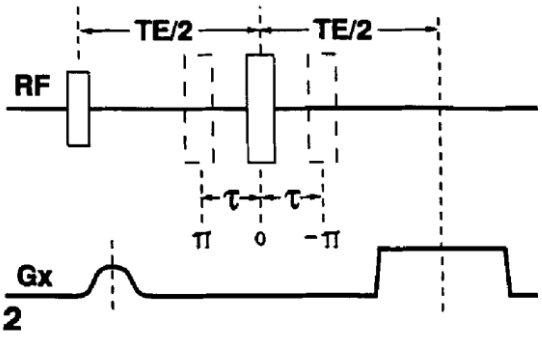


**Fig. 14** The pulse diagram of the spin-echo sequence used for the three-point Dixon method. The three different positions of the π pulse are used for the acquisition of three images ($S_{-1}$, $S_0$, and $S_1$). The echoes are symmetrically distributed about the spin-echo. [103]

The acquired signal from the third additional image (-π) can be written as follows:

$$S_{-1} = S(-t_a) = (\rho_1 - \rho_2) \cdot \mathrm{e}^{i(-\varphi+\varphi_0)}. \tag{20}$$

The phase error can be removed as before, thus

$$S'_{-1} \equiv S_{-1} \cdot e^{-i\varphi_0} = (\rho_1 - \rho_2) \cdot \mathrm{e}^{-i\varphi}, \tag{21}$$

$$S'_0 \equiv S_0 \cdot e^{-i\varphi_0} = (\rho_1 + \rho_2), \tag{22}$$

$$S'_1 \equiv S_1 \cdot e^{-i\varphi_0} = (\rho_1 - \rho_2) \cdot \mathrm{e}^{i\varphi}. \tag{23}$$

The additional equation (20) facilitates the determination of the phase error $\varphi$, and we have

$$S_1 \cdot S_{-1}^* = |\rho_1 - \rho_2|^2 \cdot e^{2\varphi} \Rightarrow \varphi = 0.5 \cdot \arg(S_1' \cdot S_{-1}'^*) = \frac{\arg(S_1') - \arg(S_{-1}')}{2} \quad (24)$$

The procedure for finding the above equation (24) is shown in Glover's and Schneider's [103] original paper. The phase error can be calculated directly from equation (24) only if the phase condition $|\varphi| \leq \pi/2$ is fulfilled. The argument of $S_1 \cdot S_{-1}^*$ is unambiguous in the range of $\langle -\pi, \pi \rangle$; therefore, the field inhomogeneity must be smaller than $(\pm \Delta f_{CS})/2$. When the phase of the argument of $S_1 \cdot S_{-1}^*$ is out of range $\langle -\pi, \pi \rangle$, the total phase overflows $2\pi$ so that the phase is summed or subtracted by multiples of $2\pi$. The phase overflow effect leads to the return of the phase into the range of $\langle -\pi, \pi \rangle$. The problem of phase overflow can be solved via unwrapping. To correct phase unwrapping, is necessary to know where the phase starts to be wrapped. Successful phase unwrapping and the $\mathbf{B}_0$ field inhomogeneity correction have a significant influence on the success of the Dixon water/fat decomposition. For example, Glover and Schneider showed how to perform the phase unwrapping algorithm using trend analysis [103].

An important attribute of a sequence is SNR efficiency (NSA* – number of signal average). In the case of the three-point Dixon method, the maximum NSA* = 3. Thus, SNR efficiency can be calculated for the 3PD as follows [104]:

$$\text{NSA}^* = \frac{2(1 - cos\theta)^2}{1 + 2cos^2\theta}. \quad (25)$$

The progress of the NSA* depending on $\theta$ is shown in Fig. 15. The maximum SNR efficiency occurs when $\theta = 2\pi/3$. The 3PD SNR efficiency with $\theta = \pi$ is equal to 2.667.

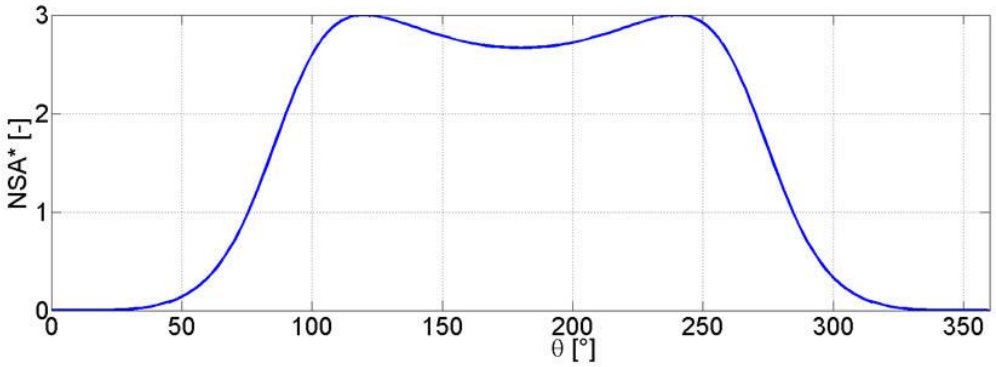


**Fig. 15** The progress of the NSA* depending on the theta angle.

The additional measurement in the 3PD method provides for the calculation of the field inhomogeneity encoded into the phase $\varphi_0$. However, two aspects in the three-point Dixon method can be improved. The first aspect lies in the possibility of determining the $\mathbf{B}_0$ inhomogeneity in voxels containing a mixture of water and fat because the signal is partially cancelled in the two out-of-phase ($\pm\pi$) images used to measure $\mathbf{B}_0$. However, the water/fat decomposition is not jeopardized by the ambiguity. An aspect more important than the previous one is the intra-voxel amplitude losses in the $\pm\pi$ images. The effect of these amplitude losses is normally negligible, but in some applications it may be important [104],

[127]; therefore, the subsequent alternatives to the 3PD were developed directly by Glover again.

#### *4.7.3.2. Extended Three-Point Dixon (E3PD)*

In comparison with the conventional 3PD, the extension of the three-point Dixon method uses a different phase-encoding strategy. The contribution of the diffusion and spectral widening losses is negligible, and thus it can be neglected. Susceptibility dephasing losses are common for water and fat ($A_{1s} = A_{2s} \equiv A_s(\tau)$), but they depend on $\tau$. In the case of the conventional 3PD method, it is not possible to estimate A from the $S_1$ and $S_{-1}$ images, and the asymmetric phase-encoding scheme must be used. Hence, Glover [104] proposed a new asymmetric (0, $\theta$, 2$\theta$) phase encoding strategy. If amplitude losses owing to susceptibility dephasing are considered, the general signal acquired from one voxel can be expressed as

$$S_n = \left(\rho_1 + \rho_2 \cdot e^{in\theta}\right) \cdot A_s^n \cdot e^{i(\varphi_0 + n\varphi)}, \tag{26}$$

where $n$ = 0, 1, 2. If we choose $\theta = \pi$, then the signals from each measurement can be written as follows:

$$S_0 = S(0) = (\rho_1 + \rho_2) \cdot e^{i\varphi_0}, \tag{27}$$

$$S_1 = S(t_a) = (\rho_1 - \rho_2) \cdot A_s \cdot e^{i(\varphi + \varphi_0)}, \tag{28}$$

$$S_2 = S(2t_a) = (\rho_1 + \rho_2) \cdot A_s^2 \cdot e^{i(2\varphi + \varphi_0)}. \tag{29}$$

In the case of a general $\theta$, the solution of the previous equation system is not straightforward. The water and fat components $\rho_1$ and $\rho_2$ are real values because we chose $\theta = \pi$; thus, the loss factor $A_s$ can be calculated from the ratio of the magnitudes $S_2$ and $S_0$. $\varphi_0$ is calculated from $S_0$, similarly to the previous Dixon methods. After the correction of $\varphi_0$, we have

$$S_0' = (\rho_1 + \rho_2), \tag{30}$$

$$S_1' = (\rho_1 - \rho_2) \cdot A_s \cdot e^{i\varphi}, \tag{31}$$

$$S_2' = (\rho_1 + \rho_2) \cdot A_s^2 \cdot e^{i2\varphi}. \tag{32}$$

The phase error $\varphi$ and the loss factor A are calculated as

$$\varphi = 0.5 \cdot \arg\left(S_2' \cdot S_0'^{*}\right) = \frac{\arg(S_2') - \arg(S_0')}{2} = \frac{\phi_{S_2'} - \phi_{S_0'}}{2}, \tag{33}$$

$$A_s^2 = \frac{|S_2'|}{|S_0'|}. \tag{34}$$

When A and $\varphi$ are known, $\rho_1$ and $\rho_2$ can be calculated from equations (30), (31), (32).

The extended 3PD method provides information about the resonance offset in the same manner as the 3PD, and it also provides additional information about the intra-voxel amplitude loss. The SNR performance and imaging time are equivalent to the 3PD method. If

the Lorentzian distribution of spectral distribution in a voxel is assumed, the losses due to susceptibility dephasing can be expressed as

$$\mathrm{A_S} = e^{-\frac{|\tau|}{T_2'}}, \tag{35}$$

where $T_2'$ is the half-width of the spectral line. The new phase-encoding strategy (0, $\theta$, 2$\theta$) used in the EP3D enables us to establish the water ($\rho_1$) and fat ($\rho_2$) components, the $\mathbf{B}_0$ field, the losses $\mathrm{A_S}$ due to susceptibility dephasing, and the $T_2'$.

#### *4.7.3.3. Four-Point Dixon (4PD) Method*

As was mentioned earlier, spectral broadening is one of the three factors which can contribute to the total loss factor A (9). The water spectral line is sharp; thus, we have the loss factor $\mathrm{A_{1W}} = 1$. The fat line has several components close around, and the spectrum is broadened. The fat broadening has a direct effect on the correct water/fat decomposition. The Gaussian shape of the fat spectral line is assumed; therefore, the loss factor $\mathrm{A_{2W}}$ for fat can be calculated as follows:

$$\mathrm{A_{2W}} = \mathrm{e}^{-\frac{(\Delta\omega\cdot\tau)^2}{4}}, \tag{36}$$

where $\Delta\omega$ is the half-width of the fat spectral line [104]. The acquired signal including the fat broadening effect can be expressed generally, using the equation (8) as follows:

$$S_n = \left(\rho_1 + \rho_2 \cdot \mathrm{A_{2W}^n} \cdot \mathrm{e}^{in\theta}\right) \cdot \mathrm{A_s^n} \cdot \mathrm{e}^{i(\varphi_0 + n\varphi)}. \tag{37}$$

From the previous equation (37) there follows an additional degree of freedom; therefore, another additional measurement must be performed. Glover has introduced a phase-encoding strategy with (0, $\theta$, 2$\theta$, and 3$\theta$). The general solution of the previous equation (37) is complicated, but the solution process is simplified for $\theta = \pi$. When $\mathrm{A_s} = \mathrm{A_1}$ and $\mathrm{A_{2W}} \cdot \mathrm{A_s} = \mathrm{A_2}$, then

$$S_n = \left(\rho_1 \cdot \mathrm{A_1} + \rho_2 \cdot \mathrm{A_2} \cdot \mathrm{e}^{in\theta}\right) \cdot \mathrm{e}^{i(\varphi_0 + n\varphi)}. \tag{38}$$

In the case of (0, $\pi$, 2 $\pi$, and 3 $\pi$) phase-encoding, the following system of equations is obtained:

$$S_0 = S(0) = (\rho_1 + \rho_2) \cdot \mathrm{e}^{i\varphi_0}, \tag{39}$$

$$S_1 = S(t_a) = (\rho_1 \cdot \mathrm{A_1} - \rho_2 \cdot \mathrm{A_2}) \cdot \mathrm{e}^{i(\varphi + \varphi_0)}, \tag{40}$$

$$S_2 = S(2t_a) = (\rho_1 \cdot \mathrm{A_1^2} + \rho_2 \cdot \mathrm{A_2^2}) \cdot \mathrm{e}^{i(2\varphi + \varphi_0)}, \tag{41}$$

$$S_3 = S(3t_a) = (\rho_1 \cdot \mathrm{A_1^3} - \rho_2 \cdot \mathrm{A_2^3}) \cdot \mathrm{e}^{i(3\varphi + \varphi_0)}. \tag{42}$$

The $\varphi_0$ and $\varphi$ are calculated similarly to the previous multipoint Dixon methods, and the equations (39), (40), (41), (42) will be simplified to yield

$$S_0'' \equiv S_0' = (\rho_1 + \rho_2), \tag{43}$$

$$S_1'' \equiv S_1' \cdot \mathrm{e}^{-i\varphi} = (\rho_1 \cdot \mathrm{A}_1 - \rho_2 \cdot \mathrm{A}_2), \tag{44}$$

$$S_2'' \equiv S_2' \cdot \mathrm{e}^{-i2\varphi} = (\rho_1 \cdot \mathrm{A}_1^2 + \rho_2 \cdot \mathrm{A}_2^2), \tag{45}$$

$$S_3'' \equiv S_3' \cdot \mathrm{e}^{-i3\varphi} = (\rho_1 \cdot \mathrm{A}_1^3 - \rho_2 \cdot \mathrm{A}_2^3), \tag{46}$$

where

$$S_n'' \equiv S_n' \cdot \mathrm{e}^{-i(n\varphi+\varphi_0)}. \tag{47}$$

The 4PD method provides more accurate water/fat decomposition compared to the E3PD method because additional information related to the losses due to fat broadening is obtained. Otherwise, the 4PD is logically more time-consuming than the E3PD or 3PD methods. Identically to the 3PD method, the SNR efficiency depends on the choice of the $\theta$ angle.

The success of the water and fat separation directly relates to correct phase unwrapping, which can be performed through the use of polynomial fitting [117], region growing [106], or graph cut [113], [128].

## Unwrapping

Generally, phase unwrapping is a well-studied and very difficult problem in mathematics and engineering. Phase unwrapping failure leads to incorrect estimation of water and fat components. Although many different methods have been proposed [129], no general solution has been found to date. The purpose of unwrapping is to establish the true phase $\varphi$ from the wrapped phase $\varphi$, that is

$$\hat{\varphi} = \varphi + 2k\pi, \tag{48}$$

where $k$ is the integer, and the true phase $\varphi$ is within the range $\langle -\pi, \pi \rangle$. Thus, the true phase can be calculated as

$$\varphi = \mathrm{Wrapp}[\hat{\varphi}]. \tag{49}$$

Phase unwrapping is a reasonable operation if we have more than one pixel. In this case, phase wrapping occurs when the phase difference exceeds $2\pi$ between two neighbouring pixels or spatial locations. Phase wrapping then results in phase discontinuities or, in other words, phase jumps. These discontinuities are called “fringe lines” [129], [101]. The basic purpose of phase unwrapping is to identify a phase jump and to restore the true phase from the wrapped one by subtracting or adding the multiple of $2\pi$. A very important condition necessary for recovering the true phase from the wrapped one is as follows:

$$-\pi < \Delta\varphi(x) \leq \pi, \tag{50}$$

where $\Delta\varphi(x) = \varphi(x+1) - \varphi(x)$ represents the true phase difference between two neighbouring pixels. If the above condition (50) has not been satisfied, the unwrapping will be incorrect. In magnetic resonance imaging, there are several sources disrupting the previous condition, for example noise, spatial undersampling of the phase, and artefacts owing to aspects including movement or blood flow. An extreme case exists in background regions

where the signal drops to zero and the phase distribution is random. For these regions, effective information about the true underlying phase (e.g., field homogeneity) cannot be acquired. Although, from the mathematical perspective, any correction procedure can be appropriate, the actual unwrapping in the given regions (pixels) is pointless. It is important to note that phase unwrapping errors in the discussed regions can potentially disturb phase unwrapping in areas where the true phase is incorrect. The success of the phase unwrapping algorithm in these regions depends on the design of the algorithm. The unwrapping methods can be divided into the following three main groups: minimum-norm methods [130], [131]; path-following methods [132], [133]; and pixel-based analytical methods [16], [120], [134], [135], [136]. A short description of these methods can be found within several sources [101]; detailed description of the discussed techniques is beyond the scope of this work.

### 4.7.4. Extended Two-Point Dixon Method (E2PD)

The multipoint Dixon technique provides more information on true water/fat separation. Unfortunately, the discussed methods require longer acquisition time. Yang et al. [117], Akkerman and Mass [116], Skinner and Glower [107], and Coombs et al. [106] showed that phase error due to field inhomogeneity can be obtained only by the 2PD method.

Now let us assume the original 2PD method. The already discussed equations (12) reveal that $\varphi_0$ can be obtained immediately, similarly as in the above-mentioned Dixon methods; thus, the subsequent equations (14), (15) are yielded. If the phase range does not exceed $2\pi$, the argument of $S_1'$ can be calculated directly. The phase error $\varphi$ can be calculated as follows:

$$\varphi = 0.5 \cdot \arg\left\{\left(S_1' \cdot S_0'^{*}\right)^2\right\}. \tag{51}$$

When the argument of $\left(S_1' \cdot S_0'^{*}\right)^2$ exceeds $2\pi$, it must be unwrapped. The square operation in the argument of the previous equation (51) practically means that the water and fat are in-phase ($2\pi$). The success of the E2PD method lies in the field inhomogeneity estimation related to the phase error, as shown in, for example, equation (51). A multitude of phase-correction algorithms for the 3PD have been proposed and applied in the 2PD method; these include region growing [106], solving Poisson's equation [107], or polynomial fitting [117]; all the discussed algorithms can be used for phase unwrapping. However, phase unwrapping for 2PD is more error-prone compared to the 3PD method. In the case of the E2PD, the SNR of the $\mathbf{B}_0$ map is low in the water/fat boundary regions since the signal of an OP image decreases towards zero, and the phase difference is half-size in comparison with the E3PD method. The E3PD method uses two IP images to calculate $\mathbf{B}_0$; therefore, the signal is not decreased in the pixel with the mixture of water and fat. The fat is broadened owing to other fat components, which in turn causes $T_2^*$ decay in the shifted-echo acquisition [104]. Therefore, fat suppression in the E2PD is worse than in the E3PD. [107]

The reliability of processing is frequently related to signal cancellation in voxels containing a mixture of water and fat. It often occurs at the boundaries of water- and fat-dominated regions. Problems can occur in the case of phase unwrapping algorithms that

require an empirical angular threshold as a criterion for phase unwrapping, mainly because of the phase uncertainty and increased phase variation in voxels where water and fat are partially disrupted. Thus, the determination of an optimal angular threshold can be problematic or even impossible. This can be avoided by segmentation of the image or compromising the reliability of phase unwrapping.

In the case of 2PD, the phase vector (phasor) can be obtained from the equations (12) and (13) for pixels containing more water than fat, such that

$$e^{i\varphi} = \frac{S_1 \cdot S_0^*}{|S_1| \cdot S_0}, \tag{52}$$

or for pixels where fat is a dominant component; we then have

$$e^{i\varphi} = -\frac{S_1 \cdot S_0^*}{|S_1| \cdot S_0}. \tag{53}$$

Thus, the phasor will be assigned the *plus* or *minus* sign. The phasor represents a unit vector in the complex plane, and the direction is determined by $\varphi$ but unaffected by a possible phase wrap in $\varphi$. It should be emphasized that the change of the phasor direction is not associated with phase wrapping. Over time, many improvements have been proposed for the elimination of field inhomogeneity in water-fat separation by 2PD methods. Ackerman and Mass [116] showed that the water and fat separation can be successfully secured via the 2PD without direct phase unwrapping. These authors used a region-growing algorithm (R-GA) similar to that applied by Szumowski [133]. A different robust R-GA was proposed by Ma [137], with several improvements made compared to the previously reported algorithms. Another modification of the original 2PD method was reported by Xiang [110]; here, the principle consisted in the measurement of one in-phase image and a different image with a partially opposed phase (POP), where water and fat are not utterly in the opposed phase. In this case, two phasor candidates are sought as in the previous algorithms, analogically to the two phasors with the *plus* and *minus* signs for the symmetrical 2PD. Xiang used the regional iterative extraction (RIPE) algorithm to determine the phasor candidates (resolve the error phasor ambiguity). *The method demonstrated that the opposed-phase constraint could be relaxed, and Eggers et al.* [138] *suggested that also the remaining constraint could be removed, allowing both echo times to be set as short as possible* [108]. In theory, the echo times are flexible, but in practical applications the echo times are limited by the noise performance (NSA) and capacity of resolving the error phasor ambiguity. Berglund et al. [108] showed that 2PD methods without usual constraints on the echo times provide several advantages, such as flexible shortening of the acquisition time or a spatial resolution increase.

### 4.7.5. Single Point Dixon Methods

Several clinical applications require a maximally short total acquisition time. The 2PD technique improves the data acquisition efficiency compared to the 3PD or MPD methods. Generally, MRI data are complex and contain a real and an imaginary part. These parts can be interpreted as real and imaginary channels. If the field inhomogeneity is perfect

and the relative phase difference between water and fat is 90° (water and fat are acquired in quadrature) [139], [140], [141], [142], then the water contributes to the real part (after the FT) and the fat contributes to the imaginary part. In fact, the inhomogeneity and the related phase error always occur; therefore, a real and an imaginary part of MR images always contain a water and fat signal mixture. In general, the obtained signal from one scan corresponds to equation (8) with three unknowns (water, fat, and $\varphi_0 + \varphi$ ), and the error terms $\varphi_0 + \varphi$ cannot be obtained. Initially, two approaches to phase correction were reported. The first technique is to use the data from the reference scan [139], [140], [119], and the second approach consists in using empirical phase modelling [141], [142]. The previous approaches eliminated the influence of inhomogeneity with varying degrees of success.

Xiang [143], [144] introduced a relatively simple and fast phase correction algorithm for the single-point Dixon (SPD) method without the necessity of a reference scan or explicit modelling of the phase errors. The method is based on normalization up to the unity of the magnitude of the original complex image obtained from the SPD quadrature acquisition; consequently, heavy smoothing (low-pass filtering) is applied on the real and imaginary channels. The smoothed (filtered) image has a significant signal reduction in the pixels at the water/fat border regions. Following this fact, the regions along the borders are segmented and classified as water- or fat-dominated areas by examining the phase of the boundary pixels. Therefore, a CBM (coloured-border map) map can be created, where the water border, fat border, and other pixels are represented by three values: 1, – 1, and 0. In the first approach, Xiang [143] implemented a phase angle rotation (78°) to the signal in fat-dominant pixels. A follow-up approach consists in "virtual shimming", in which the local phase rotation mimics a magnetic field adjustment to achieve the best chemical shift spectrum in every region of the image [144]. Under the assumption that all pixels in the image which contain a significant amount signal are water- or fat-dominant, the phase correction of the SPD method (without the reference scan) can be performed using the R-GA [145], [115], [146]. An advantage of the method presented by Ma [115] is that the fully-automated R-GA was used and the data were acquired with a flexible echo time.

## Data Acquisition Strategy and a Summary of Dixon Methods

Dixon methods in several variants are widely used with many pulse sequences, such as the fast spin echo [120], [147], [148], [149], [150], the gradient echo-based sequences (SPGR methods, SSFP and bSSFP methods) [120], [151], [152], [153], or sequences with non-rectilinear k-space sampling, for example spiral [154], [155] or concentric rings trajectory [156]. In the first approach, the success of most Dixon methods lies in the phase correction procedure. Any failure of the phase correction procedure leads to incorrect water/fat separation (water and fat can be swapped in the pixel). Another significant factor affecting the water/fat separation is the data acquisition strategy. The data acquisition strategy relates to a specific phase correction algorithm and to how the data acquisition strategy is implemented into the pulse sequence. In the case of an acquisition strategy with a long scan time, the sequence can be sensitive to motion artefacts. It is important to note that motion artefacts are a challenge for the phase correction procedure. Yet another important factor is a relative phase between water and fat related to echo spacing. A relative water-to-fat phase plays a significant

role in sequences where the maximum time efficiency and optimal image quality are required. The changes of timing in the pulse sequence (e.g., the echo time in the GRE or echo spacing in the FSE) and the related phase change between water and fat can lead to a decrease of the image quality and reduction of the scan time efficiency. It follows therefrom that data acquisition with a small relative phase between water and fat would be ideal, but in reality the success of the phase correction procedure strongly depends on the ability to detect and correct phase changes in the presence of noise and other phase errors. A small water-to-fat phase difference leads to a lower SNR in the calculated water and fat images. The selection of a suitable Dixon method requires us to consider all the factors mentioned above.

From the perspective of the scan time duration, the SPD method obviously provides the shortest scan time but, unfortunately, does not secure sufficient information on water-fat separation; additionally, the assumption of water- or fat-dominated pixels is necessary. Therefore, the SPD method cannot be strictly quantitative for all applications. In the case of the SPD with a reference scan, there is the possibility of image degradation following a patient motion or instability of the MR system. In comparison with the SPD, the 2PD method requires a double scan time in the very least; unlike the SPD, however, the 2PD approach provides a more than sufficient amount of information necessary for water/ fat separation. In addition, the information obtained from 2PD methods is essentially the same as in the case of 3PD methods, excepting pixels where the amount of water and fat is identical. Generally, the 3PD or MPD methods are more time-consuming and more prone to degradation due to a patient motion (human or animals); these techniques nevertheless provide full information [104] related to water/fat separation and the MPD methods can be used to separate two or more spectral components [120].

Many clinical applications require a very short scan time, and there are several ways to reduce its overall length. The presented Dixon methods are very flexible and can be implemented together with other techniques for reducing the total scan time. In the case of multiple receive coils, one of the options is partially parallel imaging (PPI). The scan time reduction is determined by the acceleration factor corresponding to the number of coils through the k-space undersampling [157], [158], [159]. Several combinations of Dixon methods with PPI acceleration have been proposed [160], [161], [162]. Another effective method to reduce the Dixon acquisition time consists in acquiring multiple input images with dual-echo [137], [163], [164], [165] or multi-echo [149], [166], [167] readouts.

A number of scans in Dixon methods increases the SNR in the calculated images (water, fat, or other spectral components) compared to an individually acquired image. The efficiency of Dixon methods is represented by the NSA (number of signal averages). The value of the NSA depends on the method, the acquisition strategy, and data processing. Furthermore, the SNR performance can depend on the relative amount of water and fat in individual pixels [112].

# 5. Efficient $T_2$-Weighted (T2W) Fast Imaging Methods

Together with other contrasts (such as T1W, DWI, or SWI), $T_2$-weighted (T2W) images provide valuable information on many diseases. The conventional fast spin echo (FSE) method is a standard MRI sequence for acquiring T2W images in preclinical or clinical research. The previously presented FSE-based Dixon implementations [147], [120], [148], [168] facilitate effective shortening of the Dixon acquisition time, but the measurement time is still *n*-times longer (for nPD) than in one FSE scan. Therefore, Ma et al. introduced a new method called the fast spin echo triple-echo Dixon (fTED) method. This modification of the FSE sequence significantly reduces the Dixon acquisition time in such a manner that the duration of Dixon acquisition is equal to that of one FSE scan. In this thesis, we propose a novel modification of the FSE method to be used for the Dixon acquisition. The method is called fast triple spin echo Dixon (FTSED), and it significantly reduces the Dixon acquisition time. The technique is described in Chapter 5.3.

The application of the FTSED sequence at a high field is major challenge. As mentioned earlier, the chemical shift increases commonly with the $\mathbf{B}_0$ field, and field inhomogeneity induced by magnetic susceptibility is stronger at high fields. A chemical shift increase leads to a larger shift of position between the water and fat components in an MR image for the same bandwidth (BW) and field-of-view (FOV). In the case of a high field, spin-spin relaxation decreases faster; thus, some parameters, e.g., the echo train length (ETL) in FSE-based methods, are limited. Furthermore, along with the chemical shift increase, the speed of rotation of fat components is also increased; therefore, to achieve π water-fat phase difference, a shorter time shift is necessary.

## 5.3. Fast Triple-Spin Echo Dixon Method (FTSED)

The Fast Triple-Spin Echo Dixon Sequence (FTSED) is derived from the conventional fast spin echo (FSE) method proposed by Hennig et al. [169] and can be classified as a 3PD method. The main goal of the proposed method (FTSED) lies in the acquisition of three independent k-spaces, each for a specific echo shift (Fig. 17), during one instance of FTSED acquisition; thus, the Dixon acquisition time will be equal to the FSE method duration. Fig. 17 shows a FTSED sequence for particular phase encoding steps (0, -π, -2π). Generally, however, the echo shifts can be chosen arbitrarily (within the limits of the sequence), and the Iterative Least-Squares Estimation Method [120] can be used for water and fat calculation (Appendix A). Reeder et al. [111] indicate that symmetrically acquired echoes cause artefacts which degrade image quality; therefore, symmetrical phase encoding strategies were excluded a priori. In addition, the authors found an optimal echo combination where noise performance reaches the achievable maximum and will be independent from the proportion of water and fat. The combination of asymmetrically acquired echoes with the Iterative Least-Squares Estimation is referred to as "iterative decomposition of water and fat with echo asymmetry", IDEAL [111]. In our case, the specific asymmetric phase encoding strategy was chosen:

(0, -π, -2π) or (0, π, 2π). The chosen strategy will ensure the achievement of PD –, $T_2^*$ –, $T_2$ – weighted images (e.g., Fig. 25 (A), (B), (C)).

The principle of the FTSED lies in the insertion of three (or two) time intervals into the echo train (ET); thus, the three images, each with a specific phase shift between water and fat, are obtained during one FTSED acquisition. This manner of acquisition nevertheless comprises one disadvantage, namely the ETL limitation compared to other FSE-based sequences, e.g. the fTED or asymmetric FSE (AFSE). In fact, the ETL is limited only by the $T_2$ relaxation of the measured sample/tissue (Fig. 16).

It is necessary to mention that the ETL in the FTSED method carries the same meaning as in the FSE echo method, yet there is a little difference: the ETL in the FSE sequence means the number of echoes in the echo train and the acceleration factor. In the case of the FTSED sequence, the ETL defines only the number of refocused echoes in the echo train, and the acceleration FTSED-factor is equal to the ETL/3. The method enables us to choose an arbitrary phase-encoding strategy and generally depends only on our choice. To achieve a stronger contrast between a voxel with dominant water and voxels where fat is dominant, the modified IDEAL algorithm can be used (Appendix B).

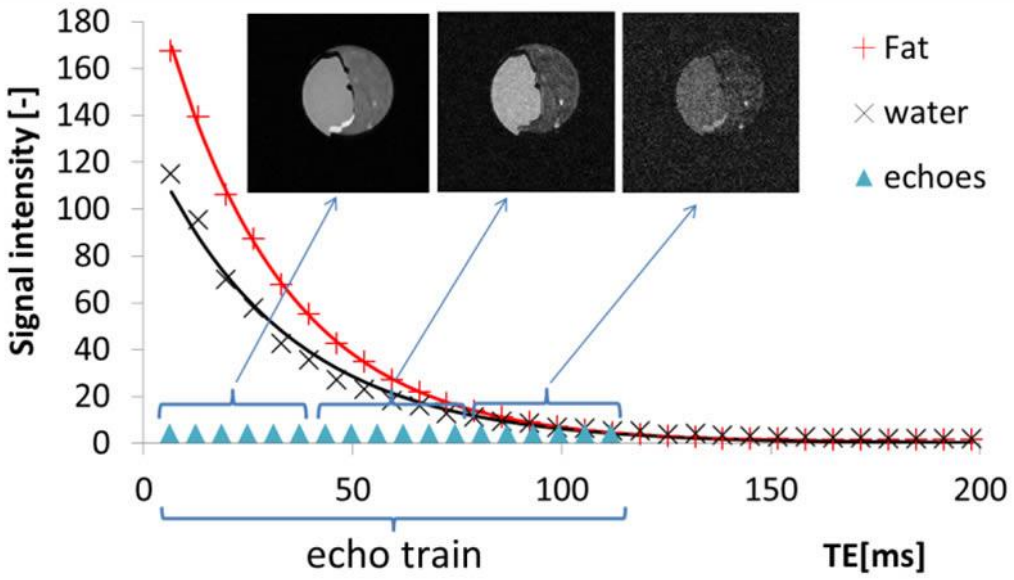


**Fig. 16** The course of water and fat $T_2$ relaxation in the phantom (water and fat/lard) during the FTSED sequence.

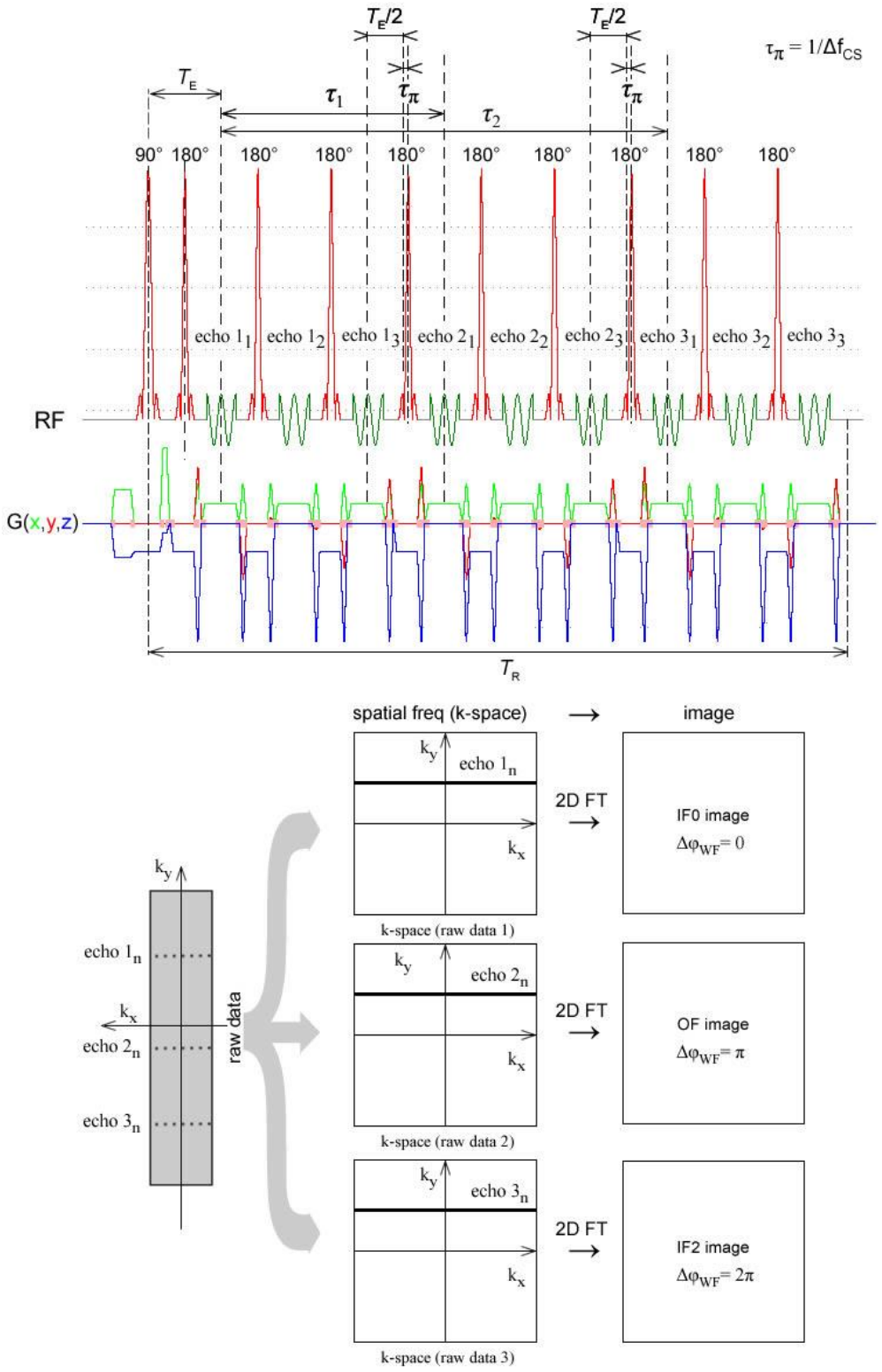


**Fig. 17** The time diagram of the Fast Triple Spin Echo pulse sequence for a particular phase encoding scheme, or 0, π, 2π, and the principle of data acquisition; ETL = 9, FTSED-factor = 3. Three images are obtained during a single acquisition: an in-phase image (IF0), an opposite-Phase image (OP), and an in-phase image (IF2) again, but with the phase difference between water and fat of 2π. n = FTSED-factor = 3.

# 6. Results

The proposed method was successfully implemented in an 9.4 T MRI system (Bruker, BioSpec 94/30). Two phantoms were created for the evaluation of the FTSED method, the first being a set of plastic tubes (twelve) containing a water-fat emulsion (mayonnaise mixed with water), each with various water/fat ratios. The second phantom consisted in a compound of lard and water placed into a glass tube. Consequently, the method was applied in rats. All animal measurements were performed with real-time breath-hold triggering (SAII, Model 1030), and each measurement followed in the pause (or interval) after exhalation. All calculations were performed in the Matlab program.

The first phantom (Fig. 19) with various concentrations of fat in water was created upon the necessity to verify correct determination of the fat fraction (FF).The fat signal fraction can be calculated as follows [170]:

$$FF = \frac{|F|}{|F| + |W|}, \tag{54}$$

While an "arbitrary" intensity scale is provided only by water and fat images, FF images secure quantitative mapping of the fat signal in each voxel [171].

| Sample [-] | 1 | 2 | 3 | 4 | 5 | 6 | 7 | 8 | 9 | 10 | 11 | 12 |
|---|---|---|---|---|---|---|---|---|---|---|---|---|
| Sunflower oil in the whole volume [%] | 0 | 8.84 | 17.7 | 26.5 | 35.3 | 44.2 | 53.0 | 61.9 | 71.0 | 79.5 | 88.4 | 100 |
| Mayonnaise [ml] | 0 | 0.5 | 1 | 1.5 | 2 | 2.5 | 3 | 3.5 | 4 | 4.5 | 5 | 0 |
| Water [ml] | 5 | 4.5 | 4 | 3.5 | 3 | 2.5 | 2 | 1.5 | 1 | 0.5 | 0 | 0 |
| Total volume[ml] | 5 | 5 | 5 | 5 | 5 | 5 | 5 | 5 | 5 | 5 | 5 | 5 |

**Tab. 3** The composition of samples in a phantom with various concentrations of oil.

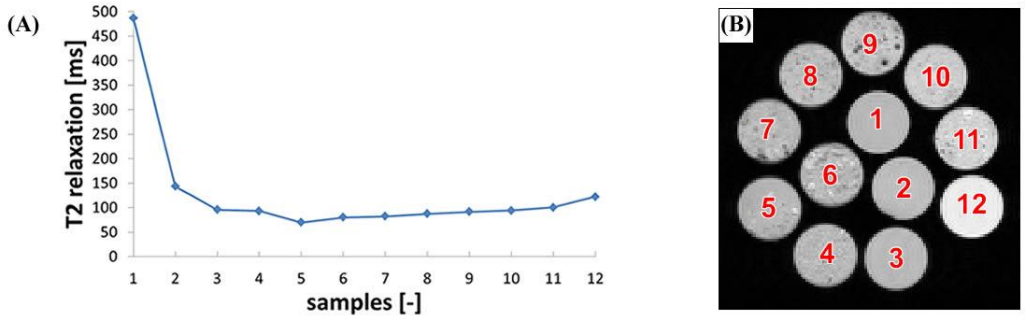


**Fig. 18** The calculated transversal relaxations $T_2$ of samples in the phantom, (A). The numerical designation of samples in the phantom, (B).

The spiral displacement of the tubes in the phantom can be seen in Fig. 18B. Each sample exhibits its own $T_2$ relaxation (Fig. 18A). The phantom composition is shown in Tab. **3**, and the spectrum of the whole phantom is presented in Fig. 22(A). To improve the stability

of the emulsion, the water was mixed with gelatine before being blended with mayonnaise. The mayonnaise was created only from chicken egg and sunflower oil. The mixing of water and oil is a problematic task if performed without an emulsifier. An emulsifier is a substance which reduces the surface tension at the interface between two immiscible liquids, thus enabling homogeneous mixing of the emulsion of the two liquids. In our case, the lecithin in a chicken egg was utilized as a natural emulsifier.

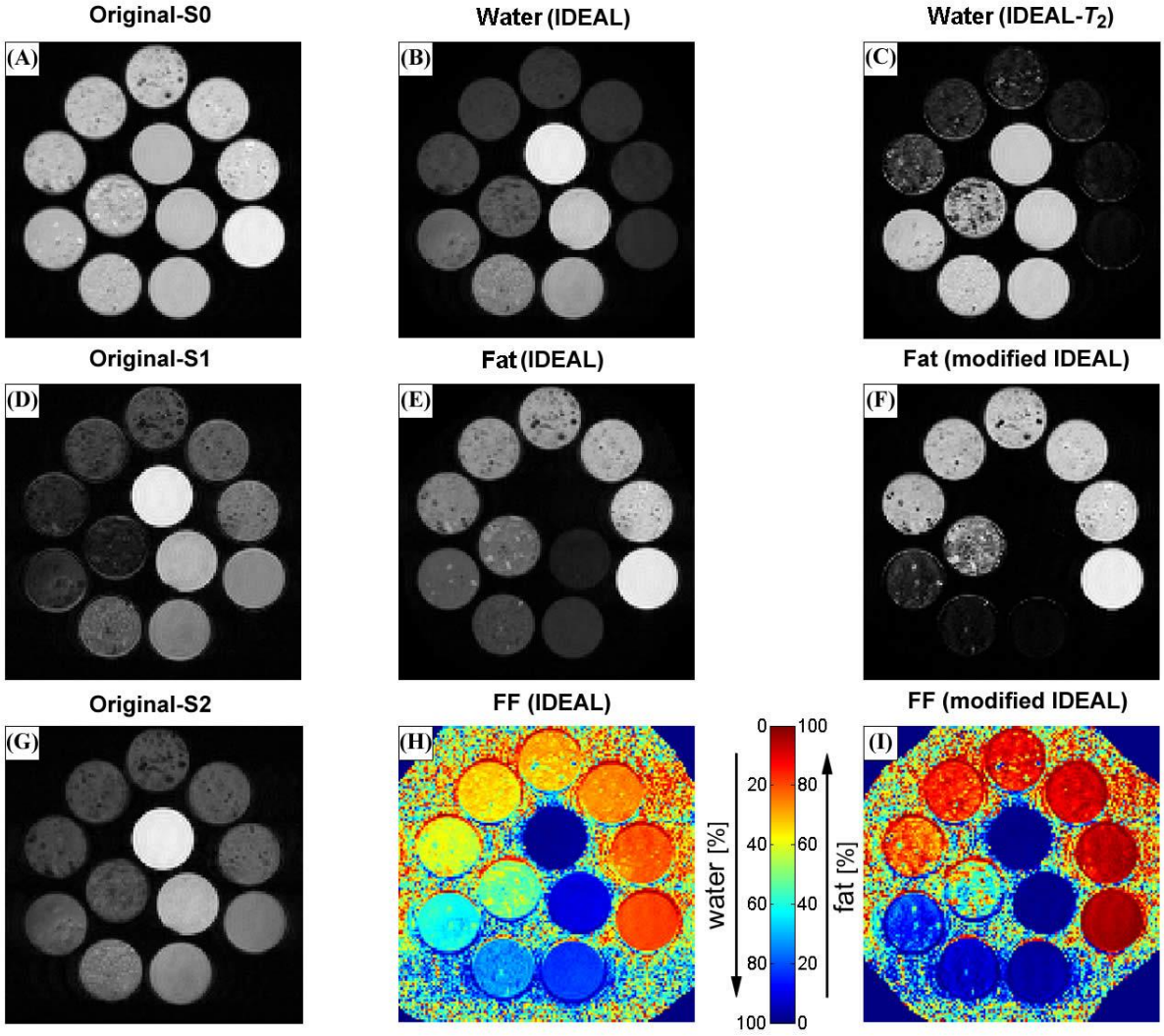


**Fig. 19** The phantom with various ratios of water and fat. (A), (D, (G) are the original images used for the calculation of water and fat images through the use of the IDEAL (B), (E) and the modified IDEAL (C), F) algorithms. The fat fraction calculated for the IDEAL, (H) and the modified IDEAL, (I). The sequence parameters: ETL = 12, (FTSED - factor = 4), BW = 150 kHz, $T_R$ = 3000 ms, $T_E$ = 4.774 ms, ETE($S_0$) = 9.548 ms, ETE($S_1$) = 28.955 ms, ETE($S_2$) = 48.362 ms, matrix = 128 x 128, FOV = 60 x 60 mm; total scan time = 1 m 36 s.

The graph in Fig. 20 shows the values of FF calculated through the use of the IDEAL and the modified IDEAL algorithms for various concentrations of fat. The ROIs were selected over each sample. The red line indicates the theoretical concentration of fat in the emulsion. However, not all samples in the phantom were homogeneous, and therefore the calculated FF maps vary from the theoretical concentration, especially for samples 5 – 7 and 9 – 10. In addition, the emerging small air bubbles exert an undesirable effect on the calculated FF from

the ROIs. The dashed lines with filled circles show the FF calculated via the IDEAL algorithm. The contrast between the voxels with dominant water or fat can be improved (Appendix B), but the resulted FF image is not correct. The solid black lines (Fig. 20) with triangles show that the signal is suppressed in voxels with dominant water and boosted in the fat-dominated voxels. The result is a higher contrast between water and fat. The same findings can be mentioned for water images. The difference between the calculated FF achieved via the FTSED-IDEAL and the theoretical FF (the red solid line) is shown in Fig. 21. In the samples 9 – 12, we evaluated the FF (the blue solid line) acquired from chemical shift imaging (CSI). The FF values were calculated for the same ROIs as in the case of FTSED.

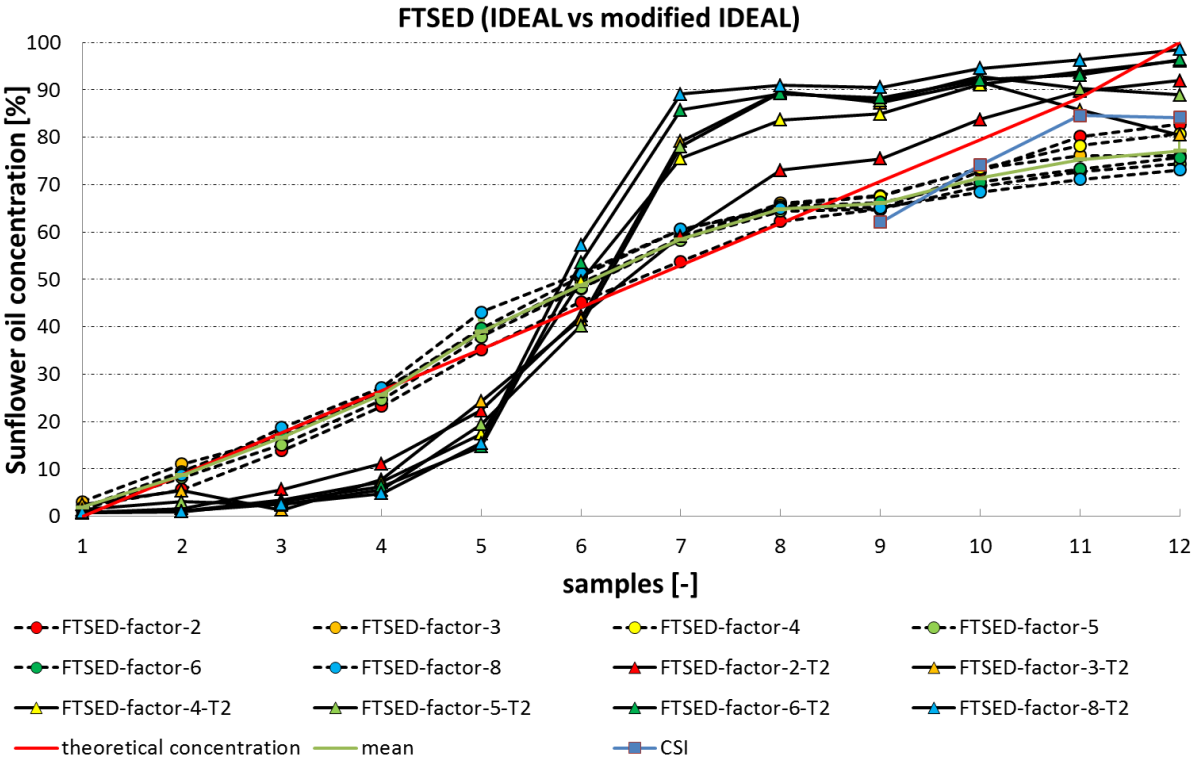


**Fig. 20** The theoretical concentration of fat in the emulsion (solid red line) compared to the measured data. The fat fraction was calculated via the IDEAL (filled circles with dashed lines) and the modified IDEAL (filled triangles with solid lines) algorithms.

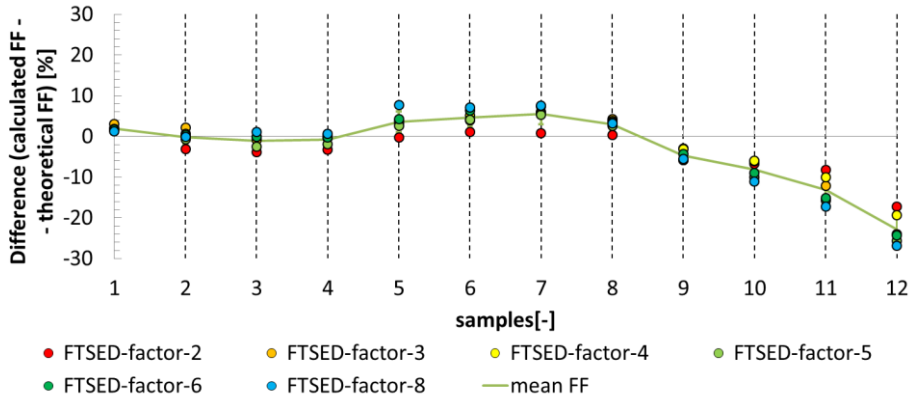


**Fig. 21** The graph showing the level of agreement between the theoretical and the calculated FF (IDEAL).

Fig. 23 – Fig. 26 show the original images (A), (B) and (C) of the second phantom and a rat acquired by the FTSED method; (D), **(**E) and (F) are the corresponding phase images. The images were used for the calculation of water and fat images through the use of the IDEAL (H and I) and the modified IDEAL (Appendix B) ((K) and (L)) algorithms. From the calculated water and fat images, images were recombined for the IDEAL (G) and the modified IDEAL (J). The images (A), (B) and (C), for the selected phase encoding strategy (0, π, 2π), represent PD –, $T_2^*$– and $T_2$ – weighted images.

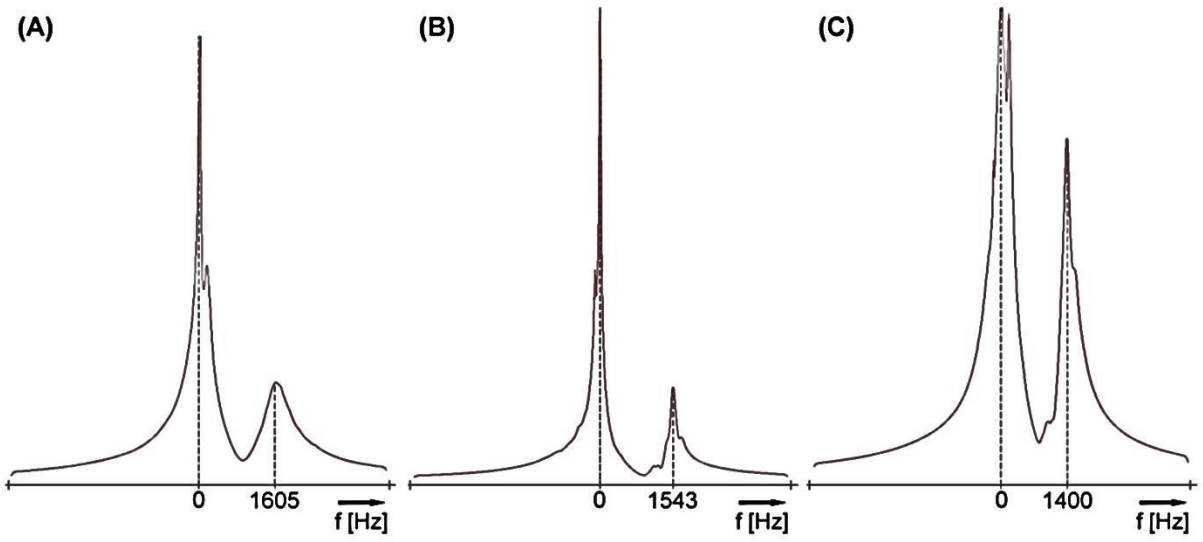


**Fig. 22** The spectra of the measured phantoms (A – water-oil emulsion; B – lard and water) and a rat (C) acquired at 9.4 T. BW = 8kHz, 2048 points.

Fig. 23 and Fig. 24 show axial slices of the measured phantom compound from the water ($T_1$ = 56.5 ms, $T_2$ = 29.1 ms) and fat-lard ($T_1$ = 508.3 ms, $T_2$ = 33.4 ms) placed into the applied glass tube. The chemical shift between water and fat is 1543Hz (Fig. 22(B)). The effects of a relatively long ETL and a "short" $T_2$ lead to errors in the reconstructed water and fat images (Fig. 24 (J), (K), (L). The errors in reconstruction occur due to a lower SNR in the images used for the reconstruction. A lower frequency bandwidth (BW) leads to a higher SNR, but, on the other hand, a low BW yields a bigger shift between water and fat in the image. The effect of a low BW at a high field can be seen in Fig. 24; the water-fat shift is 1.2344 mm in the reading direction. This regrettable effect can be partially eliminated by the exchange of the BW for the same FOV. The position shift between water and fat in the image for a higher BW is shown in Fig. 23. In this case, the shift is only 0.3086 mm. Generally, the shift between water and fat Δx in the image can be expressed as

$$\Delta x = \frac{FOV}{BW} * \Delta f_{CS} \tag{55}$$

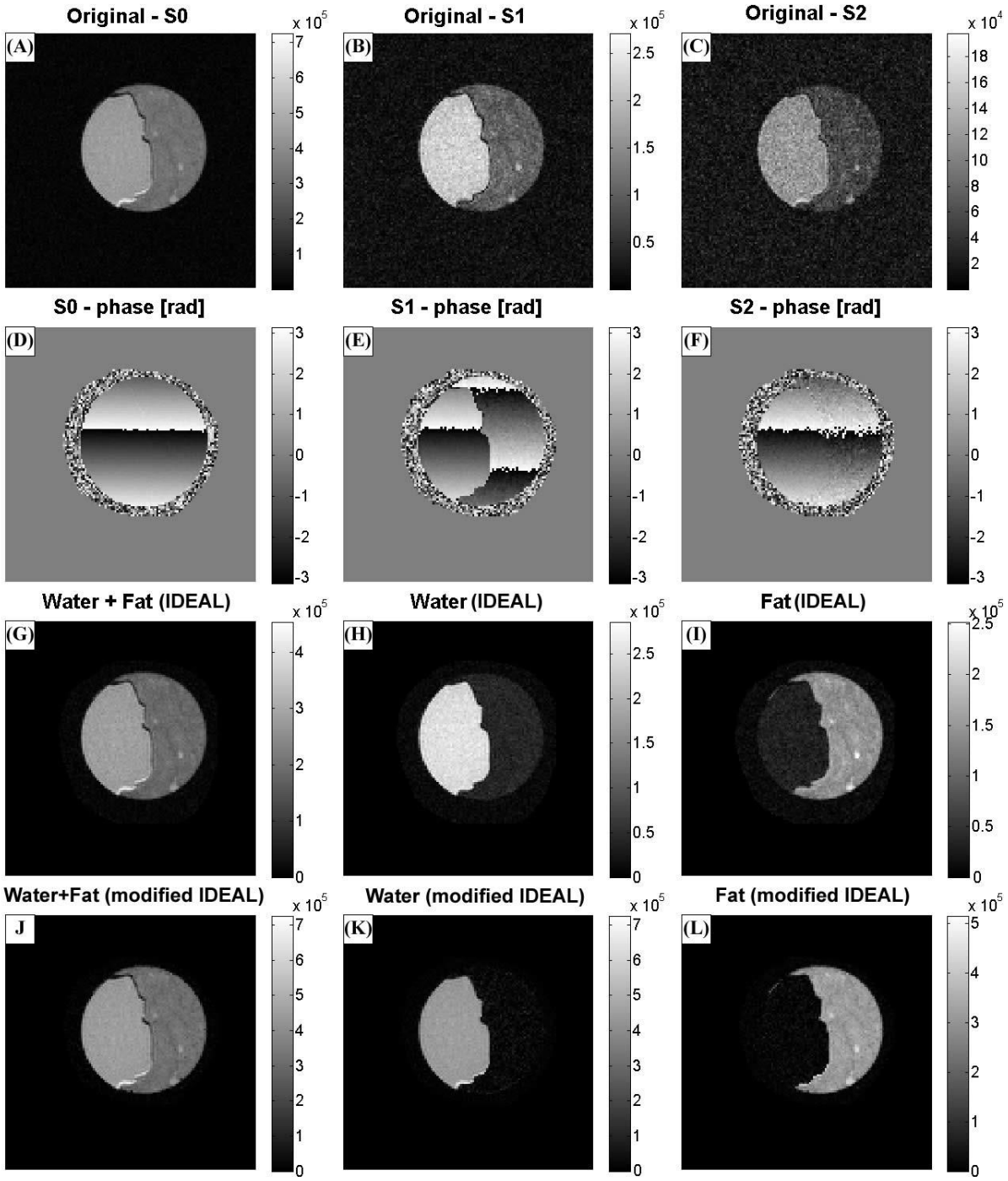


**Fig. 23** A comparison of the IDEAL and the modified IDEAL algorithms for water and fat separation. Axial images of the phantom (water and fat/lard in a glass tube) were acquired using the FTSED sequence (0, $\pi$, $2\pi$). The images (A) – **(**C) show the magnitudes (intensities), and (D) – **(**F) are the corresponding phase images. The calculated water and fat images (H), (I) utilizing the IDEAL algorithm, and the recombined image (G). The images (K) and (L) represent the calculated water and fat images using the modified IDEAL, and the following image **(**J**)** is an image recombined from the previously mentioned ones. Sequence parameters: ETL = 9, (FTSED - factor = 3), BW = 200 kHz, $T_R$ = 2000 ms, $T_E$ = 6.206 ms, ETE($S_0$) = 12.412 ms, ETE($S_1$) = 31.387 ms, ETE($S_2$) = 50.362 ms, matrix = 128 x 128, FOV = 40 x 40 mm; total scan time = 1 m 24 s.

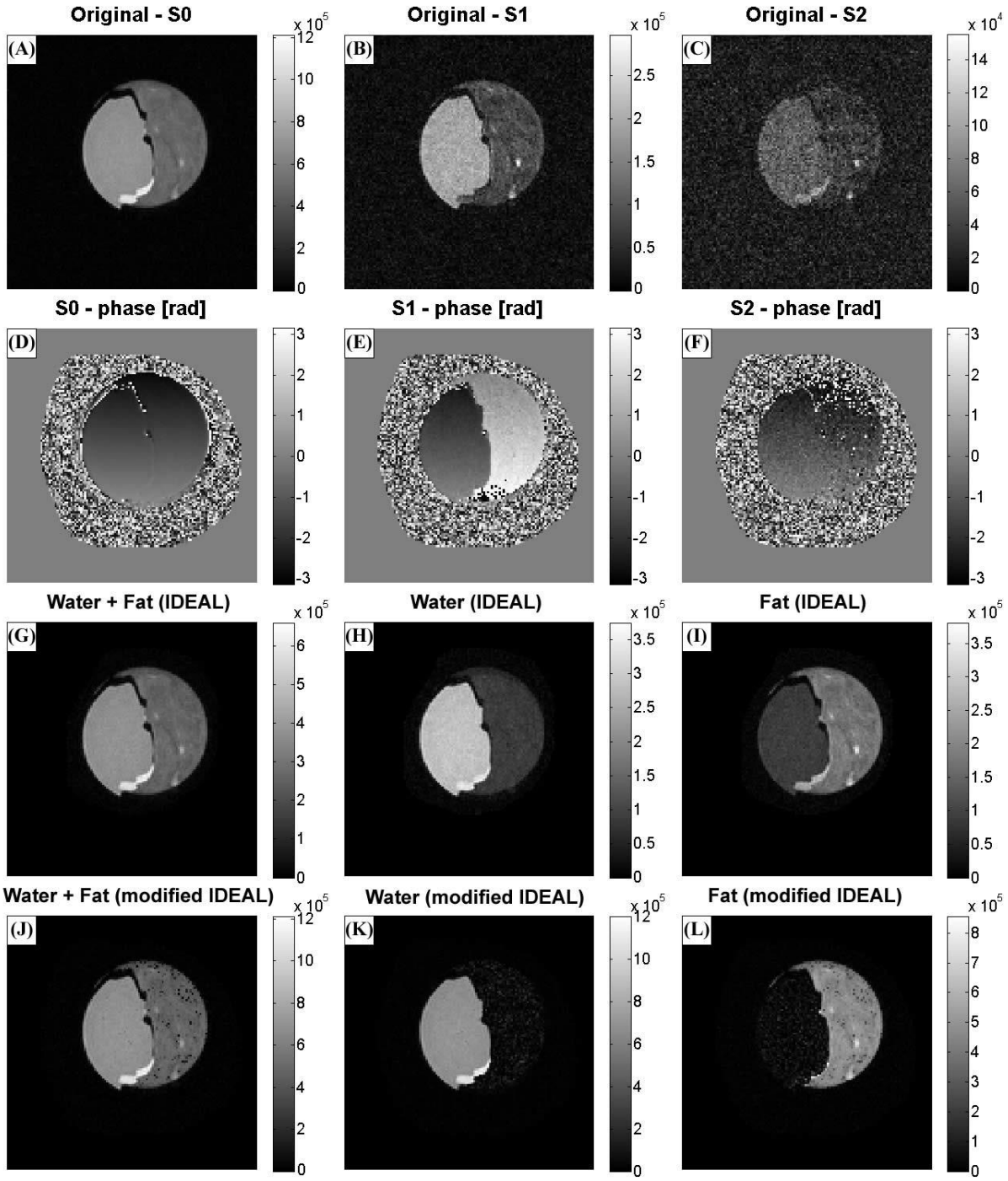


**Fig. 24** A comparison of the IDEAL and the modified IDEAL algorithms for water and fat separation. Axial images of the phantom (water and fat/lard in a glass tube) were acquired using the FTSED sequence (0, $\pi$, $2\pi$). The images (A) – (C) show the magnitudes (intensities), and (D) – (F) are the corresponding phase images. The calculated water and fat images (H), (I) utilizing the IDEAL algorithm, and the recombined image (G). The images (K), (L) represent the calculated water and fat images using the modified IDEAL, and the following image (J) is an image recombined from the previously mentioned ones. The sequence parameters: ETL = 18, (FTSED - factor = 6), BW = 50 kHz, $T_R$ = 2000 ms, $T_E$ = 6.206 ms, ETE($S_0$) = 18.618 ms, ETE($S_1$) = 56.211 ms, ETE($S_2$) = 93.804 ms, matrix = 128 x 128, FOV = 40 x 40 mm; total scan time = 42 s.

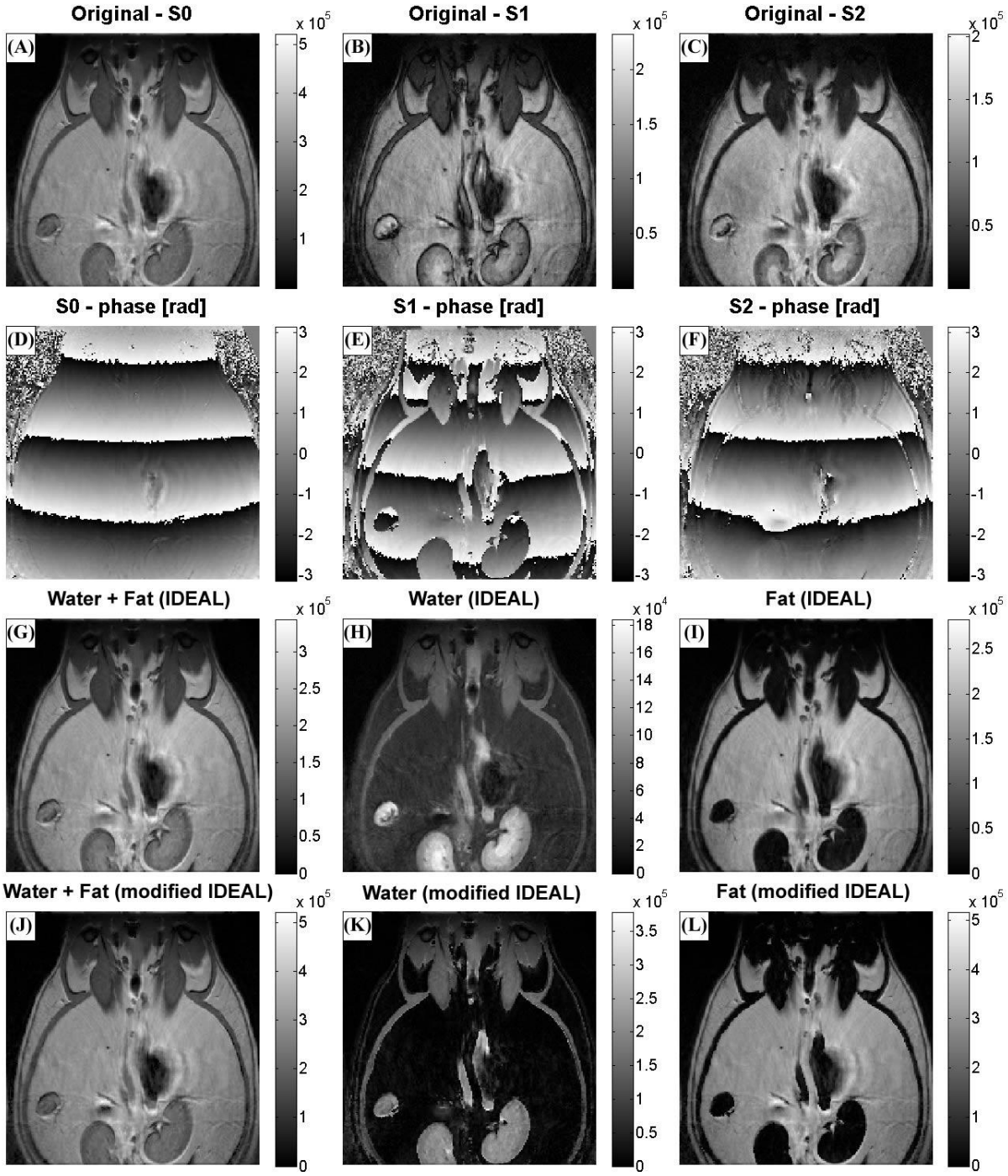


**Fig. 25** A comparison of the IDEAL and the modified IDEAL algorithms for water and fat separation in rats. The coronal images of a rat (abdomen and pelvic region) were acquired using the FTSED sequence (0, $\pi$, $2\pi$). The images (A**)** – **(**C**)** show the magnitudes (intensities), and (D) – **(**F**)** are the corresponding phase images. The calculated water and fat images (H), (I) utilizing the IDEAL, and the image recombined from the previously mentioned ones (G). The images (K) and (L) represent the calculated water and fat images using the modified IDEAL, and the following image **(**J**)** is a recombined image. Sequence parameters: ETL = 12, (FTSED - factor = 4), BW = 150 kHz, $T_R$ = 3000 ms, $T_E$ = 4.774 ms, ETE($S_0$) = 9.548 ms, ETE($S_1$) = 29.001 ms, ETE($S_2$) = 48.454 ms, matrix = 192 x 192, FOV = 70 x 70 mm; total scan time = 2 m 24 s.

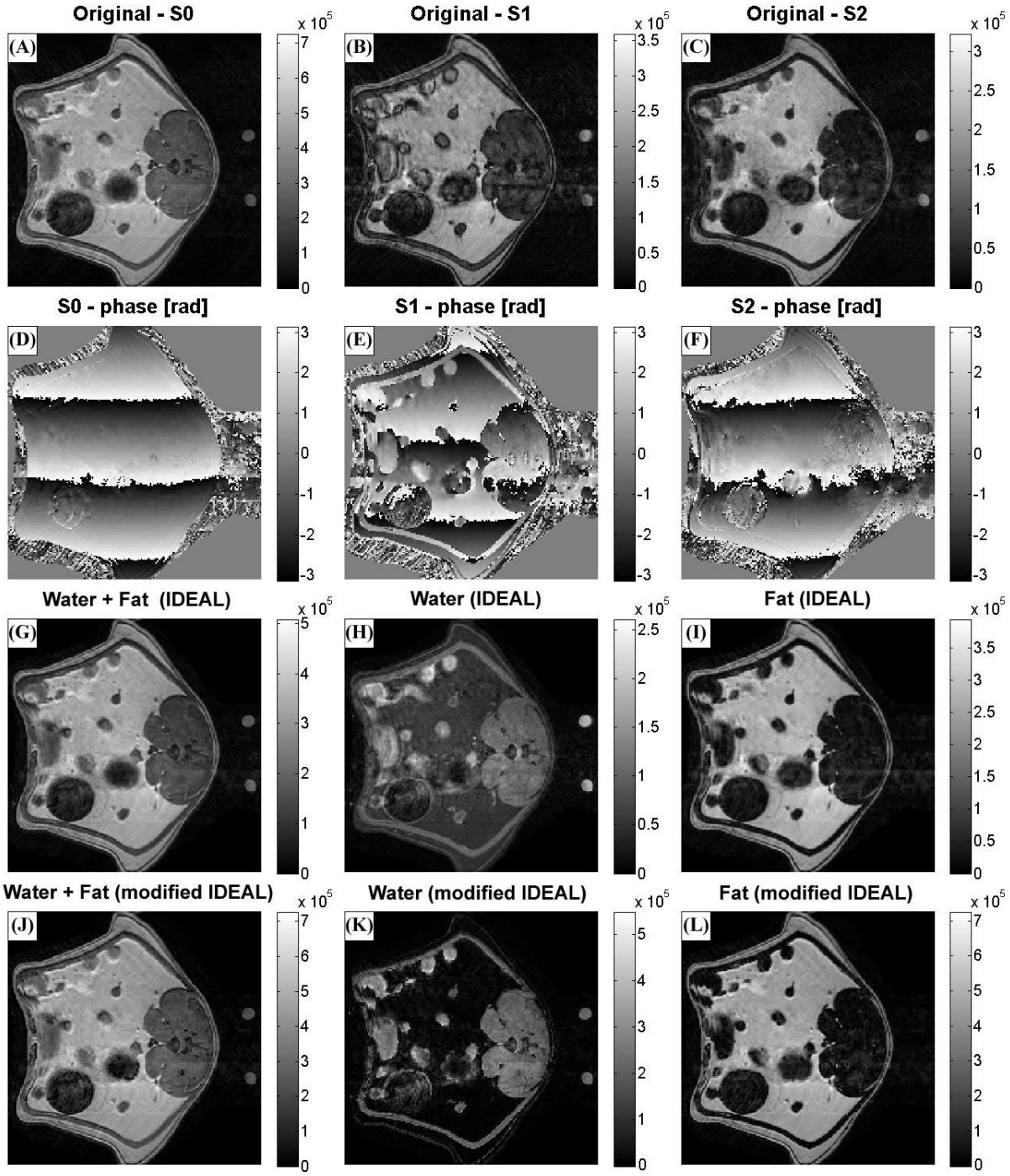


**Fig. 26** A comparison of IDEAL and the modified IDEAL algorithms for water and fat separation in rats. The transversal images of a rat abdomen were acquired using the FTSED sequence (0, π, 2π). The images (A**)** – **(**C**)** show the magnitudes (intensities,) and (D**)** – **(**F**)** are the corresponding phase images. The calculated water and fat images (H**)**, (I) utilizing the IDEAL, and the image recombined from the previously mentioned ones (G). The images (K) and (L) represent the calculated water and fat images using the modified IDEAL, and the following image **(**J**)** is a recombined image. The sequence parameters: ETL = 12, (FTSED – factor = 4), BW = 150 kHz, $T_R$ = 3000 ms, $T_E$ = 4.774 ms, ETE($S_0$) = 9.548 ms, ETE($S_1$) = 29.001 ms, ETE($S_2$) = 48.454 ms, matrix = 192 x 192, FOV = 70 x 70 mm; total scan time = 2 m 24 s.

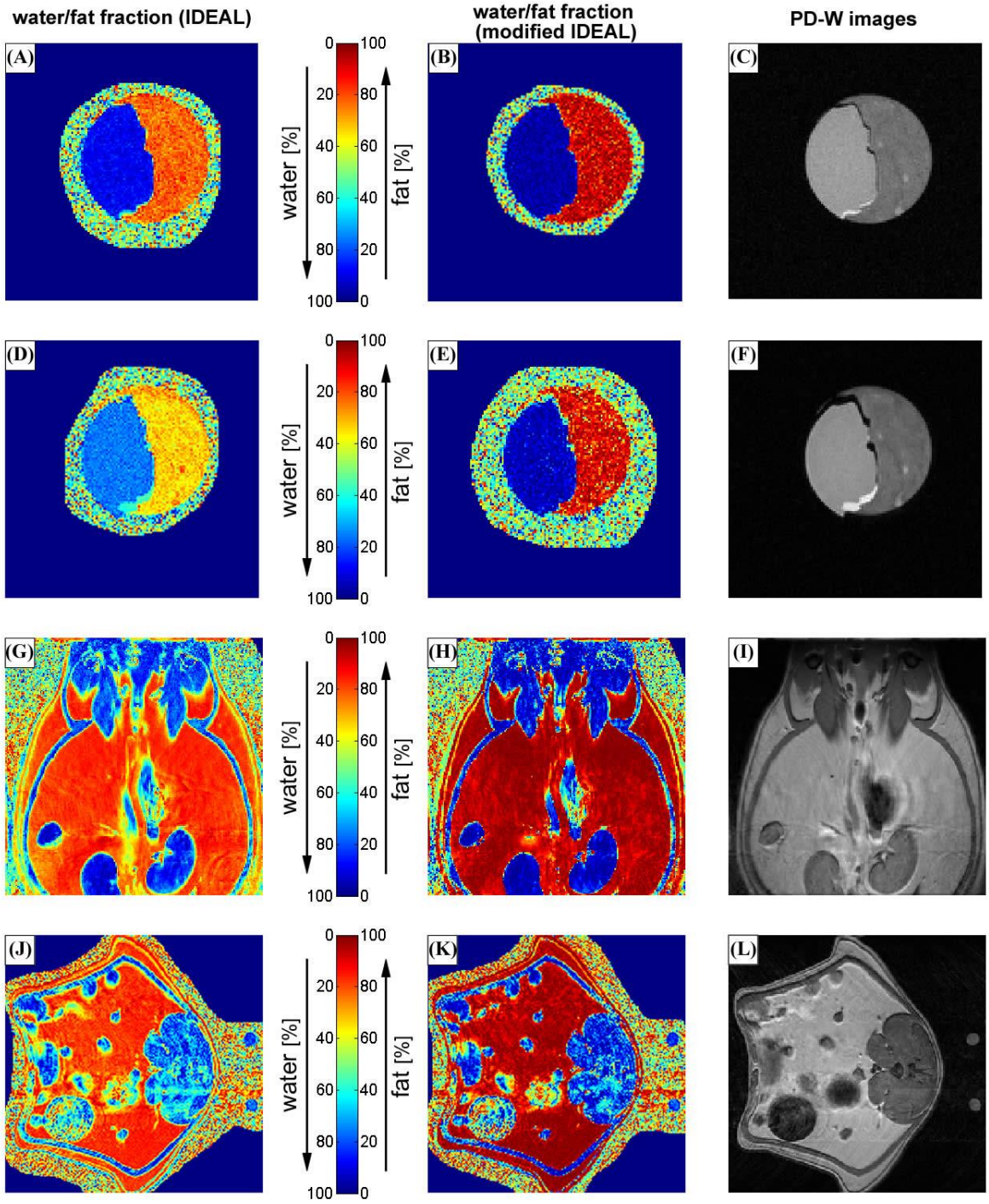


**Fig. 27** The calculated water/fat fraction images for the phantom and the rat abdomen/pelvic region. The water/fat images calculated from the images achieved from the IDEAL, (A), (D), (G), (J), and the modified IDEAL (B), (E), (H), (K) algorithm.

After the verification of the FTSED method in both phantoms, the method was applied in a rat. Fig. 25 shows the coronal slice of a rat abdomen with the pelvic region. Although the measurement was triggered, the images are slightly affected by motion artefacts because the respiration rate was not absolutely stable during the entire measurement. Fig. 26 shows transversal slices through the rat abdomen, where the motion artefacts are stronger. The artefacts are mainly visible in the phase images (D) - (F). The artefacts arise owing to the peristaltic movement of the gastrointestinal tract (intestines and stomach); thus, the abdominal

fat around the gastrointestinal tract is affected by motion too. It can be clearly seen in the water and fat images (H**)**, (I**)**, (K**)**, (L) that the artefacts are primarily due to the fat or water.

Fig. 27 shows the calculated FF and WF for the phantom and the rat abdomen/pelvic region. The spurious effect of the motion artefacts can be seen mainly in the axial slice of rat abdomen (J), (K), and a minor effect of motion artefacts can be observed in the coronal slice of the rat abdomen/pelvic region (H), (I). A strong motion artefact leads to errors in the determination of the correct fat/water fraction. The calculated water/fat fraction (B), (E**)**, (H), (K) images, from the water and fat images achieved by the modified IDEAL algorithm, show different results compared to the original IDEAL algorithm (A**)**, (D**)**, (G**)**, (J) – true value of the FF.

| Phantom – lard and water (ETL = 9, FTSED-factor = 3, BW = 200 kHz) | | | | | | |
|---|---|---|---|---|---|---|
| **I.** | $S_0$ | | $S_1$ | | $S_2$ | |
| | water | fat-lard | water | fat-lard | water | fat-lard |
| ETE [ms] | 12.412 | | 31.387 | | 50.362 | |
| SNR [-] | 44.102 | 31.628 | 22.609 | 10.740 | 12.011 | 5.755 |
| Phantom – lard and water (ETL = 18, FTSED-factor = 6, BW = 50 kHz) | | | | | | |
| **II.** | $S_0$ | | $S_1$ | | $S_2$ | |
| | water | fat-lard | water | fat-lard | water | fat-lard |
| ETE [ms] | 18.618 | | 56.211 | | 93.804 | |
| SNR [-] | 69.095 | 48.229 | 19.526 | 8.801 | 5.814 | 3.673 |

| Rat (coronal slice abdomen/pelvis region) – lard and water (ETL=12, FTSED-factor = 4, BW = 150 kHz) | | | | | | | | | |
|---|---|---|---|---|---|---|---|---|---|
| **III.** | $S_0$ | | | $S_1$ | | | $S_2$ | | |
| | water kidney Roi1* | water muscle Roi2* | fat abdominal Roi3* | water kidney Roi1* | water muscle Roi2* | fat abdominal Roi3* | water kidney Roi1* | water muscle Roi2* | fat abdominal Roi3* |
| ETE [ms] | 9.548 | | | 29.001 | | | 48.454 | | |
| SNR [-] | 75.548 | 51.556 | 109.005 | 44.993 | 21.647 | 56.323 | 40.626 | 10.574 | 48.547 |

| Rat (axial slice of abdomen) – lard and water (ETL = 12, FTSED-factor = 4, BW = 150 kHz) | | | | | | |
|---|---|---|---|---|---|---|
| **IV.** | $S_0$ | | $S_1$ | | $S_2$ | |
| | water muscle (Roi1**) | fat abdominal (Roi2**) | water muscle (Roi1**) | fat abdominal (Roi2**) | water muscle (Roi1**) | fat abdominal (Roi2**) |
| ETE [ms] | 9.548 | | 29.001 | | 48.454 | |
| SNR [-] | 24.022 | 46.746 | 10.404 | 32.866 | 7.774 | 36.390 |

**Tab. 4** Table of the SNR for the original images used for the calculation of water and fat images.

Tab. 4 shows the SNR in the defined ROIs (Fig. 28) for the original MR images achieved with the FTSED method in the phantom (C) and the rat (A**)**, (B). In the phantom, the intensity of water is higher compared to the fat due to a very short $T_1$ relaxation. The undesirable effect of motion artefacts occurred in the SNR evaluation of the axial rat abdomen (Tab. 4, **IV.**, $S_2$ - Roi2**). The acquired images were used for the calculation of water/fat images through the use of the IDEAL and the modified IDEAL algorithm (**Tab. 5**).

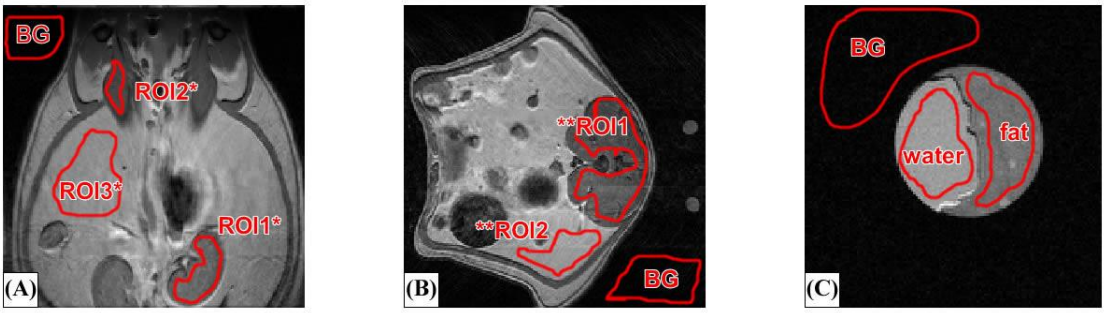


**Fig. 28** The selected regions of interest (ROIs) in the coronal slice of a rat abdomen and pelvic region (A), axial slice of the rat abdomen (B), phantom (C).

The same ROIs (Fig. 28) were applied to the calculated water and fat images of the phantom and the rat, and the SNR in these ROIs were evaluated.

| Phantom – lard and water (ETL=9, FTSED-factor = 3, BW=200kHz) | | | | | | | | |
|---|---|---|---|---|---|---|---|---|
| **I.** | IDEAL | | | | modified IDEAL | | | |
| | W - image | | F - image | | W - image | | F - image | |
| | water | fat-lard | water | fat-lard | water | fat-lard | water | fat-lard |
| SNR [-] | 41.988 | 7.176 | 5.224 | 23.915 | 65.485 | 4.485 | 2.558 | 45.439 |

| Phantom – lard and water (ETL=18, FTSED-factor = 6, BW=50kHz) | | | | | | | | |
|---|---|---|---|---|---|---|---|---|
| **II.** | IDEAL | | | | modified IDEAL | | | |
| | W - image | | F - image | | W - image | | F - image | |
| | water | fat-lard | water | fat-lard | water | fat-lard | water | fat-lard |
| SNR [-] | 46.357 | 14.072 | 14.705 | 27.877 | 98.920 | 10.090 | 6.239 | 65.097 |

| Rat (coronal slice) – lard and water (ETL=12, FTSED-factor = 4, BW=150kHz) | | | | | | | | | | | | |
|---|---|---|---|---|---|---|---|---|---|---|---|---|
| **III.** | IDEAL | | | | | | modified IDEAL | | | | | |
| | W - image | | | F - image | | | W - image | | | F - image | | |
| | Roi1* | Roi2* | Roi3* | Roi1* | Roi2* | Roi3* | Roi1* | Roi2* | Roi3* | Roi1* | Roi2* | Roi3* |
| SNR [-] | 82.92 | 43.72 | 22.98 | 16.06 | 11.48 | 113.26 | 101.11 | 69.53 | 5.95 | 9.09 | 9.31 | 160.08 |

| Phantom – lard and water (ETL=18, FTSED-factor = 6, BW=50kHz) | | | | | | | | |
|---|---|---|---|---|---|---|---|---|
| **IV.** | IDEAL | | | | modified IDEAL | | | |
| | W - image | | F - image | | W - image | | F - image | |
| | Roi1** | Roi2** | Ro1** | Roi2** | Ro1** | Roi2** | Ro1** | Roi2** |
| SNR [-] | 32.796 | 16.694 | 6.542 | 44.078 | 50.878 | 2.308 | 6.606 | 50.214 |

**Tab. 5** The SNRs of the calculated water and fat images from the original images acquired by the FTSED method.* Roi1 – kidney, Roi2 – muscles, Roi3 – abdominal fat; ** Roi1 – muscles, Roi2 – abdominal fat; the selected ROIs can be seen in Fig. 28.

# 7. Discussion

The novel 3PD fast triple spin echo Dixon method (FTSED) is introduced. The proposed technique, derived from the original fast spin echo (FSE) with echo asymmetry, was successfully implemented in an 9.4T MRI system. The measurement at a high field is accompanied by specific problems, which include the consequences of the magnetic susceptibility inhomogeneity: considerable local static field inhomogeneity may lead (in some voxels) to significant resonance line broadening, which then may complicate the separation of the water and fat components. The $T_2$ transversal relaxation shortening at a high field constrains the proposed method. The 3PD method assumes a relatively simple signal model where water and fat have a single resonance frequency, in spite of the fact that fat exhibits several spectral peaks.

The main goal of the FTSED method lies in the acquisition of 3 raw data sets (each with a specific water-fat phase shift) during one scan and in the provision of images with a high SNR. In comparison with the 3PD realized via the FSE with echo asymmetry, sometimes denoted as the AFSE, the total scan time of the FTSED is 3 times shorter. The FTSED method is directly a 3PD method. In addition, the selected phase-encoding scheme (0, $\pi$ and $2\pi$) provides three different image contrasts (PD, $T_2$*, and $T_2$-weighted images), as shown in Figs. 25(A), (B), (C). The time efficiency is directly comparable to that found in another modification of the FSE method: the fast spin-echo triple-echo Dixon (fTED) technique [149]. From the perspective of image processing, the fTED is a 2PD method.

At high fields, the chemical shift between water and fat is increased, and to minimize chemical shift artefacts, strong gradients and a large acquisition bandwidth must be used, in which the set of possible consequences includes non-negligible eddy currents or a reduced SNR. The choice of a low acquisition BW leads to non-negligible chemical shift artefacts in the image. The effect of a low BW is shown in a phantom (Fig. 24). In this case, the gradients of ~29mT/m were insufficient because the chemical shift displacement is 1.23 mm, with the pixel size of 0.31 mm, and it represents a 4-pixel displacement. As can be seen in Fig. 23, the higher acquisition BW reduced the chemical shift displacement. In this case, the gradients of ~117mT/m were sufficient to limit the chemical shift displacement to ~0.31 mm, and this shift represents only a 1-pixel displacement. On the other hand, the SNR reduction in the image is apparent. A high field causes shortening of the $T_2$ relaxation time; thus, the combination of a very long echo train and a short $T_2$ relaxation (Fig. 16 and Fig. 24) leads to errors in the calculated water and fat images, and the computed FF maps will be wrong (Fig. 27(D)).

A phantom with various fat concentrations was created for the verification of the FTSED method. Unfortunately, the concentrations determined from the FTSED – IDEAL differ from the expected values (Fig. 20, red solid line) for several reasons, including the inhomogeneity of the water-fat emulsion, the simplified signal model, and the field inhomogeneity ($T_2$*). Over all these effects, the FTSED method with IDEAL exhibits the

ability to determine the FF fraction relatively accurately. The FF determined upon the FTSED – IDEAL for samples 10 – 12 significantly differs from the expected (theoretical) values, but the FFs obtained from the chemical shift imaging (CSI) method are closer to the FF achieved with the FTSED – IDEAL. It follows from this assertion that vegetable oil comprises an inconsiderable amount of water, and this is inconsistent with our original assumption of pure oil. The second phantom (Fig. 23 and Fig. 24) was created from lard and water. Lard is an animal fat whose properties are similar to those of fat in a live animal. The water-fat calculation was successful, but in the case of a relatively long ETL compared to short $T_2$ relaxations (Fig. 24) the reconstruction can produce misleading water/fat images and FF maps.

The contrast between water- and fat-dominant voxels can be increased via the modified IDEAL (Appendix B). This is indicated in Fig. 20, where the full triangles with solid black lines represent data calculated through the use of the modified IDEAL algorithm. In the image of fat, signals from the fat-dominated pixels are boosted, while signals from the water-dominated pixels are suppressed. In the case of an equal amount of fat and water in the voxel, the signal in the voxel remains unchanged. The acquired images can be useful, similarly to other contrasts for multiparametric segmentation. The calculated FF maps acquired from the modified IDEAL algorithm do not provide true values.

Compared to the measurement of human patients, the monitoring of small animals brings about specific problems; most importantly, the animal must be anesthetized before each measuring step (+ life functions scanning), and all measurement of the abdomen or heart must be triggered (synchronized). It is vital to note that the metabolism of small animals (e.g., rabbits, rats, mice) is much faster than that of humans or big animals; generally, however, the respiration and heart rate is lower under anesthesia. The heart and respiration rate [172] differs between individual animals. If correct synchronization is not ensured, the motion artefacts can be very strong or the measurement may fail. The coronal (Fig. 25 (A) – (C)) and axial images (Fig. 26 (A) – (C)) acquired by the FTSED sequence were processed by the IDEAL and modified IDEAL algorithms. The rat coronal slice is not motion artefacts-free, but in this case such artefacts are still acceptable. The rat axial slices are strongly affected by motion artefacts because the movement is stronger in the given direction. The undesirable effect of motion artefacts can be observed in the original and calculated water/fat images and, mainly, in the FF map (Fig. 27(J)). Although the motion artefacts cannot be removed completely, they can be reduced through the use of non-Cartesian k-space sampling (e.g., PROPELLER [173] [174]) in the method.

The fast triple-spin echo Dixon (FTSED) sequence applied in this thesis represents a novel, efficient, $T_2$-weighted Dixon imaging method, and it ensures good water/fat separation when combined with iterative decomposition of water and fat, echo asymmetry, and the least-squares estimation (IDEAL) algorithm. The method enables us to acquire 3 raw-data images during one acquisition, and the acquisition time is equal to the original FSE sequence. The method is extremely time-efficient. The time efficiency is comparable to another $T_2$-weighted method, namely the fast spin-echo triple-echo Dixon (fTED) method presented by Ma et al. [149]. In the FTSED method, the time shifts are changed directly, but in the fTED method the

positions of the echoes (the phase encoding strategy) are changed through the BW. A high field means a greater echo shift; thus, the echo shift is much shorter than at a low field. This can be problem for the fTED method, where the echo shifts are controlled through the change of the BW, and the time echo shift is practically limited by the gradient ramp time (to achieve a 180° water-fat phase difference is very problematic). In the case of the FTSED method, the minimal echo shift is practically unlimited. Unlike the fTED method, the FTSED technique using the asymmetric phase encoding strategy ($0$, $\pi$, $2\pi$) appears to be more advantageous than that exploiting the symmetrical encoding strategy ($-\pi$, $0$, $\pi$).

# 8. Conclusion

A new modification of a specific Dixon method was proposed and verified on phantoms and animal subjects. The method was successfully implemented using a 9.4T MRI (Bruker) system at the Institute of Scientific Instruments, ASCR Brno. The fast triple spin echo Dixon (FTSED) sequence is a 3PD time-efficient, $T_2$-weighted method, where 3 images are acquired simultaneously and used for the calculation of water and fat images. Therefore, the method is three time faster in comparison with the asymmetric fast spin echo (AFSE) three-point Dixon (3PD) method. The duration of the FTSED sequence is comparable to the original FSE sequence, and the FTSED method is a single-scan, $T_2$-weighted method providing three images simultaneously. Furthermore, the specific phase-encoding strategy ($0, \pi, 2\pi$) provides three different contrasts (PD, $T_2$*, $T_2$). The method constitutes a viable perspective for preclinical and clinical MR imaging. Successful implementation of the method at a high-field MRI system points to the possibility of the technique being used on a low-field MRI system.

# Appendix A

## *Iterative Least-Squares Estimation Method:*

The measured signal containing *C* spectral components can be expressed as

$$s(t) = \left( \sum_{j=1}^{C} \left( \rho_j \cdot e^{i\left(2\pi \cdot \Delta f_j \cdot \tau\right)} \right) \right) \cdot e^{i\phi}, \tag{56}$$

where $\Delta f_j$ (j, $\ldots, C$) is the chemical shift of the *j*-th component; $\rho_j$ is magnitude of a specific component; $\phi$ represents the magnetic resonance offset in Hz; and the term $2\pi \cdot \Delta f_j \cdot \tau$ is the phase $\varphi_j$ of the *j*-th component. In the case of measurement at defined echo times $\tau_n (n = 1, \ldots, N)$, the signal can be expressed as follows:

$$s_n = \left( \sum_{j=1}^{C} \left( \rho_j \cdot e^{i\left(2\pi \cdot \Delta f_j \cdot \tau_n\right)} \right) \right) \cdot e^{i\phi}, \tag{57}$$

The previous equation contains *C* complex unknowns $\left(\rho_j = \rho_j^R + \rho_j^I\right)$ and one scalar quantity $\phi$; thus, the number of unknowns is $2C + 1$. Each obtained image, for the specified echo time $\tau_n$, contains a real $\left(\rho_j^R\right)$ and an imaginary part $\left(\rho_j^I\right)$. Therefore, $(C + 1)$ image must be acquired for the determination of the system and calculation of the spectral components. For simplification: if we know $\phi = \phi_0$, then the signal for the *n*-th echo time can be expressed as

$$\tilde{s}_n = s_n \cdot e^{-i(\phi)} = \sum_{j=1}^{C} \left( \rho_j \cdot e^{i\left(2\pi \cdot \Delta f_j \cdot \tau_n\right)} \right) \tag{58}$$

The previous equation represent a linear system of complex equations [120], therefore the equation can be expressed as

$$\begin{aligned} \tilde{s}_n &= \tilde{s}_n^r + \tilde{s}_n^i \\ &= \sum_{j=1}^{C} \big[ \left( \tilde{\rho}_j^r \cdot \cos\left(2\pi \cdot \Delta f_j \cdot \tau_n\right) - \tilde{\rho}_j^i \cdot \sin\left(2\pi \cdot \Delta f_j \cdot \tau_n\right) \right) + \\ &\quad + i\left( \tilde{\rho}_j^r \cdot \sin\left(2\pi \cdot \Delta f_j \cdot \tau_n\right) + \tilde{\rho}_j^i \cdot \cos\left(2\pi \cdot \Delta f_j \cdot \tau_n\right) \right) \big]. \end{aligned} \tag{59}$$

*C* denotes the spectral component sets included in the measured signal, and j represents the number of components. Generally, the real and imaginary part of each component can be calculated as follows:

$$\overbrace{\begin{pmatrix} a_{1,1} & -b_{1,1} & \cdots & a_{1,C} & -b_{1,C} \\ b_{1,1} & a_{1,1} & \cdots & b_{1,C} & a_{1,C} \\ \vdots & \vdots & \ddots & \vdots & \vdots \\ \vdots & \vdots & & \vdots & \vdots \\ a_{n,1} & -b_{n,1} & \cdots & a_{n,C} & -b_{n,C} \\ b_{n,1} & a_{n,1} & \cdots & b_{n,C} & a_{n,C} \end{pmatrix}}^{A} \times \overbrace{\begin{pmatrix} \rho_1^r \\ \rho_1^i \\ \vdots \\ \vdots \\ \rho_C^r \\ \rho_C^i \end{pmatrix}}^{\tilde{\rho}} = \overbrace{\begin{pmatrix} {S_1}^r \\ {S_1}^i \\ \vdots \\ \vdots \\ {S_n}^r \\ {S_n}^i \end{pmatrix}}^{S}, \tag{60}$$

where $a = \cos(2\pi \cdot \Delta f \cdot \tau_n)$, $b = \sin(2\pi \cdot \Delta f \cdot \tau_n)$. The coefficients *a* and *b* are known; Δf is obtained from the spectra; $S_n$ denotes the measured signals, each for the defined echo spacing $\tau_n$; and $\rho$ is the vector of known values. In the case of an unknown field inhomogeneity value, the inhomogeneity must be included in the calculation. Thus, the field map error estimation is necessary, which means that the calculation is affected by error owing to an inhomogeneity. If the least-square (LS) fitting is used for the system of linear equations, then

$$\tilde{\rho} = (A^T \cdot A)^{-1} A^T S, \tag{61}$$

where $\tilde{\rho}$ is the initial estimate of each component.

If $\tilde{\rho}_j = \rho_j - \Delta\rho_j$ and $\phi = \phi_0 + \Delta\phi$, then equation (57) can be rewritten as follows:

$$s_n = \left( \sum_{j=1}^{C} \left[ \left( \tilde{\rho}_j + \Delta\rho_j \right) \cdot e^{i(2\pi \cdot \Delta f_j \cdot \tau_n)} \right] \right) \cdot e^{i(\phi_0 + \Delta\phi)} \tag{62}$$

The real and imaginary parts of $\rho_j$ can be defined as $\rho_1^r = \tilde{\rho}_j^r + \Delta\rho_j^r$, $\rho_1^i = \tilde{\rho}_j^i + \Delta\rho_j^i$ and $\phi_0 = \left(2\pi \cdot \Delta f_{\phi_0} \cdot \tau_n\right)$, $\Delta\phi = \left(2\pi \cdot \Delta f_{\Delta\phi} \cdot \tau_n\right)$; thus, the signal can be written as

$$\begin{aligned} s_n = \left( \sum_{j=1}^{C} \left[ \left( \left( \tilde{\rho}_j^r + \Delta\rho_j^r \right) + i\left( \tilde{\rho}_j^i + \Delta\rho_j^i \right) \right) \cdot e^{i(2\pi \cdot \Delta f_j \cdot \tau_n)} \right] \right) \cdot e^{i(2\pi \cdot \Delta f_{\phi_0} \cdot \tau_n)} \cdot \\ \cdot e^{i(2\pi \cdot \Delta f_{\Delta\phi} \cdot \tau_n)}. \end{aligned} \tag{63}$$

Each side of the above equation can be divided by $e^{i(2\pi \cdot \Delta f_{\phi_0} \cdot \tau_n)}$, and using the Taylor approximation $e^{i(2\pi \cdot \Delta f_{\Delta\phi} \cdot \tau_n)} \approx 1 + i\left(2\pi \cdot \Delta f_{\Delta\phi} \cdot \tau_n\right)$ we obtain

$$\begin{aligned} \tilde{s}_n^r + \tilde{s}_n^i = \left( \sum_{j=1}^{C} \left[ \left( \left( \tilde{\rho}_j^r + \Delta\rho_j^r \right) + i\left( \tilde{\rho}_j^i + \Delta\rho_j^i \right) \right) \cdot \left( a_{n,j} + i \cdot b_{n,j} \right) \right] \right) \times \\ \times \left( 1 + i\left( 2\pi \cdot \Delta f_{\Delta\phi} \cdot \tau_n \right) \right). \end{aligned} \tag{64}$$

For the calculation of the field error, it is necessary to calculate the inhomogeneity $\Delta f_{\Delta\phi}$:

$$\tilde{s}_n^r + \tilde{s}_n^i = \left( \sum_{j=1}^{C} \left( \tilde{\rho}_j^r a_{n,j} + i\tilde{\rho}_j^r \, b_{n,j} + \Delta\rho_j^r a_{n,j} + i\Delta\rho_j^r b_{n,j} + i\tilde{\rho}_j^i \, a_{n,j} - \tilde{\rho}_j^i b_{n,j} + \right. \right.$$

$$\left. \left. + i\tilde{\rho}_j^i \, a_{n,j} - \Delta\rho_j^i b_{n,j} \right) \right) \times \left( 1 + i\left( 2\pi \cdot \Delta f_{\Delta\phi} \cdot \tau_n \right) \right)$$

$$= \left( \sum_{j=1}^{C} \left( \tilde{\rho}_j^r a_{n,j} + i\tilde{\rho}_j^r \, b_{n,j} + \Delta\rho_j^r a_{n,j} + i\Delta\rho_j^r b_{n,j} + i\tilde{\rho}_j^i \, a_{n,j} - \tilde{\rho}_j^i b_{n,j} + i\Delta\tilde{\rho}_j^i \, a_{n,j} - \right. \right.$$

$$\left. \left. - \Delta\rho_j^i b_{n,j} \right) \right) + \left( 2\pi \cdot \Delta f_{\Delta\phi} \cdot \tau_n \right) \cdot \tag{65}$$

$$\cdot \left( \sum_{j=1}^{C} \left( i\tilde{\rho}_j^r a_{n,j} - \tilde{\rho}_j^r \, b_{n,j} + i\Delta\rho_j^r a_{n,j} - \Delta\rho_j^r b_{n,j} - \tilde{\rho}_j^i \, a_{n,j} - i\tilde{\rho}_j^i b_{n,j} - \right. \right.$$

$$\left. \left. - \Delta\tilde{\rho}_j^i \, a_{n,j} - i\Delta\rho_j^i b_{n,j} \right) \right).$$

The real part of equation (65):

$$= \left( \sum_{j=1}^{C} \left( \tilde{\rho}_j^r a_{n,j} + \Delta\rho_j^r a_{n,j} - \tilde{\rho}_j^i b_{n,j} - \Delta\rho_j^i b_{n,j} \right) \right) + \left( 2\pi \cdot \Delta f_{\Delta\phi} \cdot \tau_n \right) \cdot$$

$$\cdot \left( \sum_{j=1}^{C} \left( \overbrace{-\tilde{\rho}_j^r \, b_{n,j} - \Delta\rho_j^r b_{n,j}}^{-\rho_j^r \cdot b_{n,j}} \overbrace{-\tilde{\rho}_j^i \, a_{n,j} - \Delta\tilde{\rho}_j^i \, a_{n,j}}^{-\rho_j^i \cdot a_{n,j}} \right) \right). \tag{66}$$

The imaginary part of equation (65):

$$= \left( \sum_{j=1}^{C} \left( \tilde{\rho}_j^r \, b_{n,j} + \Delta\rho_j^r b_{n,j} + \tilde{\rho}_j^i \, a_{n,j} + \Delta\tilde{\rho}_j^i \, a_{n,j} \right) \right) + \left( 2\pi \cdot \Delta f_{\Delta\phi} \cdot \tau_n \right) \cdot$$

$$\cdot \left( \sum_{j=1}^{C} \left( \overbrace{\tilde{\rho}_j^r a_{n,j} + \Delta\rho_j^r a_{n,j}}^{\rho_j^r \cdot a_{n,j}} \overbrace{-\tilde{\rho}_j^i b_{n,j} - \Delta\rho_j^i b_{n,j}}^{-\rho_j^i \cdot b_{n,j}} \right) \right). \tag{67}$$

In the case of a rearrangement of the above equation, we split the formula into a real and an imaginary component. For the real part, we have

$$\tilde{\tilde{s}}_n^r = \tilde{s}_n^r - \sum_{j=1}^{C}\left(\tilde{\rho}_j^r \cdot a - \tilde{\rho}_j^i \cdot b\right) =$$

$$= \left(\left(2\pi \cdot \Delta f_{\Delta\phi} \cdot \tau_n\right) \cdot \sum_{j=1}^{C}\left(-\rho_j^r \cdot b_{n,j} - \rho_j^i \cdot a_{n,j}\right)\right) + \sum_{j=1}^{C} \Delta\rho_j^r \cdot a_{n,j} - \quad (68)$$

$$- \sum_{j=1}^{C} \Delta\rho_j^i \cdot b_{n,j},$$

and the imaginary component is expressed as

$$\tilde{\tilde{s}}_n^i = \tilde{s}_n^i - \sum_{j=1}^{C}\left(\tilde{\rho}_j^r \cdot b + \tilde{\rho}_j^i \cdot a\right) =$$

$$= \left(\left(2\pi \cdot \Delta f_{\Delta\phi} \cdot \tau_n\right) \cdot \sum_{j=1}^{C}\left(\rho_j^r \cdot a_{n,j} - \rho_j^i \cdot b_{n,j}\right)\right) + \quad (69)$$

$$+ \sum_{j=1}^{C}\left(\Delta\rho_j^r \cdot b_{n,j} + \Delta\rho_j^i \cdot a_{n,j}\right).$$

This arrangement enables us to calculate the field inhomogeneity, and we can write the coefficients for the calculation of $g$ such that

$$\Delta f_{\Delta\phi}{}^r = g_n^r = (2\pi \cdot \tau_n) \cdot \sum_{j=1}^{C}\left(-\rho_j^r \cdot b_{n,j} - \rho_j^i \cdot a_{n,j}\right) \quad (70)$$

and

$$\Delta f_{\Delta\phi}{}^i = g_n^i = (2\pi \cdot \tau_n) \cdot \sum_{j=1}^{C}\left(\rho_j^r \cdot a_{n,j} - \rho_j^i \cdot b_{n,j}\right). \quad (71)$$

To calculate the field error, the above equations (68) and (69) can be rearranged to the matrix form

$$\overbrace{\begin{pmatrix} g_1^r & a_{1,1} & -b_{1,1} & \cdots & a_{1,C} & -b_{1,C} \\ g_1^i & a_{1,1} & b_{1,1} & \cdots & b_{1,C} & a_{1,C} \\ & \vdots & \vdots & \ddots & \vdots & \vdots \\ & \vdots & \vdots & & \vdots & \vdots \\ g_n^r & a_{n,1} & -b_{n,1} & \cdots & a_{n,C} & -b_{n,C} \\ g_n^i & b_{n,1} & a_{n,1} & \cdots & b_{n,C} & a_{n,C} \end{pmatrix}}^{B} \times \overbrace{\begin{pmatrix} \Delta\phi \\ \Delta\rho_1^r \\ \Delta\rho_1^i \\ \vdots \\ \Delta\rho_C^r \\ \Delta\rho_C^i \end{pmatrix}}^{\varsigma} = \overbrace{\begin{pmatrix} \tilde{\tilde{S}}_1^{\,r} \\ \tilde{\tilde{S}}_1^{\,i} \\ \vdots \\ \vdots \\ \tilde{\tilde{S}}_n^{\,r} \\ \tilde{\tilde{S}}_n^{\,i} \end{pmatrix}}^{\tilde{\tilde{S}}} \tag{72}$$

Equation (72) is a linear system, and thus the calculation (LSQ method) of vector $\varsigma$ can be performed as follows:

$$\varsigma = (B^T \cdot B)^{-1} B^T \tilde{\tilde{S}}. \tag{73}$$

Iterative least-squares estimation method in conjunction with asymmetric phase encoding strategy is referred as IDEAL [111].

## Appendix B

The contrast between the water- and fat-dominated voxels can be easily reached. The intensity of the second and last images will be attained at the same level as the intensity of the first image; we then have

$$S_{1\mathrm{W}} = (\rho_1 - \rho_2) \cdot \mathrm{e}^{i(\varphi+\varphi_0)} \cdot \frac{|S_0|}{|S_1|} = S_1 \cdot \frac{|S_0|}{|S_1|} \tag{74}$$

$$S_{2\mathrm{W}} = (\rho_1 + \rho_2) \cdot \mathrm{e}^{i(2\varphi+\varphi_0)} \cdot \frac{|S_0|}{|S_1|} = S_2 \cdot \frac{|S_0|}{|S_2|}. \tag{75}$$

The right side of equation (60) will be extended to yield

$$\overbrace{\begin{pmatrix} a_{1,w} & -b_{1,w} & a_{1,f} & -b_{1,f} \\ b_{1,w} & a_{1,w} & b_{1,f} & a_{1,f} \\ a_{2,w} & -b_{2,w} & a_{2,f} & -b_{2,f} \\ b_{2,w} & a_{2,w} & b_{2,f} & a_{2,f} \\ a_{3,w} & -b_{3,w} & a_{3,f} & -b_{3,f} \\ b_{3,w} & a_{3,w} & b_{3,f} & a_{3,f} \end{pmatrix}}^{A} \times \overbrace{\begin{pmatrix} \rho_w^r \\ \rho_w^i \\ \rho_f^r \\ \rho_f^i \end{pmatrix}}^{\tilde{\rho}} = \overbrace{\begin{pmatrix} S_0^{\,r} \cdot 1 \\ S_0^{\,i} \cdot 1 \\ S_1^{\,r} \cdot |S_0|/|S_1| \\ S_1^{\,i} \cdot |S_0|/|S_1| \\ S_2^{\,r} \cdot |S_0|/|S_2| \\ S_2^{\,i} \cdot |S_0|/|S_2| \end{pmatrix}}^{S_W} \tag{76}$$

and the initial estimate $\tilde{\rho}$ can be calculated according to equation (61) as follows:

$$\tilde{\rho} = (A^T \cdot A)^{-1} A^T S_W. \tag{77}$$

Another calculation process is the same as in Appendix A, only with the right side changed. The modification of right side of equation (60) in IDEAL method leads to the "new method" that can be referred as modified IDEAL.

# List of tables

# List of figures

# List of abbreviations

| | | |
|---|---|---|
| 2PD | – | two-point Dixon |
| 3PD | – | three-point Dixon |
| BAT | – | brown adipose tissue |
| BW | – | bandwidth |
| bSSFP | – | balanced steady state precession |
| CBM | – | colored-border map |
| CHESS | – | chemical shift selective imaging |
| CS | – | chemical shift |
| DWI | – | diffusion weighted imaging |
| EPI | – | echo planar imaging |
| ETE | – | effective echo time |
| ETL | – | echo train length |
| Fat-Sat | – | fat saturation |
| FF | – | fat fraction |
| FLAIR | – | fluid attenuated inversion recovery |
| FLASH | – | fast low angle shot magnetic |
| FOV | – | field of view |
| FSE | – | fast spin echo |
| FTSED | – | fast triple spin echo Dixon |
| fTED | – | fast spin echo triple-echo Dixon |
| GRE | – | gradient echo |
| IDEAL | – | iterative decomposition of water and fat with echo asymmetry and least-squares estimation |
| IF | – | in-phase |
| IR | – | inversion recovery |
| ISI | – | institute of scientific instruments |
| MPD | – | multi-point Dixon |
| MR | – | magnetic resonance |
| MRA | – | magnetic resonance angiography |
| MRI | – | magnetic resonance imaging |
| ndb | – | number of double bonds |
| nmidb | – | number of methylene-interrupted double bonds |
| NMR | – | nuclear magnetic resonance |
| NSA | – | number of signal averages |
| OP | – | oppose-phase |

| | | |
|---|---|---|
| PDW | – | proton density weighted |
| PET | – | positron emission tomography |
| PPI | – | partially parallel imaging |
| R-GA | – | region growing algorithm |
| ROI | – | region of interest |
| RF | – | radio frequency |
| SE | – | spin echo |
| SNR | – | signal-to-noise ratio |
| SPAIR | – | spectral attenuated inversion recovery or spectral adiabatic inversion recovery |
| SPD | – | single-point Dixon |
| SPECIAL | – | spectral Inversion at lipid |
| SPGR | – | spoiled gradient echo |
| SPIR | – | spectral presaturation with inversion recovery |
| SPSP | – | spectral-spatial |
| SSFP | – | steady state free precession |
| SSFSE | – | single shot fast spin echo |
| STIR | – | short time inversion recovery |
| SWI | – | susceptibility weighted imaging |
| T1W | – | $T_1$-weighted |
| T2W | – | $T_2$-weighted |
| WAT | – | white adipose tissue |

# List of symbols

| | | | |
|---|---|---|---|
| $\gamma$ | – | gyromagnetic ratio | [rad/s/T] |
| $\Delta\delta$ | – | chemical shift | [ppm] |
| $\Delta x$ | – | chemical shift in the image | [m] |
| $\Delta f_{\mathrm{CS}}$ | – | chemical shift | [Hz] |
| $\Delta f_{wf}$ | – | water and fat difference | [Hz] |
| $\Delta\mathbf{B}_0$ | – | magnetic field inhomogeneity | [T] |
| $\theta$ | – | water-fat phase difference | [rad] |
| $\mu$ | – | magnetic permeability | [H/m] |
| $\mu_0$ | – | magnetic permeability in vacuum | [H/m] |
| $\rho_1$ | – | water component | [-] |
| $\rho_2$ | – | fat component | [-] |
| $\sigma$ | – | shielding constant | [-] |
| $\varphi$ | – | phase | [rad] |
| $\hat{\varphi}$ | – | wrapped phase | [rad] |
| $\varphi_0$ | – | phase error due to system imperfections | [rad] |
| $\chi_m$ | – | magnetic susceptibility | [-] |
| $A_1$, $A_2$ | – | loss factors | [-] |
| $A_{\mathrm{d}}$ | – | diffusion losses | [-] |
| $A_{\mathrm{s}}$ | – | intravoxel susceptibility losses | [-] |
| $A_{\mathrm{w}}$ | – | losses due to spectral broadening | [-] |
| $\mathbf{B}$ | – | magnetic induction | [T] |
| $\mathbf{B}_0$ | – | basic magnetic field | [T] |
| $\mathbf{B}_1$ | – | radio frequency field | [T] |
| $\mathbf{B}_{\mathrm{eff}}$ | – | effective magnetic field at nucleus | [T] |
| $f_0$ | – | Larmor frequency | [Hz] |
| $f_{\mathrm{F}}$ | – | fat frequency | [Hz] |
| $f_{\mathrm{W}}$ | – | water frequency | [Hz] |
| $\mathbf{H}$ | – | intensity of magnetic field | [A/m] |
| $\mathrm{L}(\omega)$ | – | spectrum with Lorentzian distribution | |
| $\mathbf{M}$ | – | magnetization vector | [-] |

| | | | |
|---|---|---|---|
| $M_W$ | – | water magnetization | [-] |
| $M_F$ | – | fat magnetization | [-] |
| $M_{Z(F)}$ | – | longitudinal magnetization of fat | [-] |
| $M_{Z(W)}$ | – | longitudinal magnetization of water | [-] |
| $S$ | – | signal | [-] |
| $T_1$ | – | longitudinal relaxation | [s] |
| $T_2$ | – | transversal relaxation | [s] |
| $T_2^*$ | – | combination of spin-spin relaxation and magnetic field inhomogeneity | [s] |
| $T_2'$ | – | half-width of spectral line | [Hz] |
| $T_I$ | – | inversion time | [s] |
| $T_E$ | – | echo time | [s] |

# List of References


[1] H. Y. Carr, "Free precession techniques in nuclear magnetic resonance.," Harvard University, Cambridge, 1953.

[2] B. MacWilliams, "Russian claims first in magnetic imaging.," *Nature*, vol. 426(375), 27 November 2003.

[3] R. Damadian, „Tumor Detection by Nuclear Magnetic Resonance.," *Science*, pp. 1151-1153, 19 March 1971.

[4] V. D. Schepkin, W. W. Brey, P. L. Gor'kov and S. C. Grant, "Initial in vivo rodent sodium and proton MR imaging at 21.1 T.," *Magn Reson Imaging*, vol. 28(3), pp. 400-407, April 2010.

[5] C. Qian, I. S. Masad, J. T. Rosenberg, M. Elumalai, W. W. Brey, S. C. Grant a P. L. Gor'kov, „A volume birdcage coil with an adjustable sliding tuner ring for neuroimaging in high field vertical magnets: Ex and in vivo applications at 21.1 T.," *Journal of Magnetic Resonance*, sv. 221, pp. 110-116, August 2012.

[6] M. E. Ladd and M. Bock, "Problems and chances of high field magnetic resonance imaging.," *Radiologe*, vol. 53(5), pp. 401-410, May 2013.

[7] P. J. Wright, O. E. Mougin, J. J. Totman, A. M. Peters, M. J. Brookes, R. Coxon, P. E. Morris, M. Clemence, S. T. Francis, R. W. Bowtell and P. A. Gowland, "Water proton T1 measurements in brain tissue at 7, 3, and 1.5 T using IR-EPI, IR-TSE, and MPRAGE: results and optimization.," *MAGMA*, Vols. 21(1-2), pp. 121-130, March 2008.

[8] B. D. Ross, "The biochemistry of living tissue: Examination by MRS.," *NMR Biomed*, vol. 5(5), pp. 215-219, September-October 1992.

[9] B. Ross, R. Kreis and T. Ernst, "Clinical tools for the 90s: magnetic resonance spectroscopy and metabolite imaging.," *Eur J Radiol*, vol. 14(2), pp. 128-140, March-April 1992.

[10] W. G. Proctor and F. C. Yu, "The dependence of a nuclear magnetic resonance frequency upon chemical compound.," *Phys Rev*, vol. 77(5), pp. 717-717, March 1950.

[11] W. C. Dickinson, "Dependence of the F19 Nuclear Resonance Position on Chemical Compound.," *Physical Review*, vol. 77(5), pp. 736-737, 9 January 1950.

[12] T. R. Brown, B. M. Kincaid and K. Ugurbil, "NMR chemical shift imaging in three

dimensions.," *Proc Natl Acad Sci U S A*, vol. 79(11), pp. 3523-3526, June 1982.

[13] I. L. Pykett and B. R. Rosen, "Nuclear magnetic resonance: in vivo proton chemical shift imaging. Work in progress.," vol. 149(1), pp. 197-201, October 1983.

[14] A. A. Maudsley, S. K. Hilal, W. H. Perman and H. E. Simon, "Spatially resolved high resolution spectroscopy by "four-dimensional" NMR.," *J Magn Reson,* vol. 51(1), pp. 147-152, January 1983.

[15] R. Sepponen, J. T. Sipponen and J. I. Tanttu, "A method for chemical shift imaging: demonstration of bone marrow involvement with proton chemical shift imaging.," *J Comput Assist Tomogr,* vol. 8(4), pp. 585-587, August 1984.

[16] Q. Xiang and L. An, "Water-fat imaging with direct phase encoding.," *J Magn Reson Imaging,* vol. 7(6), pp. 1002-1015, Nov-Dec 1997.

[17] G. Hamilton, D. L. J. Smith, M. Bydder, K. S. Nayak and H. H. Hu, "MR properties of brown and white adipose tissues.," *J Magn Reson Imaging,* vol. 34(2), pp. 468-473, Aug 2011.

[18] A. L. Albright and J. S. Stern, "Adipose tissue," in *Encyclopedia of Sports Medicine and Science,* 1998.

[19] R. G. Vernon and D. J. Flint, "ADIPOSE TISSUE | Structure and Function of White Adipose Tissue," in *Encyclopedia of Food Sciences and Nutrition (Second Edition),* Academic Press, 2003, pp. 23-29.

[20] Z. L. Mazurek T, A. Zalewski, J. D. Mannion, J. T. Diehl, H. Arafat, L. Sarov-Blat, S. O'Brien, E. A. Keiper, A. G. Johnson, J. Martin, B. J. Goldstein and Y. Shi, "Human epicardial adipose tissue is a source of inflammatory mediators.," *Circulation,* vol. 108(20), pp. 2460-2466, 18 November 2003.

[21] G. Iacobellisl, D. Corradi a A. M. Sharma, „Epicardial adipose tissue: anatomic, biomolecular and clinical relationships with the heart.," *Nat Clin Pract Cardiovasc Med,* sv. 2, pp. 536-543, 18 July 2005.

[22] After T. L. Lentz, Cell Fine Structure: An Atlas of Drawings of Whole-Cell Structure, W. B. Saunders, 1971.

[23] M. W. King, *Adipose Tissue: Not Just Fat*, 2013.

[24] P. Lee, M. M. Swarbrick and K. K. Ho, "Brown Adipose Tissue in Adult Humans: A Metabolic Renaissance.," *Endocr Rev,* vol. 34(3), pp. 413-438, June 2013.

[25] J. Mishra, "Importance of thermoregulation in the newborn: role of the brown fat.,"

*Orissa Journal of Medical Biochemistry*, vol. 1, pp. 75-76, 2004.

[26] J. Himms-Hagen, "Obesity may be due to a malfunctioning of brown fat.," *Can Med Assoc J.*, vol. 121(10), pp. 1361-1364, 17 November 1979.

[27] B. Cannon a J. Nedergaard, „Brown adipose tissue: function and physiological significance.," *Physiol Rev*, sv. 84(1), pp. 277-359, 2004.

[28] B. B. Lowell and J. S. Flier, "Brown adipose tissue, beta 3-adrenergic receptors, and obesity.," *Annu Rev Med*, vol. 48, pp. 307-316, 1997.

[29] P. Huttunen, J. Hirvonen and V. Kinnula, "The occurrence of brown adipose tissue in outdoor workers.," *Eur J Appl Physiol Occup Physiol*, vol. 46(4), pp. 339-345, 1981.

[30] J. Nedergaard, T. Bengtsson and B. Cannon, "Unexpected evidence for active brown adipose tissue in adult humans.," *Am J Physiol Endocrinol Metab*, vol. 293(2), pp. E444-E452, August 2007.

[31] A. M. Cypess, S. Lehman, G. Williams, I. Tal, D. Rodman, A. B. Goldfine, F. C. Kuo, E. L. Palmer, Y.-H. Tseng, A. Doria, G. M. Kolodny and C. R. Kahn, "Identification and importance of brown adipose tissue in adult humans.," *N Engl J Med*, vol. 360(15), pp. 1509-1517, 9 April 2009.

[32] Y. I. Chen, A. M. Cypess, C. A. Sass, A. L. Brownell, K. T. Jokivarsi, C. R. Kahn and K. K. Kwong, "Anatomical and functional assessment of brown adipose tissue by magnetic resonance imaging.," *Obesity (Silver Spring)*, vol. 20(7), pp. 1519-1526, Jul 2012.

[33] H. H. Hu, D. L. J. Smith, K. S. Nayak, M. I. Goran and T. R. Nagy, "Identification of Brown Adipose Tissue in Mice with Fat-Water IDEAL-MRI.," *J Magn Reson Imaging*, vol. 31(5), pp. 1195-1202, May 2010.

[34] T. Lauenstein, P. Sharma, T. Hughes, K. Heberlein, D. Tudorascu and D. Martin, "Evaluation of optimized inversion-recovery fat-suppression techniques for T2-weighted abdominal MR imaging.," *J Magn Reson Imaging*, vol. 27(6), pp. 1448-1454, June 2008.

[35] T. Shonai, T. Takahashi, H. Ikeguchi, M. Miyazaki, K. Amano and M. Yui, "Improved arterial visibility using short-tau inversion-recovery (STIR) fat suppression in non-contrast-enhanced time-spatial labeling inversion pulse (Time-SLIP) renal MR angiography (MRA).," *J Magn Reson Imaging*, vol. 29(6), pp. 1471-1477, June 2009.

[36] L. Havla, T. Basha, H. Rayatzadeh, J. Shaw, W. Manning, S. Reeder, S. Kozerke and R. Nezafat, "Improved fat water separation with water selective inversion pulse for inversion recovery imaging in cardiac MRI.," *J Magn Reson Imaging*, vol. 37(2), pp.

484-490, February 2013.

[37] M. Francone, I. Carbone, L. Agati, D. C. Bucciarelli, M. Mangia, I. Iacucci, C. Catalano and R. Passariello, "Utility of T2-weighted short-tau inversion recovery (STIR) sequences in cardiac MRI: an overview of clinical applications in ischaemic and non-ischaemic heart disease.," *Radiol Med,* vol. 116(1), pp. 32-46, February 2011.

[38] C. Denoiseux, I. Boulay-Coletta, J. Nakache, I. Claude and M. Zins, "Liver T2-weighted MR imaging: assessment of a three-dimensional fast spin-echo with extended echo train acquisition sequence at 1.5 Tesla.," *J Magn Reson Imaging,* vol. 38(2), pp. 336-343, August 2013.

[39] P. Hors, "A new method for water suppression in the proton NMR spectra of aqueous solutions.," *J. Magn. Reson. (1969),* vol. 54(3), pp. 539-542, 1 October 1983.

[40] J. M. Patsch, X. Li, T. Baum, S. P. Yap, D. C. Karampinos, A. V. Schwartz and T. M. Link, "Bone marrow fat composition as a novel imaging biomarker in postmenopausal women with prevalent fragility fractures.," *J Bone Miner Res,* vol. 28(8), pp. 1721-1728, August 2013.

[41] E. M. Delfaut, J. Beltran, G. Johnson, J. Rousseau, X. Marchandise and A. Cotten, "Fat suppression in MR imaging: techniques and pitfalls.," *Radiographics,* vol. 19(2), pp. 373-382, March-April 1999.

[42] T. A. Bley, O. Wieben, C. J. François, J. H. Brittain and S. B. Reeder, "Fat and water magnetic resonance imaging.," *J Magn Reson Imaging,* vol. 31(1), pp. 4-18, January 2010.

[43] X. Li, J. Youngren, B. Hyun, G. Sakkas, K. Mulligan, S. Majumdar, U. Masharani, M. Schambelan and I. Goldfine, "Technical evaluation of in vivo abdominal fat and IMCL quantification using MRI and MRSI at 3 T.," *Magn Reson Imaging,* vol. 26(2), pp. 188-197, February 2008.

[44] D. Armao, J. Guyon, Z. Firat, M. Brown and R. Semelka, "Accurate quantification of visceral adipose tissue (VAT) using water-saturation MRI and computer segmentation: preliminary results.," *J Magn Reson Imaging,* vol. 23(5), pp. 736-741, May 2006.

[45] J. Machann, C. Thamer, B. Schnoedt, M. Haap, H. Haring, C. Claussen, M. Stumvoll, A. Fritsche and F. Schick, "Standardized assessment of whole body adipose tissue topography by MRI.," *J Magn Reson Imaging,* vol. 21(4), pp. 455-462, April 2005.

[46] S. R. Mehta, E. L. Thomas, J. D. Bell, D. G. Johnston and S. D. Taylor-Robinson, "Non-invasive means of measuring hepatic fat content.," *World J Gastroenterol,* vol. 14(22), pp. 3476-3483, 14 June 2008.

[47] S. Reeder, P. Robson, H. Yu, A. Shimakawa, C. Hines, C. McKenzie and J. Brittain, "Quantification of hepatic steatosis with MRI: the effects of accurate fat spectral modeling.," *J Magn Reson Imaging,* vol. 29(6), pp. 1332-1339, June 2009.

[48] B. Guiu, J. Petit, R. Loffroy, S. D. Ben, S. Aho, D. Masson, P. Hillon, D. Krause and J. Cercueil, "Quantification of liver fat content: comparison of triple-echo chemical shift gradient-echo imaging and in vivo proton MR spectroscopy.," *Radiology,* vol. 250(1), pp. 95-102, January 2009.

[49] H. Kim, S. Taksali, S. Dufour, D. Befroy, T. Goodman, K. Petersen, G. Shulman, S. Caprio and R. Constable, "Comparative MR study of hepatic fat quantification using single-voxel proton spectroscopy, two-point dixon and three-point IDEAL.," *Magn Reson Med,* vol. 59(3), pp. 521-527, March 2008.

[50] C. Liu, C. McKenzie, H. Yu, J. Brittain and S. Reeder, "Fat quantification with IDEAL gradient echo imaging: correction of bias from T(1) and noise.," *Magn Reson Med,* vol. 58(2), pp. 354-364, August 2007.

[51] K. Fumiko, M. Yuka, N. Takatomo, N. Toshio, K. Shunji, S. Seiya, H. Nobuhisa and S. Fumikazu, "Myocardial Fat at Cardiac Imaging: How Can We Differentiate Pathologic from Physiologic Fatty Infiltration?," *Radiographics,* vol. 30, pp. 1587-1602, October 2010.

[52] P. Kellman, D. Hernando and A. E. Arai, "Myocardial Fat Imaging.," *Curr Cardiovasc Imaging Rep,* vol. 3(2), pp. 83-91, April 2010.

[53] C. Y. Liu, A. Redheuil, R. Ouwerkerk, J. A. Lima and D. A. Bluemke, "Myocardial fat quantification in humans: Evaluation by two-point water-fat imaging and localized proton spectroscopy.," *Magn Reson Med,* vol. 63(4), pp. 892-901, April 2010.

[54] J. Guy, J. Mao, W. D. J. Bidgood, A. Mancuso and R. G. Quisling, "Enhancement and demyelination of the intraorbital optic nerve. Fat suppression magnetic resonance imaging.," *Ophthalmology,* vol. 99(5), pp. 713-719, May 1992.

[55] D. H. Miller, D. G. Mac Manus, P. A. Bartlett, R. Kapoor, S. P. Morrissey and I. F. Moseley, "Detection of optic nerve lesions in optic neuritis using frequency-selective fat-saturation sequences.," *Neuroradiology,* vol. 35(2), pp. 156-158, 1993.

[56] R. A. de Graaf, In vivo NMR spectroscopy, principles and techniques, Chichester: John Viley & Son, 1998.

[57] J. C. Hindman, "Proton Resonance Shift of Water in the Gas and Liquid States.," *J Chem Phys,* vol. 44, pp. 4582-4592, June 1966.

[58] V. Rieke and K. Butts Pauly, "MR thermometry.," *J Magn Reson Imaging,* vol. 27(2),

pp. 376-390, February 2008.

[59] N. J. Baxter and M. P. Williamson, “Temperature dependence of 1H chemical shifts in proteins.,” *J Biomol NMR,* vol. 9(4), pp. 359-369, June 1997.

[60] E. M. Haacke, R. W. Brown, M. R. Thompson and R. Venkatesan, Magnetic Resonance Imaging: Physical Principles and Sequence Design., Wiley, 1999.

[61] D. C. Alsop, T. J. Connick and G. Mizsei, “A spiral volume coil for improved RF field homogeneity at high static magnetic field strength.,” *Magn Reson Med,* vol. 40(1), pp. 49-54, July 1998.

[62] T. S. Ibrahim, R. Lee, B. A. Baertlein, A. M. Abduljalil, H. Zhu and P. M. Robitaille, “Effect of RF coil excitation on field inhomogeneity at ultra high fields: a field optimized TEM resonator.,” *Magn Reson Imaging,* vol. 19(10), pp. 1339-1347, December 2001.

[63] R. S. Staewen, A. J. Johnson, B. D. Ross, T. Parrish, H. Merkle and M. Garwood, “3-D FLASH imaging using a single surface coil and a new adiabatic pulse, BIR-4.,” *Invest Radiol,* vol. 25(5), pp. 559-567, May 1990.

[64] R. Deichmann, C. D. Good, O. Josephs, J. Ashburner and R. Turner, “Optimization of 3-D MP-RAGE sequences for structural brain imaging.,” *Neuroimage,* vol. 12(1), pp. 112-127, July 2000.

[65] S. Clare, M. Alecci and P. Jezzard, “Compensating for B(1) inhomogeneity using active transmit power modulation.,” *Magn Reson Imaging,* vol. 19(10), pp. 1349-1352, December 2001.

[66] S. Saekho, “B1 INHOMOGENEITY COMPENSATION IN MAGNETIC RESONANCE IMAGING (MRI),” 2005.

[67] Z. Zhang, C. Y. Yip, W. Grissom, D. C. Noll, F. E. Boada and V. A. Stenger, “Reduction of transmitter B1 inhomogeneity with transmit SENSE slice-select pulses.,” *Magn Reson Med,* vol. 57(5), pp. 842-847, May 2007.

[68] V. A. Stenger, F. E. Boada and D. C. Noll, “Multishot 3D slice-select tailored RF pulses for MRI.,” *Magn Reson Med,* vol. 48(1), pp. 157-165, July 2002.

[69] H. Mihara, N. Iriguchi and S. Ueno, “A method of RF inhomogeneity correction in MR imaging.,” *MAGMA,* vol. 7(2), pp. 115-120, December 1998.

[70] M. S. Cohen, R. M. DuBois and M. M. Zeineh, “Rapid and effective correction of RF inhomogeneity for high field magnetic resonance imaging.,” *Hum Brain Mapp,* vol. 10(4), pp. 204-211, August 2000.

[71] G. M. Bydder and I. R. Young, “MR imaging: clinical use of the inversion recovery sequence.,” *J Comput Assist Tomogr*, vol. 9(4), pp. 659-675, July-August 1985.

[72] G. M. Bydder, J. M. Pennock, R. E. Steiner, S. Khenia, J. A. Payne and I. R. Young, “The short TI inversion recovery sequence--an approach to MR imaging of the abdomen.,” *Magn Reson Imaging*, vol. 3(3), pp. 251-254, 1985.

[73] G. M. Bydder, R. E. Steiner, L. H. Blumgart, S. Khenia and I. R. Young, “MR imaging of the liver using short TI inversion recovery sequences.,” *J Comput Assist Tomogr*, vol. 9(6), pp. 1084-1089, November-December 1985.

[74] E. Kaldoudi, S. C. Williams, G. J. Barker and P. S. Tofts, “A chemical shift selective inversion recovery sequence for fat-suppressed MRI: theory and experimental validation.,” *Magn Reson Imaging*, vol. 11(3), pp. 341-355, 1993.

[75] K. Tanabe, K. Nishikawa, T. Sano, O. Sakai and H. Jara, “Fat suppression with short inversion time inversion-recovery and chemical-shift selective saturation: a dual STIR-CHESS combination prepulse for turbo spin echo pulse sequences.,” *J Magn Reson Imaging*, vol. 31(5), pp. 1277-1281, May 2010.

[76] M. Brant-Zawadzki, D. Atkinson, M. Detrick, W. Bradley and G. Scidmore, “Fluid-attenuated inversion recovery (FLAIR) for assessment of cerebral infarction. Initial clinical experience in 50 patients.,” *Stroke*, vol. 27(7), pp. 1187-1191, July 1996.

[77] T. S. Ibrahim, R. Lee, A. M. Abduljalil, B. A. Baertlein and P. M. Robitaille, "Dielectric resonances and B(1) field inhomogeneity in UHFMRI: computational analysis and experimental findings.," *Magn Reson Imaging*, vol. 19(2), pp. 219-226, February 2001.

[78] R. A. De Graaf and K. Nicolay, “Adiabatic rf pulses: Applications to in vivo NMR.,” *Concepts in Magnetic Resonance*, vol. 9(4), pp. 247-268, 7 December 1998.

[79] D. G. Norris, “Adiabatic radiofrequency pulse forms in biomedical nuclear magnetic resonance.,” *Concepts in Magnetic Resonance*, vol. 14(2), pp. 89-101, 12 February 2002.

[80] M. Garwood and L. DelaBarre, “The Return of the Frequency Sweep: Designing Adiabatic Pulses for Contemporary NMR.,” *J Magn Reson*, vol. 153(2), pp. 155-177, December 2001.

[81] A. Haase, J. Frahm, W. Hänicke and D. Matthaei, “1H NMR chemical shift selective (CHESS) imaging.,” *Phys Med Biol*, vol. 30(4), pp. 341-344, April 1985.

[82] J. Mao, H. Yan, W. W. Brey, W. D. J. Bidgood, J. J. Steinbach and A. Mancuso, “Fat tissue and fat suppression.,” *Magn Reson Imaging*, vol. 11(3), pp. 385-393, 1993.

[83] C. H. Meyer, J. M. Pauly, A. Macovski and D. G. Nishimura, “Simultaneous spatial and spectral selective excitation.,” *Magn Reson Med,* vol. 15(2), pp. 287-304, August 1990.

[84] D. Spielman, C. Meyer, A. Macovski and D. Enzmann, "1H spectroscopic imaging using a spectral-spatial excitation pulse.," *Magn Reson Med,* vol. 18(2), pp. 269-279, April 1991.

[85] F. Schick, "Simultaneous highly selective MR water and fat imaging using a simple new type of spectral-spatial excitation.," *Magn Reson Med,* vol. 40(2), pp. 194-202, August 1998.

[86] J. M. Pauly, D. G. Nishimura and A. Macovski, "A k-space analysis of small-tip-angle excitation.," *Journal of Magnetic Resonance,* vol. 81, pp. 43-56, 11 April 1988.

[87] Y. Zur, "Design of improved spectral-spatial pulses for routine clinical use.," *Magn Reson Med,* vol. 43(3), pp. 410-420, March 2000.

[88] M. Bernstein, K. King and X. Zhou, Handbook of MRI Pulse Sequences, Academic Press, 2004, p. 1040.

[89] F. Schick, J. Forster, J. Machann, P. Huppert and C. D. Claussen, "Highly selective water and fat imaging applying multislice sequences without sensitivity to B1 field inhomogeneities.," *Magn Reson Med,* vol. 38(2), pp. 269-274, August 1997.

[90] W. Block, J. Pauly, A. Kerr and D. Nishimura, "Improved spectral-spatial pulses through Bo eddy current compensation.," in *Proc., ISMRM, 4th Annual Meeting*, New York, 1996.

[91] "Improved solvent suppression and increased spatial excitation bandwidths for three-dimensional PRESS CSI using phase-compensating spectral/spatial spin-echo pulses.," *J Magn Reson Imaging,* vol. 7(4), pp. 745-757, July-August 1997.

[92] F. Schick, J. Forster, J. Machann, R. Kuntz and C. Claussen, "Improved clinical echo-planar MRI using spatial-spectral excitation.," *J Magn Reson Imaging*, vol. 8(4), pp. 960-967, July-August 1998.

[93] C. Leong, B. Daniel, R. Herfkens, R. Birdwell, S. Jeffrey, D. Ikeda, A. Sawyer-Glover and G. Glover, "Characterization of breast lesion morphology with delayed 3DSSMT: an adjunct to dynamic breast MRI.," *J Magn Reson Imaging*, vol. 11(2), pp. 87-96, February 2000.

[94] W. Block, J. Pauly, A. Kerr and D. Nishimura, "Consistent fat suppression with compensated spectral-spatial pulses.," *Magn Reson Med,* vol. 38(2), pp. 198-206, August 1997.

[95] J. Yuan, B. Madore and L. Panych, "Fat-water selective excitation in balanced steady-state free precession using short spatial-spectral RF pulses.," *J Magn Reson,* vol. 208(2), pp. 219-224, February 2011.

[96] F. Schick, "Pulsed magnetization transfer contrast MRI by a sequence with water selective excitation.," *J Comput Assist Tomogr,* vol. 20(1), pp. 73-79, January-February 1996.

[97] O. Bieri, T. Mamisch, S. Trattnig, O. Kraff, M. Ladd and K. Scheffler, "Optimized spectrally selective steady-state free precession sequences for cartilage imaging at ultra-high fields.," *MAGMA,* Vols. 21(1-2), pp. 87-94, March 2008.

[98] D. Thomasson, D. Purdy and J. Finn, "Phase-modulated binomial RF pulses for fast spectrally-selective musculoskeletal imaging.," *Magn Reson Med,* vol. 35(4), April 1996.

[99] X. Deligianni, P. Bär, K. Scheffler, S. Trattnig and O. Bieri, "Water-selective excitation of short T2 species with binomial pulses.," *Magn Reson Med,* vol. 00, pp. 1-6, 7 October 2013.

[100] W. T. Dixon, "Simple proton spectroscopic imaging.," *Radiology,* vol. 153(1), pp. 189-194, October 1984.

[101] J. Ma, "Dixon techniques for water and fat imaging.," *J Magn Reson Imaging,* vol. 28(3), pp. 543-558, September 2008.

[102] H. N. Yeung and D. W. Kormos, "Separation of true fat and water images by correcting magnetic field inhomogeneity in situ.," *Radiology,* vol. 159(3), pp. 783-786, June 1986.

[103] G. H. Glover and E. Schneider, "Three-point Dixon technique for true water/fat decomposition with B0 inhomogeneity correction.," *Magn Reson Med,* vol. 18(2), pp. 371-383, April 1991.

[104] G. H. Glover, "Multipoint dixon technique for water and fat proton and susceptibility imaging.," *J Magn Reson Imaging,* vol. 1(5), pp. 521-530, September-October 1991.

[105] Q. S. Xiang and L. An, "Water-fat imaging with direct phase encoding.," *J Magn Reson Imaging,* vol. 7(6), pp. 1002-1015, November-December 1997.

[106] B. D. Coombs, J. Szumowski and W. Coshow, "Two-point Dixon technique for water-fat signal decomposition with B0 inhomogeneity correction.," *Magn Reson Med,* vol. 38(6), pp. 884-889, December 1997.

[107] T. Skinner and G. H. Glover, "An extended two-point Dixon algorithm for calculating separate water, fat, and B0 images.," *Magn Reson Med,* vol. 37(4), pp. 628-630, April

1997.

[108] J. Berglund, H. Ahlström, L. Johansson and J. Kullberg, "Two-point dixon method with flexible echo times.," *Magn Reson Med,* vol. 65(4), pp. 994-1004, April 2011.

[109] H. Yu, A. Shimakawa, C. A. McKenzie, E. Brodsky, J. H. Brittain and S. B. Reeder, "Multiecho water-fat separation and simultaneous R2* estimation with multifrequency fat spectrum modeling.," *Magn Reson Med,* vol. 60(5), pp. 1122-1134, November 2008.

[110] Q. S. Xiang, "Two-point water-fat imaging with partially-opposed-phase (POP) acquisition: an asymmetric Dixon method.," *Magn Reson Med,* vol. 56(3), pp. 572-584, September 2006.

[111] S. Reeder, A. Pineda, Z. Wen, A. Shimakawa, H. Yu, J. Brittain, G. Gold, C. Beaulieu and N. Pelc, "Iterative decomposition of water and fat with echo asymmetry and least-squares estimation (IDEAL): application with fast spin-echo imaging.," *Magn Reson Med,* vol. 54(3), pp. 636-644, September 2005.

[112] A. Pineda, S. Reeder, Z. Wen and N. Pelc, "Cramér-Rao bounds for three-point decomposition of water and fat.," *Magn Reson Med,* vol. 54(3), pp. 625-635, September 2005.

[113] D. Hernando, P. Kellman, J. P. Haldar and Z. P. Liang, "Robust water/fat separation in the presence of large field inhomogeneities using a graph cut algorithm.," *Magn Reson Med,* vol. 63(1), pp. 79-90, January 2010.

[114] H. Yu, S. B. Reeder, A. Shimakawa, J. H. Brittain and N. J. Pelc, "Field map estimation with a region growing scheme for iterative 3-point water-fat decomposition.," *Magn Reson Med,* vol. 54(4), pp. 1032-1039, October 2005.

[115] J. Ma, "A single-point Dixon technique for fat-suppressed fast 3D gradient-echo imaging with a flexible echo time.," *J Magn Reson Imaging,* vol. 27(4), pp. 881-890, April 2008.

[116] E. M. Akkerman and M. Maas, "A region-growing algorithm to simultaneously remove dephasing influences and separate fat and water in two-point Dixon imaging.," in *Society for Magnetic Resonance in Medicine and the European Society for Magnetic Resonance in Medicine and Biology Meeting*, Berkeley, California, 1995.

[117] G. Z. Yang, D. N. Firmin, R. H. Mohhiadin, J. P. Konrad and D. B. Longmore, "B0 inhomogeneity correction for two point Dixon chemical shift imaging," in *Proc., SMRM, 11th annual Meeting*, Berlin, Germany, 1992.

[118] D. Ragan and J. Bankson, "Two-point Dixon technique provides robust fat suppression for multi-mouse imaging.," *J Magn Reson Imaging,* vol. 31(2), pp. 510-514, February

2010.

[119] H. Yu, S. Reeder, C. McKenzie, A. Brau, A. Shimakawa, J. Brittain and N. Pelc, “Single acquisition water-fat separation: feasibility study for dynamic imaging.,” *Magn Reson Med,* vol. 55(2), pp. 413-422, February 2006.

[120] S. Reeder, Z. Wen, H. Yu, A. Pineda, G. Gold, M. Markl and N. Pelc, “Multicoil Dixon chemical species separation with an iterative least-squares estimation method.,” *Magn Reson Med,* vol. 51(1), pp. 35-45, January 2004.

[121] L. An and Q. Xiang, “Chemical shift imaging with spectrum modeling.,” *Magn Reson Med,* vol. 46(1), pp. 126-130, July 2001.

[122] D. Hernando, J. Haldar, B. Sutton, J. Ma, P. Kellman and Z. Liang, “Joint estimation of water/fat images and field inhomogeneity map.,” *Magn Reson Med,* vol. 59(3), pp. 571-580, March 2008.

[123] V. Chebrolu, C. Hines, H. Yu, A. Pineda, A. Shimakawa, C. McKenzie, A. Samsonov, J. Brittain and S. Reeder, “Independent estimation of T*2 for water and fat for improved accuracy of fat quantification.,” *Magn Reson Med,* vol. 63(4), pp. 849-857, April 2010.

[124] M. Bydder, T. Yokoo, G. Hamilton, M. Middleton, A. Chavez, J. Schwimmer, J. Lavine and C. Sirlin, “Relaxation effects in the quantification of fat using gradient echo imaging.,” *Magn Reson Imaging,* vol. 26(3), pp. 347-359, April 2008.

[125] C. Hines, H. Yu, A. Shimakawa, C. McKenzie, J. Brittain and S. Reeder, “T1 independent, T2* corrected MRI with accurate spectral modeling for quantification of fat: validation in a fat-water-SPIO phantom.,” *J Magn Reson Imaging,* vol. 30(5), pp. 1215-1222, November 2009.

[126] J. Pauly, “Dixon reconstruction,” pp. 1-6, October 2007.

[127] J. C. Ford and F. W. Wehrli, “In vivo quantitative characterization of trabecular bone by NMR interferometry and localized proton spectroscopy.,” *Magn Reson Med,* vol. 17(2), pp. 543-551, February 1991.

[128] J. M. Bioucas-Dias and G. Valadao, “Phase Unwrapping via Graph Cuts.,” *Image Processing, IEEE Transactions on,* vol. 16(3), pp. 698-709, March 2007.

[129] D. C. Ghiglia and M. D. Pritt, Two-Dimensional Phase Unwrapping: Theory, Algorithms, and Software, Wiley-Interscience, 1998.

[130] E. Schneider and G. Glover, "Rapid in vivo proton shimming.," *Magn Reson Med,* vol. 18(2), pp. 335-347, April 1991.

[131] Z. Liang, “A model-based method for phase unwrapping.,” *IEEE Trans Med Imaging,* vol. 15(6), pp. 893-897, 1996.

[132] S. Chavez, Q. Xiang and L. An, "Understanding phase maps in MRI: a new cutline phase unwrapping method.," *IEEE Trans Med Imaging,* vol. 21(8), pp. 966-977, August 2002.

[133] J. Szumowski, W. Coshow, F. Li and S. Quinn, "Phase unwrapping in the three-point Dixon method for fat suppression MR imaging.," *Radiology,* vol. 192(2), pp. 555-561, August 1994.

[134] H. Yu, S. Reeder, A. Shimakawa, J. Brittain and N. Pelc, "Field map estimation with a region growing scheme for iterative 3-point water-fat decomposition.," *Magn Reson Med,* vol. 54(4), pp. 1032-1039, October 2005.

[135] Y. Wang, D. Li, E. Haacke and J. Brown, "A three-point Dixon method for water and fat separation using 2D and 3D gradient-echo techniques.," *J Magn Reson Imaging,* vol. 8(3), pp. 703-710, May-June 1998.

[136] M. Jacob and B. Sutton, "Non-iterative decomposition of fat and water using chemical shift.," in *Joint Annual Meeting ISMRM-ESMRMB (abstract 1630)*, Berlin, 2007.

[137] J. Ma, "Breath-hold water and fat imaging using a dual-echo two-point Dixon technique with an efficient and robust phase-correction algorithm.," *Magn Reson Med,* vol. 52(2), pp. 415-419, August 2004.

[138] H. Eggers, B. Brendel and G. Herigault, "Comparison of Dixon Methods for Fat Suppression in Single Breath-Hold 3D Gradient-Echo Abdominal MRI.," in *Proceedings of the 17th Annual Meeting of ISMRM*, Honolulu, 2009.

[139] Z. Paltiel and A. Ban, "Separate water and lipids images obtained by a single scan.," in *Proceedings of the International Society for Magnetic Resonance in Medicine*, London, 1985.

[140] J. Patrick, E. Haacke and J. Hahn, "Water/fat separation and chemical shift artifact correction using a single scan.," in *Proceedings of the International Society for Magnetic Resonance in Medicine*, London, 1985.

[141] C. Ahn, S. Lee, O. Nalcioglu and Z. Cho, "Spectroscopic imaging by quadrature modulated echo time shifting.," *Magn Reson Imaging,* vol. 4(2), p. 110, 1986.

[142] J. Hajnal and I. Young, "Use of spatial phase distribution models to produce water and fat only images from single echo shifted data sets.," in *Proceedings of the International Society for Magnetic Resonance in Medicine*, San Francisco, 1995.

[143] Q. Xiang, "Fat suppression with single quadrature acquisition," in *Proceedings of the 6th Annual Scientific Meeting of the ISMRM*, Sydney, 1998.

[144] Q. Xiang, "Improved single point water-fat imaging with virtual shimming," in *Proceedings of the 9th Annual Scientific Meeting of the ISMRM*, Glasgow, 2001.

[145] J. Son, J. Ji and J. Ma, "Three-dimensional T1-weighted MR Imaging using a One-point Dixon Technique with Arbitrary Echo Time," in *Proc. Intl. Soc. Mag. Reson. Med. 13*, Florida, 2005.

[146] J. Son, S. Wright and J. Ji, "Single-point Dixon water-fat imaging using 64-channel single-echo acquisition MRI.," *Concepts in Magnetic Resonance Part B: Magnetic Resonance Engineering*, vol. 33B(3), pp. 152-162, August 2008.

[147] P. Hardy, R. Hinks and J. Tkach, "Separation of fat and water in fast spin-echo MR imaging with the three-point Dixon technique.," *J Magn Reson Imaging*, vol. 5(2), pp. 181-185, March-April 1995.

[148] J. Ma, S. Singh, A. Kumar, N. Leeds and L. Broemeling, "Method for efficient fast spin echo Dixon imaging.," *Magn Reson Med*, vol. 48(6), pp. 1021-1027, December 2002.

[149] J. Ma, J. Son, Y. Zhou, H. Le-Petross and H. Choi, "Fast spin-echo triple-echo dixon (fTED) technique for efficient T2-weighted water and fat imaging.," *Magn Reson Med*, vol. 58(1), pp. 103-109, July 2007.

[150] C. Costelloe, V. Kundra, J. Ma, B. Chasen, E. Rohren, R. J. Bassett and J. Madewell, "Fast Dixon whole-body MRI for detecting distant cancer metastasis: a preliminary clinical study.," *J Magn Reson Imaging*, vol. 35(2), pp. 399-408, February 2012.

[151] T. Huang, H. Chung, F. Wang, C. Ko and C. Chen, "Fat and water separation in balanced steady-state free precession using the Dixon method.," *Magn Reson Med*, vol. 51(2), pp. 243-247, February 2004.

[152] R. Stafford, M. Sabati, H. Mahallati and R. Frayne, "3D non-contrast-enhanced MR angiography with balanced steady-state free precession Dixon method.," *Magn Reson Med*, vol. 59(2), pp. 430-433, February 2008.

[153] J. Glockner, M. Saranathan, E. Bayram and C. Lee, "Breath-held MR cholangiopancreatography (MRCP) using a 3D Dixon fat-water separated balanced steady state free precession sequence.," *Magn Reson Imaging*, vol. 31(8), pp. 1263-1270, October 2013.

[154] H. Moriguchi, J. Lewin and J. Duerk, "Dixon techniques in spiral trajectories with off-resonance correction: a new approach for fat signal suppression without spatial-spectral RF pulses.," *Magn Reson Med*, vol. 50(5), pp. 915-924, November 2003.

[155] H. Moriguchi, J. Lewin and J. Duerk, "Fast Spiral two-point Dixon technique using block regional off-resonance correction.," *Magn Reson Med,* vol. 52(6), pp. 1342-1350, December 2004.

[156] H. Wu, J. Lee and D. Nishimura, "Fat/water separation using a concentric rings trajectory.," *Magn Reson Med,* vol. 61(3), pp. 639-649, March 2009.

[157] D. Sodickson and W. Manning, "Simultaneous acquisition of spatial harmonics (SMASH): fast imaging with radiofrequency coil arrays.," *Magn Reson Med,* vol. 38(4), pp. 591-603, October 1997.

[158] M. Griswold, P. Jakob, R. Heidemann, M. Nittka, V. Jellus, J. Wang, B. Kiefer and A. Haase, "Generalized autocalibrating partially parallel acquisitions (GRAPPA).," *Magn Reson Med,* vol. 47(6), pp. 1202-1210, June 2002.

[159] K. Pruessmann, M. Weiger, M. Scheidegger and P. Boesiger, "SENSE: sensitivity encoding for fast MRI.," *Magn Reson Med,* vol. 42(5), pp. 952-962, November 1999.

[160] J. Ma, J. Bankson and R. Stafford, "Multipoint Dixon Imaging using Sensitivity Encoding.," in *ISMRM: Proc Intl Soc Mag Reson Med 11 (2003)*, Toronto, 2003.

[161] C. McKenzie, S. Reeder, A. Shimakawa, N. Pelc and J. Brittain, "Abdominal Three Point Dixon Imaging with Self Calibrating Parallel MRI.," in *ISMRM: Proc Intl Soc Mag Reson Med (2004)*, Kyoto, 2004.

[162] J. Ma, J. Son, J. Bankson, R. Stafford, H. Choi and D. Ragan, "A fast spin echo two-point Dixon technique and its combination with sensitivity encoding for efficient T2-weighted imaging.," *Magn Reson Imaging,* vol. 23(10), pp. 977-982, December 2005.

[163] J. Ma, A. Vu, J. Son, H. Choi and J. Hazle, "Fat-suppressed three-dimensional dual echo Dixon technique for contrast agent enhanced MRI.," *J Magn Reson Imaging,* vol. 23(1), pp. 36-41, January 2006.

[164] H. Eggers, B. Brendel, A. Duijndam and G. Herigault, "Dual-echo Dixon imaging with flexible choice of echo times.," *Magn Reson Med,* vol. 65(1), pp. 96-107, January 2011.

[165] M. Bashir, B. Dale, E. Merkle and D. Boll, "Automated liver sampling using a gradient dual-echo Dixon-based technique.," *Magn Reson Med,* vol. 67(5), pp. 1469-1477, May 2012.

[166] S. Reeder, A. Vu, B. Hargreaves, A. Shimakawa, O. Wieben, C. McKenzie, J. Polzin and J. Brittain, "Rapid 3D-SPGR Imaging of the Liver with Multi-Echo IDEAL.," in *ISMRM: Proc Intl Soc Mag Reson Med 14*, Seattle, Washington, 2006.

[167] D. Weng, Y. Pan, X. Zhong and Y. Zhuo, "Water-fat separation with parallel imaging

based on BLADE.," *Magn Reson Imaging,* vol. 31(5), pp. 656-663, June 2013.

[168] F. Rybicki, T. Chung, J. Reid, D. Jaramillo, R. Mulkern and J. Ma, "Fast three-point dixon MR imaging using low-resolution images for phase correction: a comparison with chemical shift selective fat suppression for pediatric musculoskeletal imaging.," *AJR Am J Roentgenol,* vol. 177(5), pp. 1019-1023, November 2001.

[169] J. Hennig, A. Nauerth and H. Friedburg, "RARE imaging: a fast imaging method for clinical MR.," *Magn Reson Med,* vol. 3(6), pp. 823-833, December 1986.

[170] R. Buxton, G. Wismer, T. Brady and B. Rosen, "Quantitative proton chemical-shift imaging.," *Magn Reson Med,* vol. 3(6), pp. 881-900, December 1986.

[171] G. Brix, S. Heiland, M. Bellemann, T. Koch a W. Lorenz, „MR imaging of fat-containing tissues: valuation of two quantitative imaging techniques in comparison with localized proton spectroscopy.," *Magn Reson Imaging,* sv. 11(7), pp. 977-991, 1993.

[172] D. Detweiler and H. Erickson, Dukes' Physiology of Domestic Animals, 12th Edition, 2004.

[173] J. Pipe, "Motion correction with PROPELLER MRI: application to head motion and free-breathing cardiac imaging.," *Magn Reson Med,* vol. 42(5), pp. 963-969, November 1999.

[174] J. Pipe, V. Farthing and K. Forbes, "Multishot diffusion-weighted FSE using PROPELLER MRI.," *Magn Reson Med,* vol. 47(1), pp. 42-52, January 2002.